Molecular dynamics of metal oxides with induced electrostatic dipole moments

Molekulardynamik von Metalloxiden mit induzierten elektrostatischen Dipolmomenten

Von der Fakultät für Mathematik und Physik der Universität Stuttgart zur Erlangung der Würde eines Doktors der Naturwissenschaften (Dr. rer. nat.) genehmigte Abhandlung

Vorgelegt von

Philipp Beck

aus Bad Friedrichshall

Hauptberichter:	Prof. Dr. H.-R. Trebin
Mitberichter:	Prof. Dr. C. Holm
Tag der mündlichen Prüfung:	17.12.2012

Institut für Theoretische und Angewandte Physik
der Universität Stuttgart

2012

Meinen Eltern

... und meiner Schwester

Inhaltsverzeichnis

List of symbols

$\{x_i\}$	ensemble of i variables x_i
$\mathbf{v}$	vector
v	$:= \lvert\mathbf{v}\rvert$ for a vector $\mathbf{v}$
$\hat{O}$	operator
$\underline{\underline{\mathrm{M}}}$	matrix
$\sum_n$	$:= \sum_{n=1}^{N}$, in which N is given by the context
$\sum_{n,m}$	$:= \sum_n \sum_m$
$\mathbf{v}_1\mathbf{v}_2$	$:= \mathbf{v}_1 \cdot \mathbf{v}_2$, inner product of two vectors
$\mathbf{v}_1 \otimes \mathbf{v}_2$	dyadic product of two vectors
$D_1 \otimes D_2$	representation product of two representations

List of Figures

List of Tables

Abstract

Metal oxides belong to the most important material classes in industrial technology. These high-tech ceramics are irreplacable in lots of modern microelectronic devices due to their excellent insulating properties, high melting points and high degrees of hardness. In the theoretical study of these systems, the atomistic modelling with molecular dynamics simulations and classical effective interaction force fields is a very powerful tool. There, fundamental properties can be uncovered and understood due to the atomic resolution. Both force field generation and simulation of oxide systems are computationally much more demanding than those of metals or covalent materials due to long-range electrostatic interactions. Furthermore, it is often not sufficient to only take Coulomb interactions into account, but to include electrostatic dipole moments. The latter can be integrated with the Tangney-Scandolo polarizable force field model, where dipole moments are determined by a self-consistent iterative solution during each simulation time step. Applying the direct, pairwise Wolf summation to interactions between charges and its extension to dipole moments avoids high computational effort due to its linear scaling properties in the number of particles. Three relevant metal oxides have been selected to apply the new high-performance force field generation model. Therewith, a detailed investigation of crack propagation was possible. Both crack propagation insights and the influence of cracks on the dipole field are shown. Finally, the coupling of strain and – even more meaningful – strain gradient with the dipole moments is presented, which gives rise to flexoelectric effects in non-piezoeletric materials.

Zusammenfassung in deutscher Sprache

Dass der unheimlich komplex gereifte Methodenapparat der Computerphysik, der sich in aufwändigen Gleichungssystemen und verpackt in tausende von Code-Zeilen präsentiert, die Fähigkeit besitzt, hochpräzise Aussagen über moderne Materialien sowohl des Alltags als auch der Hightech-Mikroindustrie zu treffen, ohne mit dem betreffenden Stoff jemals in realen Kontakt gekommen zu sein, ist nachvollziehbar und damit einhergehend logisch, aber dennoch bewundernswert und faszinierend zugleich.

Einleitung

Ein tiefroter Rubin auf einem goldenen Ring, eine Saphir-bestückte Kette um den Hals einer Dame – schöne Erscheinungsformen von Metalloxiden begegnen uns fern der Wissenschaft. Ein Blick auf industrielle Anwendungen verrät darüberhinaus, dass Metalloxide unerlässlich sind in Jedermanns Computer (in Transistoren eines gängigen Mikrochips wird ein dünner Siliziumdioxid-Film zur elektrischen Isolierung verwendet), in jedem Handy (oft wird hier Aluminiumoxid als Schutzschicht und Hitzeschild um Metallkomponenten eingesetzt) und als Alltags-Glas (sowohl Fenster- als auch Trinkgläser bestehen aus amorphem Siliziumdioxid). Nicht ganz so offensichtlich – aber genau so wertvoll – sind kleine Mengen an Metalloxiden in Alltagsprodukten verborgen: In der Lebensmittelindustrie versteckt sich hinter dem Emulgator-Zusatzstoff E 530 Magnesiumoxid; Siliziumdioxid wird aufgrund seiner Ungiftigkeit häufig in der Kosmetik eingesetzt; und Lacke sowie Farben besitzen ebenfalls kleine Beimengungen von Siliziumdioxid (hier oftmals als amorphe Nanopartikel) zur Erhöhung der Kratzfestigkeit. Schlussendlich ist jede Wüste gefüllt mit Quarz-Sand (kristallines Siliziumdioxid), und die Erdkruste besteht zu sehr großen Teilen aus Metalloxiden, hier stellt ebenfalls Quarz eines der wichtigsten Minerale dar. Zusammenfassend lässt sich aussagen, dass wir täglich derart von Me-

talloxiden und Metalloxid-Produkten umgeben sind, dass deren eingehende Analyse durch Simulationen von größtem Interesse ist.

Die vorliegende Arbeit wird nicht mit einem neuen Metalloxid-haltigen Hightech-Produkt enden; vielmehr ist sie grundlagenorientiert und erweitert den Horizont der atomistischen Simulationen von Metalloxiden. Da eine technische Anwendung basierend auf Ergebnissen der Grundlagentheorie jedoch nie auszuschließen ist, gibt ein Ausblick auf mögliche industrielle Anwendungsgebiete der Simulation von Metalloxiden einen anschaulichen Rahmen.

Computersimulationen

Zu Beginn jeder computergestützten Material-Analyse muss die am besten geeignete Simulationsmethode evaluiert werden. Das Vorgehen, welches die Phänomene der Natur am präzisesten abzubilden vermag, stellt die quantenmechanische Betrachtung eines Vielteilchensystems dar, was dazu führt, die Vielteilchen-Dirac-Gleichung numerisch lösen zu müssen. Selbst mit der Fülle an Näherungen, die zur ab initio Dichtefunktionaltheorie führen, sind quantenmechanische Methoden immer auf sehr kleine Systemgrößen und kurze Zeitskalen beschränkt. Modernste Realisierungen kombiniert mit schnellsten Rechnerarchitekturen stoßen bereits bei der Betrachtung weniger tausend Teilchen an ihre Grenzen – Systemabmessungen, die reale technologische Anwendungen um viele Größenordnungen unterschreiten. Demgegenüber stehen kontinuierliche Methoden mit einer vergröberten Sicht auf kondensierte Materie, die faszinieren, weil sie in der Lage sind, ganze makroskopische Objekte in Alltagsgröße und über Alltagszeitabstände hin zu modellieren. Jedoch muss diese Fähigkeit erkauft werden durch den Verzicht auf eine atomare Auflösung der zugrunde liegenden physikalischen Phänomene – per Definitionem.

Die vorliegende Arbeit basiert zu großen Teilen auf Molekulardynamik-Simulationen, wo eine zufriedenstellende Berücksichtigung der quantenmechanischen Natur von Materie über klassische effektive Kraftfelder eingebracht wird. Diese Kraftfelder werden einzig und allein mit ab initio Referenzdaten erzeugt. Da die Quantenmechanik nur noch in diesen steckt und die eigentliche Simulation mit klassischen Bewegungsgleichungen beschrieben wird, können viele Millionen Atome über viele Nanosekunden hinweg modelliert werden. In diesem Sinne stellt die Wahl von Molekulardynamik-

Simulationen einen Kompromiss dar zwischen der Auflösung physikalischer Phänomene und dem Erlangen von Zeit- und Längen-Skalen, die notwendig sind, um die gewünschten Materialeigenschaften simulieren zu können.

In der klassischen Molekulardynamik werden Newton's Bewegungsgleichungen für ein Ensemble von Atomen numerisch gelöst, wobei die Integration durch Diskretisierung der Zeit angenähert wird, weil es nicht möglich ist, dieses gekoppelte System von Differenzialgleichungen exakt zu lösen. Mit dem Simulations-Code IMD (ITAP Molecular Dynamics, [84]) können verschiedene thermodynamische Ensembles ebenso realisiert werden wie nahezu beliebige Randbedingungen. Die Wechselwirkungen zwischen den Atomen gehen ein durch Kraftfelder, die mit dem Programm potfit [9] erzeugt werden. Dieses generiert effektive atomare Kraftfelder, indem es deren Parameter derart justiert, dass ab initio vorgegebene Kenndaten (Kräfte, Energien und Spannungen aus Referenz-Konfigurationen) ideal reproduziert werden.

Elektrostatik

Die Bindungs-Situation in Metalloxiden kann mit dem Konzept ionischer Festkörper beschrieben werden, in welchen die Ladungsdichte jedes Ions hauptsächlich nahe des Kerns und näherungsweise isotrop lokalisiert ist. Wechselwirkungen zwischen Ionen können dann mit elementaren Coulomb-Kräften beschrieben werden. Diese elektrostatischen Wechselwirkungen sind weitreichend und müssen in der Simulation geeignet behandelt werden. Kurzreichende Wechselwirkungen werden gängigerweise mit Abschneideradien belegt, wodurch eine akkurate Näherung erzielt werden kann. Würde man dieses Vorgehen auf elektrostatische Kräfte übertragen, wären solch große Abschneideradien nötig, dass die Rechenzeiten explodieren würden. Diese Problematik wurde in den vergangenen dreißig Jahren auf viele verschiedene Arten gelöst. Für die vorgestellten Simulationen erwies sich die direkte Wolfsummation [97] als am besten geeignet. Sie passt hervorragend zur Struktur von IMD und skaliert linear mit der Teilchenzahl. Außerdem erlaubt sie nahezu beliebige Randbedingungen. In vielen Tests übertrifft sie – speziell für die Anwendung auf kondensierte ionische Materie – viele andere Coulomb-Löser.

Weiterhin zeigt sich, dass es oftmals nicht ausreicht, lediglich Coulomb-Kräfte zwischen den Ionen zu berücksichtigen. Die elektrostatischen Wechselwirkungen wurden daher um Dipol-Kräfte ergänzt. Die Dipolmomente hängen nach der verwendeten Methode von Tangney und Scandolo (TS) [88] vom lokalen elektrischen Feld umliegender Ladungen und Dipolmomente ab. Somit muss eine selbst-konsistente iterative Lösung gefunden werden, was aber in allen vorliegenden Fällen sehr schnell und damit wenig Rechenzeit-intensiv gelingt. Das TS Modell liefert trotz seiner Einfachheit schnelle und präzise Simulations-Ergebnisse.

Die Verknüpfung des Dipol-Modells mit der Wolfsumme stellt eine Neuerung dar, welche die Präzision von Oxidmodellierungen erhöht und dabei gleichzeitig die Rechenzeit möglichst gering hält. Die detailreichen Konzepte, die bei dieser Verknüpfung von Nöten waren, erweisen sich als lohnenswert.

Visualisierung

Moderne Techniken der Visualisierung leisten weit mehr als die Produktion schöner Bilder aus Simulations-Datensätzen. Sie sind in der Lage, mit cleveren und speziell an die jeweilige Problemstellung angepassten Darstellungsmethoden Phänomene sichtbar zu machen, die sonst unentdeckt blieben. Auch bei der vorliegenden Metalloxid-Studie wurde die Visualisierung von Datensätzen eingesetzt, ebenfalls mit dem Erfolg, neue Entdeckungen zu enthüllen, die sonst vermutlich verborgen geblieben wären. Das Progamm MegaMol [29] wurde in den vergangenen zwei Jahren um ein Modul erweitert, welches speziell für die Darstellung von elektrostatischen Dipolmomenten zuständig ist. Neben gängigen glyphen-basierten Darstellungen – wie ein Atom durch eine Kugel oder ein Moment durch einen Pfeil zu zeigen – wurde das Konzept der fraktionalen Anisotropie (FA) eingesetzt, um kollektives Dipol-Verhalten aufdecken zu können. Die FA wurde ursprünglich entwickelt, um effektive Diffusions-Tensoren z.B. in der Magnetresonanz-Bildgebung zu untersuchen. Durch die Übertragung der Methodik auf das Feld der elektrischen Dipole kann ein Skalar-Feld berechnet werden, welches angibt, wie stark Momente lokal korreliert sind. Im Gegensatz zu simpler Aufsummierung nahegelegener Momente erkennt die FA auch antiferroelektrische Ordnung und kann sie von isotropen Regionen abgrenzen. Um verschiedene Regionen auch visuell abzugrenzen, wurden

Isoflächen in MegaMol implementiert, die Regionen gleichartiger Dipol-Ausrichtung umhüllen. Zusätzliche Erweiterungen, wie eine Richtungskodierung in der Farbe der Pfeilglyphen und Schattierungsmechanismen für noch bessere optische Unterschiedung verschiedener Regionen komplettieren das Ensemble an Darstellungs-Mechanismen, die zu wesentlichen physikalischen Ergebnissen geführt haben.

Kraftfelder

Mithilfe des neuen Methoden-Apparates wurden Kraftfelder generiert für drei der wichtigsten Metalloxide. Begonnen wurde mit flüssigem Siliziumdioxid, weil auch Tangney und Scandolo dieses Oxid für erste Kraftfeld-Erstellungen verwendeten und sich damit perfekte Vergleichs-Möglichkeiten boten. Weiterhin wurde flüssiges Magnesiumoxid gewählt, weil es durch seine strukturelle Einfachheit bereits sehr häufig modelliert wurde und hier ebenfalls gute Validierungsmöglichkeiten bestehen. Schließlich wurde als erstes kristallines System Aluminiumoxid herangezogen, sodass auch stöchiometrisch möglichst verschiedenartige Kraftfelder entstehen konnten. Die Anwendung der Wolfsumme auf Kristalle stellt eine Erhöhung der Schwierigkeit dar, weil die Wolfsumme prinzipell präziser in Systemen arbeitet, in welchen ein isotroper Ladungshintergrund vorliegt. Letzterer ist in Schmelzen besser gegeben als in periodischen Strukturen. Dennoch gelang es, ein hoch-effizientes Kraftfeld zu erzeugen.

Alle drei Kraftfelder wurden intensiv validiert um sicherzustellen, dass sie schnelle, effiziente und präzise Modellierung erlauben. Zahlreiche Vergleichsrechnungen mit experimentellen und ab initio Ergebnissen wurden durchgeführt. Die Schmelzen-Kraftfelder können sowohl mikroskopische Radial- und Winkel-Verteilungen als auch makroskopische Eigenschaften wie thermodynamisch korrekte Druck-Volumen-Beziehungen oder phononische Zustandsdichten reproduzieren. Das Aluminiumoxid-Kraftfeld modelliert die kristalline Struktur mit hoher Genauigkeit. Kohäsions- und Oberflächenenergien sind ebenso präzise reproduzierbar wie die phononische Zustandsdichte. Zusammenfassend sind hier drei sehr potente Kraftfelder gegeben, die online [70] zur Verfügung stehen und bereits mehrfach heruntergeladen wurden.

Stellenwert der Dipole

Der zusätzliche Rechenaufwand bei der Berücksichtigung von Dipolmomenten beträgt etwa einen Faktor 3 in der Simulations-Dauer. Auch wenn sich die erstellten Kraftfelder als sehr fähig erwiesen haben, musste zusätzlich geklärt werden, wieviel besser diese arbeiten im direkten Vergleich mit dipolfreien Kraftfeldern. Es zeigt sich dabei, dass die Berücksichtigung der Dipole bei mikroskopischen Radialverteilungen kaum Relevanz zeigt. Dagegen sind Dipole deutlich wichtiger bei Winkelverteilungen. Unterschiede bei mikroskopischen Phänomenen verringerten sich dabei mit steigender Temperatur. Auch Kristall-Parameter konnten mit der Hinzunahme von Dipolen besser modelliert werden. Bei kollektiven makroskopischen Eigenschaften zeigten sich die Dipole als unverzichtbar. Energieberechnungen liefern deutliche Abweichungen und thermodynamische Zustandsgleichungen können ohne Dipole überhaupt nicht mehr reproduziert werden. Eine detaillierte Analyse der einzelnen Kenndaten und ihr Vergleich mit den zugehörigen ab initio Werten zeigt, dass es weniger die Kräfte zwischen Atomen sind, die bei Hinzunahme von Dipolmomenten akkurater modelliert werden können, sondern vielmehr die Spannungen im System ohne Dipole nicht korrekt abgestimmt werden können. Insgesamt ist die Erhöhung der Rechendauer durch die Berücksichtigung von elektrostatischen Dipolmomenten in den meisten der Fällen nicht nur gerechtfertigt, sondern unerlässlich.

Risse in α-Aluminiumoxid

Eine vielversprechende Anwendung des Kraftfeldes für α-Aluminiumoxid versprach die Modellierung von sich ausbreitenden Rissen. Detailliertes Wissen über das Rissverhalten auf atomarer Ebene erbringt nicht nur neue Einsichten in die Natur von Rissen, sondern kann auch Informationen beisteuern zur vergröberten Rissanalyse, beispielsweise mit finiten Elementen. Nach jetzigem Wissensstand stellen die vorliegenden Ergebnisse die bisher erste dynamische Untersuchung von Rissen in einem Metalloxid mithilfe von MD Simulationen und unter Berücksichtigung elektrischer Dipole dar. Bedindung hierfür war die positive Validierung des Kraftfeldes für freie Grenzflächen und für Systeme unter Spannung.

Im ersten Schritt wurde untersucht, in welchen kristallographischen Ebenen und in welche Richtungen eingebaute Risskeime verlaufen können. Die Ergebnisse stimmen exakt mit jüngsten elektronenmikroskopisch erfassten experimentellen Studien [59] überein. Im zweiten Schritt wurde – ebenfalls erstmalig – der Einfluss eines laufenden Risses auf das elektrische Feld der Dipolmomente untersucht. Es zeigt sich, dass die Dipole empfindlich auf das vom Riss erzeugte Spannungsfeld reagieren. Im Bereich der Probe, die der Riss noch nicht erreicht hat und die folglich unter Spannung steht, existieren antiferroelektrisch geordnete Gebiete, wohingegen in Bereichen ober- und unterhalb des Risses, in denen die Spannung durch den Riss bereits abgebaut ist, isotrope Dipol-Regionen vorliegen. Hinzu kommen Oberflächen-Phänomene, die ebenfalls mit der Erwartung übereinstimmen: Momente an Sauerstoff-terminierten Riss-Grenzflächen hin zum Vakuum richten sich parallel aus. Ebenfalls klären konnte die Simulation den Sachverhalt, dass die Oberflächen-Effekte stärker sind als kollektive Phänomene im Inneren der untersuchten Probe. Insgesamt erbringt die Riss-Studie – auch durch die Sichtbarmachung dynamischer Phänomene mithilfe der eingesetzten Visualisierung – eine Fülle an neuen Erkenntnissen bei der Untersuchung des Wechselspiels zwischen heterogener Spannung und dem Feld der Dipole: Die Dipol-Ordnung wird im Wesentlichen durch zwei Effekte des Risses gestört. Einerseits bewegen sich nahezu senkrecht vom Riss in das Dipolfeld hinein blasenförmige Gebiete der Unordnung, andererseits sendet die Riss-Spitze eine wellenförmige Störung im Feld der Dipole aus. Letzteres Verhalten erinnert an Riss-Einfluss-Studien auf die Gitterdynamik, aus denen bereits bekannt ist, dass phononische Störungen von Riss-Spitzen emittiert werden.

Flexoelektrizität

Auf der Suche nach der Ursache die für kollektive Ausrichtung von Dipolmomenten in Riss-Simulationen von α-Aluminiumoxid können piezoelektrische Effekte (Ausrichtung von Dipolen aufgrund von Spannung) ausgeschlossen werden, weil diese nur in nicht-inversionssymmetrischen Kristallstrukturen auftreten. Im letzten Kapitel wird daher die Kopplung zwischen Spannungsgradient und elektrostatischen Dipolmomenten, die sogenannte Flexoelektrizität, vorgestellt. Eine darstellungstheoretische Analyse zeigt, dass flexoelektrische Phänomene sowohl in α-Aluminiumoxid als

auch in Periklas (kristallines Magnesiumoxid in kubischer Natriumchlorid-Struktur) auftreten können, wohingegen piezoelektrische Effekte aus Symmetrie-Gründen untersagt sind. Durch die Flexoelektrizität wird eine neue Materialklasse für die technologischen Anwendungen zugänglich, in welchen durch Materialverformung elektrische Spannung abgegriffen werden kann oder – noch wesentlicher in umgekehrter Form – in welchen Materialverformung durch Stromfluss kontrolliert wird.

Das gruppentheoretisch vorhergesagte Auftreten der Flexoelektrizität in α-Aluminiumoxid und Periklas konnte in MD Simulationen mit den in dieser Arbeit vorgestellten Kraftfeldern bestätigt und genauer untersucht werden. Ein Nichtvorhandensein piezoelektrischer Kopplung konnte ebenfalls bestätigt werden. Nach jetzigem Wissensstand existierten vor dieser Arbeit keine atomistischen Simulationsergebnisse zu flexoelektrischen Phänomenen. Durch heterogene Verzerrung ließen sich Dipolmomente in Periklas einheitlich ausrichten. Der analytisch angenommene und experimentell vorausgesagte [3] lineare Zusammenhang zwischen Spannungsgradient und flexoelektrischer Polarisation konnte numerisch bestätigt werden. Mittels geschickter Implementierung mehrerer Verzerrungsgradienten in die Probe konnten Domänen unterschiedlicher Dipol-Ausrichtung erzeugt werden, die durch Néel-Wände sauber voneinander separiert werden. Aufgrund der komplexeren Kristallstruktur von α-Aluminiumoxid wurden hier komplexere Domänen-Anordnungen beobachtet, die nicht nur fließend ineinander übergehen können, sondern die von antiferroelektrischer Anordnung geprägt sind.

Zusammenfassung

Die vorliegende Arbeit vertieft die breit angelegte Modellierungs-Studie dreier wichtiger Metalloxide. Detaillierte Untersuchungen durch Molekulardynamik-Simulationen mit Kraftfeldern für Siliziumdioxid, Magnesiumoxid und α-Aluminiumoxid werden dargestellt. Speziell angepasste Visualisierungs-Techniken erweitern die numerischen Einblicke und verhelfen zu neuen Erkenntnissen in den untersuchten ionischen Systemen. Im Wesentlichen leistet die Arbeit einen dreistufigen Beitrag zur numerischen Erforschung ionischer kondensierter Materie:

1. Zunächst wird die neue Art der Kraftfelderstellung dargestellt, welche das Potenzial-Modell von Tangney und Scandolo mit der direkten

Wolfsummation verknüpft. Gezeigt wird die gewissenhafte Prüfung, dass die Vereinigung der Vorteile des TS Modells, welches elektrostatische Dipolmomente mit einbezieht, mit den linearen Skalierungs-Eigenschaften der Wolfsumme gelungen ist. Die Implementierung der Kraftfelderstellung in potfit durch den Autor gibt anderen Simulations-Gruppen die Möglichkeit, diese präzise, effiziente und flexible Methode für ihre individuellen Studien ionischer Materie einzusetzen.

2. Weiterhin werden die mithilfe der neuen Methodik generierten Kraftfelder für Siliziumdioxid, Magnesiumoxid und α-Aluminiumoxid vorgestellt. Neben ihrer Erstellung wird in jedem Einzelfall die sorgfältige Validierung gezeigt. Die neuen Kraftfelder werden nicht nur für eigene Simulationen eingesetzt, sondern anderen Gruppen öffentlich zugänglich gemacht. Dadurch können nun vielerorts Simulationen durchgeführt werden, die bisher aufgrund von Beschränkungen bezüglich Zeit-, Längenskalen oder Randbedingungen nicht annehmbar realisierbar waren.

3. Unter Einsatz der neuen Kraftfelder wurden verschiedene Simulationen durchgeführt, die – auch mithilfe der speziell angepassten Visualisierung der fraktionalen Anisotropie – zu neuen Entdeckungen und grundlegenden Erkenntnissen geführt haben:

   - Das für α-Aluminiumoxid erstellte Kraftfeld wurde zur MD Simulation von sich ausbreitenden Rissen verwendet, welche die vor zwei Jahren elektronenmikroskopisch untersuchten Verlaufs-Richtungen von in verschiedenen kristallinen Ebenen existierenden Rissen vollständig reproduzieren konnte. Darüberhinaus konnte – erstmalig in atomistischen Simulationen von Metalloxiden – der Einfluss von sich ausbreitenden Rissen auf die Orientierung der elektrostatischen Dipolmomente beobachtet und analysiert werden.
   - Derartige flexoelektrische Phänomene wurden schließlich sowohl in MD Simulationen als auch mithilfe der Darstellungstheorie untersucht. Die Kombination liefert eine konsistente Vorhersage flexoelektrischen Verhaltens in α-Aluminiumoxid und auch in Periklas, obwohl beide Materialien aufgrund ihrer inversionssymmetrischen Kristallstruktur keine Piezoelektrizität aufwei-

sen. Die analytisch angenommene und experimentell vorhergesagte lineare Kopplung zwischen Spannungsgradient und flexoelektrischer Polarisation wurde von MD Simulationen bestätigt. Erstmalig wurde flexoelektrische Domänenausbildung modelliert. In Periklas zeigt sich, dass flexoelektrische Domänen exakt von Néel-Wänden abgetrennt werden.

Zusammenfassend bieten die vorliegenden Ergebnisse an mehreren Stellen Raum zur weiteren Anwendung. Bereits jetzt werden sowohl die Kraftfeld-Erstellung in potfit als auch die präsentierten Kraftfelder andererorts genutzt. Insbesondere aber kann die Erwartung geäußert werden, dass die erstmalige Beobachtung flexoelektrischer Phänomene in atomistischen Simulationen weitere Studien auf diesem noch relativ neuen Forschungsgebiet initiieren wird.

Chapter 1.

Introduction

A ruby gemstone on a golden ring, a saphire jewelry around a lady's neck – there is pretty appearance of metal oxides in everyday life. In terms of industrial applications, metal oxides are ubiquitous in everyone's computer (insulating silica film in microchip transistors), mobile phone (alumina covering metallic components to prevent further oxidation and to act as heat shield) or ordinary glass (window or drinking glass is amorphous silica). More hidden, but just as helpful: magnesia encoded as emulsifier E 530 in food industry or silica as nontoxic additive in everyday cosmetics products or admixture in paint for increasing the scratch resistance. Further, a huge amount of quartz (crystalline silica) fills up every sand desert in the world and is the most abundant mineral in the earth's crust. To summarize, we are surrounded by metal oxides and metal oxide products daily. Hence, simulation studies of this material class are of great interest.

The present thesis details theoretical basic research and, hence, does not result in showing a new metal oxide microelectronics product. In fact, new fundamental research findings are presented which may in principle lead to future industrial applications. Thus, the merit of the results is pointed up by showing possible application scenarios of nowadays technology.

Atomistic simulation is a very powerful tool to investigate metal oxides. Nowadays, millions of atoms can be treated and fundamental properties can be uncovered and understood. Beside validating experimental results, theoretical simulations are always able to investigate regions, which are inaccessible to experiments. Molecular dynamics (MD) simulations allow a preferably accurate consideration of the quantum nature of matter by use of classical effective force fields, but without such strong length- and timescale restrictions ab initio calculations have to deal with.

Both force field generation and simulation of oxide systems are computationally much more demanding than those of metals or covalent materials due to long-range electrostatic interactions. Furthermore, it is often

not sufficient to only take Coulomb interactions into account, but to include electrostatic dipole moments. The latter can be integrated in simulations with the Tangney-Scandolo (TS) polarizable force field model [88], where dipole moments are determined by a selfconsistent iterative solution method during each simulation time step. Applying the direct, pairwise Wolf summation [97] to interactions between charges and its extension to dipole moments avoids too high computational effort due to its linear scaling properties in the number of particles.

The present thesis enlarges the collection of available force fields by presenting new faster and more efficiently working force fields for three relevant metal oxides (silica, magnesia and alumina). It shows MD simulations of metal oxide systems with the use of the new force fields and presents new findings such as crack propagation investigations, the influence of cracks on the dipole field and the coupling of strain gradient with dipole moments, which gives rise to flexoelectric effects in non-piezoelectric materials. Some findings have been uncovered by the visualization technique of fractional anisotropy which is novel applied to visualize MD trajectories.

The structure of the thesis is as follows: Chapter 2 shows basics of the computer simulation techniques that have been used for the present research. Beside the essential numeric approch of MD simulations, also ab initio calculations are introduced. In chapter 3, the whole approach of including electrostatics in MD simulations is discussed in detail. Mainly, the combination of TS model and Wolf summation is depicted. Chapter 4 details the applied visualization techniques. In addition to simple glyph representations as spheres for atoms and arrows for dipole moments, the method of fractional anisotropy is used to uncover regions of correlated dipole behavior. In chapter 5, the new force fields for silica, magnesia and alumina are presented as well as their careful validation to assure its high accuracy. Chapter 6 depicts a verification study to assure that – and for which applications more notably – the extra simulation effort caused by the new polarizable terms is justified. Chapter 7 presents the investigation of cracks in α-alumina. After an analysis of the propagation directions, a detailed investigation of the influence of cracks on the dipole field is given. Finally, chapter 8 shows a detailed analysis of the coupling of a strain gradient with the electrostatic dipole moments. Chapter 9 gives a conclusion and shows an outlook.

Parts of this work have been previously published in other publications of the author, cf. List of Publications on page 161.

Chapter 2.

Computer simulations

In the beginning of each material analysis by use of computational methods, the choice of the most suitable simulation type has to be made. The most accurate method is to consider the quantum nature of matter and solve the many-particle Dirac equation numerically. Even with the aid of many approximations - which are discussed in section 2.1 and which yield the ab initio formalism - this method cannot yet tackle the study of various material properties due to length and time scale restrictions. Although there have been enormous advances in first-principles methods, they are typically limited to systems containing at most few thousands atoms and to simulation times of few picoseconds. On the other hand, continuous approaches with a coarsened view on matter - which have the ability to simulate whole macroscopic objects in the region of meters and seconds - are not able to resolve underlying atomistic phenomena by definition.

The present work is mainly based on atomistic molecular dynamics (MD) simulations (section 2.2) where a preferably accurate consideration of the quantum nature of matter is included by use of classical effective force fields (section 2.3). The latter are generated by means of solely ab initio and not any empirical input data. Nevertheless, system sizes on micron length scales (which correspond to several million atoms) and timescales in the region of nanoseconds can be obtained. To this effect, selecting MD is striking a balance between resolution of physical phenomena and achievement of length and time scales required for the investigation of material properties the present thesis deals with.

2.1. Ab initio calculations

The force fields, which were used in MD simulations and are presented in chapter 5, were generated by adjusting the potential's parameters to opti-

mally reproduce a set of reference data computed in ab initio calculations (see section 2.3). This reference data base had to be created at the beginning of each force field generation. On the other hand, each finalized force field is validated in materials properties studies also by comparing its accuracy to own or externally calculated ab initio reference results. Hence, the ab initio formalism is present at different stages of force field development and from there is introduced briefly in the following.

2.1.1. Density functional theory

The need for density functional theory has its seeds in the problem of finding a many-particle wave function Ψ for N_{tot} particles in a condensed matter system. The consideration of a particle density $\rho(\mathbf{r})$ instead of Ψ does not make this intention possible either. Therefore, the following two basic approximations are introduced:

- The Born-Oppenheimer approximation: The electron mass is three orders of magnitude smaller than the nuclear mass. On the timescale of the nuclear motion, the electrons follow instantaneously. Hence, the equation of motion for the total system can be separated into a nuclear and an electronic part. The formalism below treats the pure electronic system where the core potential merely enters as a constant term in the total potential energy.

- Let a system of N interacting electrons be given. The basic accomplishment of W. Kohn's and L. J. Sham's density functional theory [41] is changing over to a virtual system of N non-interacting electrons in a modified effective potential. Hence, it is possible to describe each electron i by its effective single-particle wave function Ψ_i. The whole changeover takes place in such a manner that both original and virtual system have the same ground state energy.

2.1.2. The Hohenberg-Kohn theorems

The Hamilton operator $\hat{H}$ of a non-relativistic system of N electrons is composed of the kinetic energy operators $\hat{T}_i$ for each electron i, the interaction parts between each pair of electrons i and j, $\hat{U}_{ij}(\mathbf{r}_i, \mathbf{r}_j)$, and a potential function $W(\mathbf{r})$, which acts on each electron i and contains an

optionally external potential $W_{\mathrm{ext}}(\mathbf{r})$ and the core potential $W_{\mathrm{K}}(\mathbf{r})$. $\hat{H}$ is then given by

$$\hat{H} = \hat{T} + \hat{U}(\{\mathbf{r}_i\}) + W(\mathbf{r}), \tag{2.1}$$

where the individual parts can be written as

$$\hat{T} = \sum_i \hat{T}_i = -\frac{\hbar^2}{2m} \sum_i \triangle_i, \tag{2.2}$$

$$\hat{U}(\{\mathbf{r}_i\}) = \sum_{\substack{i,j \\ j \neq i}} \hat{U}_{ij}(\mathbf{r}_i, \mathbf{r}_j) = \sum_{\substack{i,j \\ j \neq i}} \frac{e^2}{|\mathbf{r}_i - \mathbf{r}_j|} \tag{2.3}$$

and

$$W(\mathbf{r}) = \sum_i W(\mathbf{r}_i) = \sum_i [W_{\mathrm{ext}}(\mathbf{r}_i) + W_{\mathrm{K}}(\mathbf{r}_i)] \tag{2.4}$$

with

$$W_{\mathrm{K}}(\mathbf{r}) = \sum_{\mathrm{I}} \frac{Z_{\mathrm{I}} e^2}{|\mathbf{r} - \mathbf{R}_{\mathrm{I}}|}. \tag{2.5}$$

$\mathbf{r}_i$ are the electron coordinates, e is the elementary charge, m the electron mass, $\mathbf{R}_{\mathrm{I}}$ are the nuclei coordinates and Z_{I} the nuclei charges. The total energy is then defined as the functional

$$\begin{aligned} \tilde{E}[\rho(\mathbf{r})] &:= E_1 + E_2 \\ &= < \Psi \mid \hat{T} + \hat{U} \mid \Psi > \; + \int \rho(\mathbf{r}) W(\mathbf{r}) \; \mathrm{d}^3\mathrm{r} \end{aligned} \tag{2.6}$$

The minimum in E_1 has to be found in a way, that only many-particle wave functions are taken into account, which correspond to the given electron density $\rho(\mathbf{r})$. As can be seen from equation (2.4), the potential function is uniquely determined by the external and the core potential.

With it, the theorems of Hohenberg and Kohn [33] can be written as:

1. Any ground state property can be expressed by a functional depending solely on the ground state electron density $\rho^0(\mathbf{r})$.

2. Both ground state electron density $\rho^0(\mathbf{r})$ and corresponding ground state energy $E^0[\rho^0(\mathbf{r})]$ are obtained by minimizing the energy functional.

2.1.3. Virtual system of non-interacting electrons

The first term E_1 of the energy functional in Eq. (2.6) contains the many-particle wave function Ψ and the interelectronic energy parts, which both have to be avoided due to its overly large computing time and memory requirement. Changing over to a virtual system of N non-interacting electrons in a modified effective potential eliminates these quantities. This changeover is realized by a substitution of

1. the energy term E_1,

$$E_1 \longrightarrow E_{\mathrm{H}}[\rho(\mathbf{r})] + E_{\mathrm{kin}}[\rho(\mathbf{r})] + E_{\mathrm{xc}}[\rho(\mathbf{r})], \tag{2.7}$$

2. and the potential function,

$$W(\mathbf{r}) \longrightarrow W_{\mathrm{eff}}(\mathbf{r}). \tag{2.8}$$

The Hartree energy,

$$E_{\mathrm{H}}[\rho(\mathbf{r})] := \frac{e^2}{2} \int\int \frac{\rho(\mathbf{r})\rho(\mathbf{r}')}{|\mathbf{r}-\mathbf{r}'|}\ \mathrm{d}^3\mathrm{r}\ \mathrm{d}^3\mathrm{r}', \tag{2.9}$$

is a functional of the electron density $\rho(\mathbf{r})$ and describes the interaction of $\rho(\mathbf{r})$ with itself without consideration of any electronic exchange and correlations. $E_{\mathrm{kin}}[\rho(\mathbf{r})]$ is defined as the total kinetic energy of the system of non-interacting electrons in an effective interaction potential $W_{\mathrm{eff}}(\mathbf{r})$. Note that $E_{\mathrm{kin}}[\rho(\mathbf{r})]$ takes another value compared to the kinetic energy of the original real system. The exchange-correlation functional $E_{\mathrm{xc}}[\rho(\mathbf{r})]$ is defined to compensate the two approximations (negligence of correlation and exchange effects and different kinetic energy). In a system of non-interacting electrons the energy functional in Eq. (2.6) by definition becomes

$$E[\rho(\mathbf{r})] := E_{\mathrm{kin}}[\rho(\mathbf{r})] \ + \ \int \rho(\mathbf{r}) W_{\mathrm{eff}}(\mathbf{r})\ \mathrm{d}^3\mathrm{r}. \tag{2.10}$$

Finally, the following condition determines $W_{\mathrm{eff}}(\mathbf{r})$: Minimizing the energy functional of both real and virtual system lead to the same ground state density. Hence, the variation of both $\tilde{E}[\rho(\mathbf{r})]$ and $E[\rho(\mathbf{r})]$ vanishes at this point.

2.1.4. The Kohn-Sham equations

Each non-interacting electron i with single-particle wave function Ψ_i and energy eigenvalue ϵ_i then fulfills the single-particle Schrödinger equation

$$[-\frac{\hbar^2}{2m} \triangle_i + W_{\text{eff}}(\mathbf{r})] \; \Psi_i(\mathbf{r}) = \epsilon_i \Psi_i(\mathbf{r}). \tag{2.11}$$

With the condition discussed at the end of section (2.1.3), the effective interaction potential can be written as

$$W_{\text{eff}}(\mathbf{r}) = W(\mathbf{r}) + e^2 \int \frac{\rho(\mathbf{r}')}{|\mathbf{r} - \mathbf{r}'|} \, \mathrm{d}^3\mathrm{r}' + \frac{\delta E_{\text{xc}}[\rho(\mathbf{r})]}{\delta \rho(\mathbf{r})}. \tag{2.12}$$

The ansatz for the density is

$$\rho(\mathbf{r}) = \sum_i f(\epsilon_i) \Psi_i^*(\mathbf{r}) \Psi_i(\mathbf{r}) \tag{2.13}$$

with

$$f(\epsilon_i) = \begin{cases} 1 & \text{if } \epsilon_i \leq \epsilon_{\text{F}} \\ 0 & \text{if } \epsilon_i > \epsilon_{\text{F}} \end{cases}$$

and the Fermi energy ϵ_{F}. The equations (2.11)-(2.13) are the Kohn-Sham equations [41], a system of $N + 2$ equations, which can be solved selfconsistently to determine the $N + 2$ quantities $\Psi_i(\mathbf{r})$, $W_{\text{eff}}(\mathbf{r})$ und $\rho(\mathbf{r})$ for a system of N electrons.

It is important to note that the electron density $\rho(\mathbf{r})$ uniquely determines the effective potential function $W_{\text{eff}}(\mathbf{r})$ as can be supposed from equation (2.12). An explicit proof can be found in [27] on page 39. Hence, the energy in Eq. (2.10) is solely a functional of the electron density $\rho(\mathbf{r})$ and the first theorem of Hohenberg and Kohn (p. 29) is still valid.

2.1.5. Exchange-correlation functional

In the end, the exchange-correlation functional $E_{\text{xc}}[\rho(\mathbf{r})]$, which is not known exactly, has to be determined. The most basic approach is the Local Density Approximation (LDA) by Kohn and Sham [41]. In the LDA, the exchange-correlation energy is assumed to be a local quantity and thus

can be expressed by an energy density $e_{\mathrm{xc}}[\rho(\mathbf{r})]$ (the latter is related to the local quantity of a homogeneous electron gas):

$$E_{\mathrm{xc}}^{\mathrm{LDA}}[\rho(\mathbf{r})] = \int \rho(\mathbf{r})\ e_{\mathrm{xc}}[\rho(\mathbf{r})]\ \mathrm{d}^3\mathrm{r}. \tag{2.14}$$

The LDA is known to sometimes underestimate the volume of a condensed matter system. Hence, further enhancements have been introduced: The Local Spin-Density Approximation (LSDA) introduces spin-densities $\rho_{\uparrow,\downarrow}(\mathbf{r})$ and is a generalization of the LDA. Based on electron spins as well, another approach is the Generalized Gradient Approximation where the exchange-correlation energy may also depend on the gradient of the spin components of the charge density:

$$E_{\mathrm{xc}}^{\mathrm{GGA}}[\rho_\uparrow(\mathbf{r}), \rho_\downarrow(\mathbf{r})] = \int g[\rho_\uparrow(\mathbf{r}), \rho_\downarrow(\mathbf{r}), \nabla\rho_\uparrow(\mathbf{r}), \nabla\rho_\downarrow(\mathbf{r})]\ \mathrm{d}^3\mathrm{r}. \tag{2.15}$$

g is a density function, which in each approach has to be further spezified.

2.1.6. Atomic forces

As mentioned at the beginning of this chapter, the force fields the present thesis deals with (see chapter 5) were generated by adjusting the potential's parameters to optimally reproduce a set of ab initio reference data (see section 2.3). This reference data consists of energies, forces and stresses. The ground state energy $E^0(\mathbf{r})$ was already given by the second theorem of Hohenberg and Kohn (p. 29). A force $\mathbf{F}_I$ which acts on an atom I at coordinate $\mathbf{R}_I$ can then be calculated as the derivative of $E^0(\mathbf{r})$ with respect to the atomic coordinates:

$$\begin{aligned} \mathbf{F}_I &= -\nabla_{R_I} E^0(\mathbf{r}) = -\nabla_{R_I} \int \Psi^{*0}(\mathbf{r})\hat{H}(\mathbf{r})\Psi^0(\mathbf{r})\ \mathrm{d}^3\mathrm{r} \\ &= -\int \Psi^{*0}(\mathbf{r})\ [\ \nabla_{R_I}\hat{H}(\mathbf{r})\ ]\ \Psi^0(\mathbf{r})\ \mathrm{d}^3\mathrm{r} \end{aligned} \tag{2.16}$$

with $\nabla_{R_I} f(\mathbf{r}) := \nabla_r f(\mathbf{r})|_{\mathbf{R}_I}$ (f any function as Ψ or $\hat{H}$). The last conversion of equation (2.16) is based on the Hellmann-Feynman theorem which proves the relation

$$\int [\ \nabla_{R_I}\Psi^{*,0}(\mathbf{r})\ ]\ \hat{H}(\mathbf{r})\Psi^0(\mathbf{r})\ \mathrm{d}^3\mathrm{r}\ +\ \int \Psi^{*,0}(\mathbf{r})\hat{H}(\mathbf{r})\ [\ \nabla_{R_I}\Psi^0(\mathbf{r})\ ]\ \mathrm{d}^3\mathrm{r} = 0. \tag{2.17}$$

The components of the stress tensor can be obtained similarly.

Note that in the ab initio molecular dynamics approach, which is described in section 2.2.2, also the atomic forces are required and, hence, are calculated with equation (2.16).

2.1.7. Vienna Ab Initio Simulation Package (VASP)

The density functional theory based calculations for this thesis were done with the Vienna Ab Initio Simulation Package (VASP) [43, 44], which can be executed in parallel to reduce computational time. It can deal with LDA exchange-correlation functionals, whereof a parametrization from Perdew and Zunger [67] is provided. Also the GGA version is supported, where an implementation for the function g (see section 2.1.5) is provided by Perdew [66]. In the following, further VASP specific implementations are briefly discussed.

Periodic boundary Conditions

So far, the density functional theory formalism is described for a system of N electrons in a finite space. To map a real crystalline system to a first-principles calculation, one switches over to an infinite and periodic system. According to Bloch's theorem, an electronic wave function in a periodic system can be written as a product of a plane wave and a function with the periodicity of the lattice. In VASP, the periodic function is then expanded in a plane wave basis set taking reciprocal lattice vectors as wave vectors. Basically, the plane wave basis set is infinite. To avoid infinite computational time, an energy cutoff E_{cut} is introduced. Solely plane waves with a wave vector corresponding to an energy below E_{cut} are taken into account. E_{cut} has to be determined to provide for all oscillations occuring in the wave functions.

Each wave function is characterized uniquely by a wave vektor $\mathbf{k}$ and a band index j. Due to periodicity, it is adequate to calculate only the electronic states in the first Brillouin zone (BZ, volume Ω). Instead of summing over all states and weighting with the fermi energy function $f(\epsilon_i)$ in Eq. (2.13), one only needs to integrate over the first BZ and sum over all bands:

$$\sum_i f(\epsilon_i) \ \ldots \ \longrightarrow \ \sum_j \frac{1}{\Omega} \int_{\mathrm{BZ}} \mathrm{d}^3\mathrm{k} \, f(\epsilon_{j\mathbf{k}}) \ \ldots \tag{2.18}$$

In an unlimited crystal lattice structure, the **k**-vectors are dense in the reciprocal space. Then, the integral in Eq. (2.18) is replaced by a sum over a discrete set $\{\mathbf{k}_\nu\}$ of $N_\mathbf{k}$ sampling points in the **k**-space:

$$\sum_j \frac{1}{\Omega} \int_{\mathrm{BZ}} \mathrm{d}^3\mathrm{k}\; f(\epsilon_{j\mathbf{k}}) \;\ldots\; \longrightarrow \;\sum_j \frac{1}{N_\mathbf{k}} \sum_\nu f(\epsilon_{j\mathbf{k}_\nu}) \;\ldots \tag{2.19}$$

If the considered unit cell shows point symmetries, it is even sufficient to treat only the irreducible Brillouin zone, which results in an additional speedup. In VASP, the discrete **k**-grid can be created with the algorithm by Monkhorst and Pack [61]. Both precision and computational time increase with a denser grid. For each application, a compromise has to be effected. During ab initio calculations for the present work, a **k**-grid with only 2×2×2 k-points was sufficient due to the relatively large sample sizes containing number of atoms in the range of 100. The energy deviation compared to testruns with $32 \times 32 \times 32$ k-points was smaller than 0.02%.

Pseudopotentials

The physical questions within this thesis basically depend on the valence electrons, whose wave functions feature strong oscillations. The more oscillations occur, the higher E_{cut} has to be chosen, which results in a higher computational time. Also taking into account the less interesting core electrons all along slows down the calculation extensively. First-principles calculations with typical unit cell sizes (containing few hundred atoms) are impossible without the pseudopotential formalism, that was first introduced by Philipps [68] and that eliminates both issues. In the pseudopotential formalism, the core electrons are pre-calculated and kept frozen during further calculations. The original core potential (Eq. (2.5)) is replaced by a pseudopotential, which comprehends the core electrons. Due to the reduced net charge (core charge minus core electron charges), the new pseudopotential is smoother, thus yielding less oscillations in the new pseudo wave functions and enabling a lower E_{cut}. The substitution of both potential and wave functions is illustrated in Fig. 2.1. Two conditions have to be fulfilled:

1. Outside a sphere with radius r_c, potential (wave function) and pseudopotential (pseudo wave function) have to be identical.

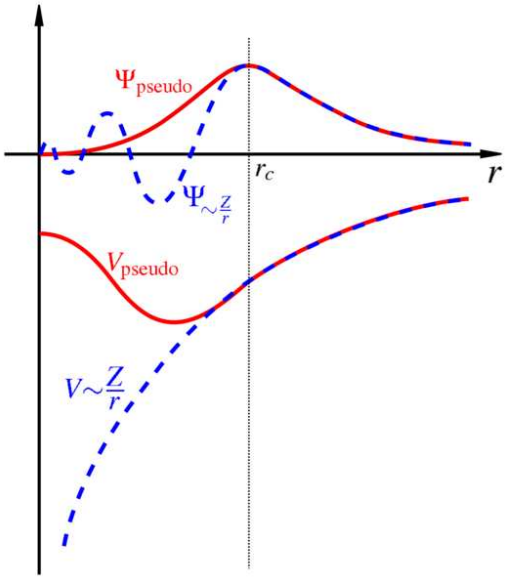

Figure 2.1.: Schematic picture of Coulomb potential V and a wave function $\Psi_{\sim\frac{Z}{r}}$ (dashed) and correspondent pseudopotential V_{pseudo} and pseudo wave function Ψ_{pseudo} (solid). Outside a sphere with radius r_c, potential (wave function) and pseudopotential (pseudo wave function) are identical. From [96].

2. Within the sphere, the effect of the pseudopotential on the pseudo wave functions has to yield the same results as the effect of the original potential on the original wave functions.

By now, there are various realizations of the pseudopotential formalism. Among others, VASP supports the Projector Augmented-Wave method (PAW), which is mostly applied for the calculations of the present thesis. Details of the PAW method can be found in [45]. The pseudopotentials provided by VASP already feature an optimized default E_{cut}. Usually, there is no need to change it.

Relativistic Density functional theory

In favor of clearness and convenience, the whole ab initio formalism was discussed in its non-relativistic form, although two relativistic options are implemented in VASP:

1. The core electrons are treated fully relativistic. Thereby, the Schrödinger equation - Eq. (2.11) - is replaced by the Dirac equation, which yields the Kohn-Sham-Dirac equations, that are solved selfconsistently as discussed in section 2.1.4.

2. The valence electrons are treated scalar-relativistic. Two terms accounting for relativistic effects are added ad hoc to the Hamilton operator in Eq. (2.1): The Darwin term provides for the electronic trembling motion, and a second term introduces the dependence of mass on velocity.

2.2. Molecular dynamics

Molecular dynamics (MD) is the essential numeric approach the present thesis deals with. The MD program package ITAP Molecular Dynamics (IMD, section 2.2.1, [84]) was the main tool to obtain the results of this work. MD is a classical simulation method on an atomistic level where Newton's equations of motion for a set of N atoms,

$$\frac{d\mathbf{p}_i}{dt} = \mathbf{F}_i(\{\mathbf{r}_i\}) \quad (i = 1, .., N), \tag{2.20}$$

are solved numerically. In general, this $3N$-dimensional system of differential equations cannot be solved exactly. Hence, the integration is approximated by discretizing time. For a given configuration (N atoms with masses m_i and momenta $\mathbf{p}_i^0$ at positions $\mathbf{r}_i^0$) at a given time t^0 (assuming the forces $\mathbf{F}_i$ on each atom i as known), new positions $\mathbf{r}_i$ of each atom at time $t = t^0 + \Delta t$ can be determined in two steps:

$$\mathbf{p}_i = \mathbf{p}_i^0 + \Delta t \; \mathbf{F}_i(\{\mathbf{r}_i\}), \tag{2.21}$$

$$\mathbf{r}_i = \mathbf{r}_i^0 + \Delta t \; \frac{\mathbf{p}_i}{m_i}. \tag{2.22}$$

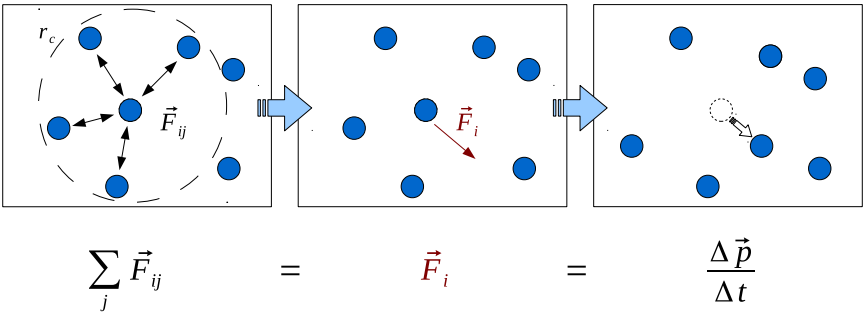

Figure 2.2.: Schematic atom movement depicted for atom i in the center of the shown box. First the total force $\mathbf{F}_i$ on atom i is determined by summing up all pair forces $\mathbf{F}_{ij}$ inside of a cutoff sphere defined by the cutoff radius r_c. Then atom i is moved to its new position. In simulation, all atoms are moved simultaneously. Vectors are distinguished with arrows inside of the graph.

After each new position is obtained, all atoms are advanced simultaneously. Δt has to be chosen in a way, that the relevant atomic processes can be resolved during simulation. This condition typically yields femtosecond time scales.

The forces in Eq. (2.21) are assumed to be known. They are determined by effective interaction force fields, which are described in detail in section 2.3. The force field is the most crucial part of an MD simulation and mainly determines the quality of the results. For pairwise interactions, the total force on each atom is given by the superposition of all pair forces. The atomic movement is depicted schematically in figure 2.2. A cutoff radius r_c is introduced to yield linear scaling of computational effort in the number of particles instead of $O(N^2)$. In most cases, this is sufficient due to the short-range nature of interatomic forces. Typical interactions are only relevant in the range of 2-4 atomic distances.

Interactions in metal oxides are dominated by electrostatic forces due to the presence of electrostatic charges and dipoles. They are long-ranged and thus do not conform to the approach of truncating interactions. Hence, electrostatic forces have to be treated separately, which is shown in detail in chapter 3.

In a common MD simulation, the number of particles N is constant.

Integrating Newton's equations of motion additionally conserves volume and energy (NVE or microcanonical ensemble). It is, however, also possible to control temperature instead of energy (NVT or canonical ensemble) and pressure instead of volume (NPT ensemble). Conserving temperature and/or pressure during simulation is put into effect by adding terms to Eq. (2.21), that can be taken as an external heat and/or volume reservoir.

Mapping bulk materials to a computer simulation by introducing periodic boundary conditions is easier than in the case of quantum mechanics (section 2.1.7). In MD simulations, the given box of particles is copied and added in each spatial direction in order to provide interaction partners also for atoms sitting near to the edge of the box. In contrast to ab initio methods, it is also possible to define open boundaries.

2.2.1. ITAP Molecular Dynamics (IMD)

IMD [84] was created at the Institut für Theoretische und Angewandte Physik (ITAP) in Stuttgart. It is primarily specialized in condensed matter systems and hence the most suitable MD code for the applications of this thesis. Above all, it is still under active development [36]; thus it has been fine-tuned to optimally treat the individual tasks yielding the present results.

IMD is able to treat millions of atoms [76] due to its parallelization performance. The Message Passing Interface (MPI) is included to transfer data from one processor to another. For limited-range interactions, IMD provides linear scaling up to thousands of CPUs. It uses a combination of link cells and neighbor lists where the former are used to compute the latter in an efficient way. Parallelization is done via fixed geometric domain decomposition, where each CPU gets an equal block of material. This approach is sufficient as long as the simulated system is not too heterogeneous, which is always fulfilled in the present studies of condensed matter. For the force computation, atoms at the surface of a block are exchanged with the neighboring CPUs. A two-dimensional scheme of the link cell approach is shown in figure 2.3.

IMD can handle both tabulated and analytical potentials, from which the forces on each atom are computed. The latter are tabulated once only at the beginning of simulation. Between points of support, cubic splines are applied for interpolation. In IMD, a huge number of force field types are implemented (pair, covalent, EAM, electrostatics (see chapter 3)).

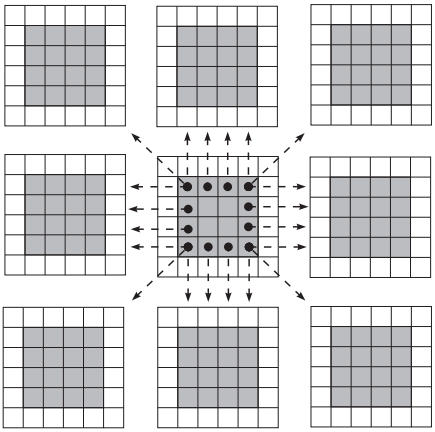

Figure 2.3.: Two-dimensional example of link cells. Each CPU gets one block of cells. The white cells are buffer cells. The surface cells (dotted in the center block) exchange data with neighboring blocks. From [84].

The numerical integration of Newton's equations of motion is accomplished by the Verlet algorithm, which is based on equations (2.21) and (2.22). The external heat reservoir for simulations with NVT ensemble is given by a Nosé-Hoover thermostat [62]. In a similar way, a barostat is available to achieve NPT conditions. IMD also provides integrators for relaxation simulations. Thereby, after each step the velocity components of all atoms are reset to zero in each direction except for the one oriented towards the minimum in the potential landscape.

During a simulation, IMD is able to write out full trajectories of each particle (positions and velocities at each timestep). From this, the *partial* vibrational density of states (VDOS) G_μ(E) for atom type μ can be obtained by computing the Fourier transform of the time-dependent velocity-velocity autocorrelation function with the post-processing software package nMoldyn [75]. The *generalized* VDOS $G(E)$ is then calculated by

$$G(E) = \sum_\mu \frac{\sigma_\mu}{m_\mu} G_\mu(E) \tag{2.23}$$

with the scattering cross section σ_μ and atomic mass m_μ of atom μ. If a VDOS curve shall be compared to experimental results, sometimes a

certain adjustment is needed due to inadequatenesses of the classical atomic approach (negligence of quantum phenomena). Also when comparing to ab initio results, some correction is required, because ab initio calculations are not able to study full phononic trajectories due to timescale restrictions. There, often the harmonic approximation is used to find the VDOS. In all cases, it is common to introduce a global, constant relative frequency scaling for the MD curves,

$$\omega = (1 + \gamma)\omega', \tag{2.24}$$

where ω' is the original eigenfrequency, ω the scaled frequency, and γ the constant relative frequency scaling.

In IMD, almost arbitrary boundary conditions are available. They can also be combined (e.g. applied in chapter 7). Plenty of other options are supported in IMD; detailed descriptions can be found in [36].

2.2.2. Ab initio molecular dynamics

Another atomistic approach, which aims for considering the quantum nature of matter, is the ab initio MD. The procedure is to treat the core system classically while providing the forces directly from first-principles calculations (as described in section 2.1.6). Thus, dynamic ab initio simulations are possible. There exist several approaches which are based on the following briefly introduced idea: Already in density functional theory (section 2.1.1), nuclear and electronic equations of motion are decoupled according to the Born-Oppenheimer approximation. The ab initio MD takes advantage of the different time scales of the two systems. After each MD time step, where the nuclei are moved to new positions, the new forces on each nucleus are calculated fully quantum mechanical according to the electronic behavior discussed in section 2.1. Ab initio MD is many orders in magnitude slower compared to pure classical MD. However, it can be used for creating reference data structures for the force field generation (section 2.3). Starting with an input configuration as in the static case, an ab initio MD trajectory can be obtained. Each nucleus time step yields a new checkpoint which can be included in the reference database. This allows to include structures with a finite temperature and even short trajectories of a structure into the ab initio reference data base. For example, such a temperature trajectory is applied in the α-alumina force field generation (see section 5.3.1).

2.3. Force field generation

In MD simulations, Newton's equations of motion can be solved numerically (section 2.2) provided that the forces on each atom are known. This is realized by force fields that include all interactions and energy contributions from the electronic system. They can be obtained by fitting ab initio, empirical and/or experimental data into its generation. The most direct and full non-empirical approach is to solely allow first-principles input to enter the generation. This is maintained for each force field the present thesis deals with.

2.3.1. Effective potentials

In general, a full many-body interaction potential $V(\{\mathbf{r}_i\})$, which depends on the atomic coordinates $\{\mathbf{r}_i\}$ of N atoms, can be expanded into multibody contributions:

$$V(\{\mathbf{r}_i\}) = \sum_{i}^{N} V_1(\mathbf{r}_i) + \sum_{i}^{N}\sum_{j\neq i}^{N-1} V_2(\mathbf{r}_i,\mathbf{r}_j) + \sum_{i}^{N}\sum_{j\neq i}^{N-1}\sum_{k\neq i,j}^{N-2} V_3(\mathbf{r}_i,\mathbf{r}_j,\mathbf{r}_k) + \ ... \tag{2.25}$$

There exist various approaches depending on the particular bond situation, which introduce an effective interaction potential V^{eff} and aim for a preferably accurate approximation of $V(\{\mathbf{r}_i\})$:

- The widely-used form is a *pair potential*, that neglects many-body terms and hence tries to map all interactions into the second term of expansion (2.25). This approach is the most basic one. For instance, it yields accurate results for noble gas solids where Van-der-Waals interactions are dominant. Due to its simplicity, a pair potential allows the fastest simulations, but is often insufficient where many-body effects play an important role.

- More advanced is the *embedded atom method (EAM)* where in addition to pairwise terms an embedding function depending on the electron density enters the force field. This mimics many-body, but still isotropic interactions. Mainly metals are treated with EAM potentials, because they are able to accurately represent the free electronic system.

- If directional interactions have to be taken into account and angles between bonds become relevant (for example in covalent systems), expansion (2.25) can be truncated after the third term. Hence, real three-body terms enter the force field, which costs more computational time than simple pair potentials. These aproaches are known as *multi-body potentials*. Also *angular dependent potentials* can be assigned to this class of force fields.

- The present work presents MD studies of ionic systems. Hence, the force fields have to treat *electrostatic interactions*. They consist of isotropic pair and multi-body dipolar terms and are detailed in chapter 3.

Plenty of advanced potential models are available (also in IMD), which will not be discussed here. Let a selected effective interaction potential be given. Then, the forces required for Eq. (2.21) are obtained by taking the negative gradient of the potential function V^{eff} with respect to the atomic coordinates in either case.

Unfortunately, the effective potential approach in no way yields an all-round force field. A potential can only be generated for one material with a certain stoichiometry and for a certain area of its phase diagram. The range for which a potential is optimized, is determined by the selection of reference data. The broader a dataset is prepared (wide temperature and pressure range), the less precisely the force field works. On the other hand a potential is rarely required with huge accuracy at one point in the phase diagram, which, however, yields wrong results outside the range for which it was optimized. In each case, a compromise between precision and transferability has to be found.

2.3.2. Generation with potfit

The program potfit [70] was originally developed by Peter Brommer [8, 9] and is now maintained at the ITAP in Stuttgart. It is a free, open-source software published under the GNU General Public License (GPL). Full details of the basic functions and a flowchart of the framework can be found in [7]. potfit generates an effective atomic interaction force field solely from ab initio reference structures. The potential parameters are optimized by matching the resulting forces, energies and stresses to according first-principles values with the force matching method [16]. All reference

structures used in this study were prepared with VASP (section 2.1.7). The generated force fields are directly exported to IMD (section 2.2.1).

For N_m particles, reference configuration m provides one energy e^0_m, six components of the stress tensor $s^0_{m,l}$ $(l = 1, 2, .., 6)$ and $3N_m$ total force cartesian components $f^0_{m,n}$ $(n = 1, 2, ..., 3N_m)$ on N_m atoms. The function

$$Z = w_e Z_e + w_s Z_s + Z_f \tag{2.26}$$

is minimized with respect to the potential parameters. Here

$$\begin{aligned} Z_e &= 3 \sum_{m=1}^{M} N_m (e_m - e^0_m)^2, \\ Z_s &= \frac{1}{2} \sum_{m=1}^{M} \sum_{l=1}^{6} N_m (s_{m,l} - s^0_{m,l})^2, \\ Z_f &= \sum_{m=1}^{M} \sum_{n=1}^{3N_m} (f_{m,n} - f^0_{m,n})^2, \end{aligned} \tag{2.27}$$

and e_m, $s_{m,l}$ and $f_{m,n}$ are the corresponding values calculated with the parametrized force field. w_e and w_s are certain weights to balance the different amount of available data for each quantity. In the following, M reference structures are assumed that all consist of the same number of particles ($N_m = N$), but in principle, potfit can handle different numbers of particles for each reference structure. The root mean square (rms) errors,

$$\Delta F_e = \sqrt{\frac{Z_e}{3MN}} \quad , \quad \Delta F_s = \sqrt{\frac{2Z_s}{MN}} \quad \text{and} \quad \Delta F_f = \sqrt{\frac{Z_f}{MN}}, \tag{2.28}$$

are first indicators of the quality of the generated force field. Its magnitudes are independent of weighting factors, number and sizes of reference structures. For the minimization of the function Z, a combination of a stochastic simulated annealing algorithm [12] and a conjugate-gradient-like deterministic algorithm [71] are used. Details and flowcharts of both algorithms can be found in [7]. potfit is parallelized using the standard MPI by distributing the reference configurations on the processors. Generation details for each force field are given in chapter 5.

Chapter 3.

Electrostatics

The bond situation in metal oxides can be described by the concept of ionic solids where the charge density of each ion is mainly localized close to its core and is almost isotropically. The interactions between the ions can be modelled with basic Coulomb interactions. Although there is no need for non-isotropic approaches like angular-dependent potentials, simple pair potentials are not able to yield an accurate modelling in MD simulations (see chapter 6). The following sections serve with answers for how to treat long-range electrostatic forces in MD simulations and how to enhance pair potentials to yield an accurate description of metal oxide systems.

3.1. Long-range interactions

The electrostatic interactions in condensed matter systems are long ranged. Hence, a huge cut-off (or even an infinite one at worst) would be required, if one wanted to sum up all Coulomb forces directly. This would lead to massive computational costs. When using a link cell algorithm as in IMD to run a simulation in parallel, further problems would arise, because a cell decomposition is designed for short-range interactions. In the last thirty years, many high-performance approaches have been developed to improve simulations of systems with long-range interactions. These Coulomb solvers are briefly discussed in the following section to point out why Wolf summation [97] was chosen for the present work.

3.1.1. Overview: Coulomb solver

Solving problems with long ranged forces in particle simulations originates from the ninety year old Ewald summation method [6]. The Ewald idea is to split the interactions into a short-range and a smooth part and evaluate

the latter in Fourier space. The scaling of the computational effort with the number of particles is $O(N^{3/2})$ at best. In addition, Ewald summation requires periodic boundary conditions due to the Fourier transformation. Because Ewald summation is also the initial point for Wolf summation, it is described in detail in section 3.1.2.

Most of the modern and established Coulomb solver can be classified in the following three types (an extensive presentation can be found in [23]):

- *Grid based methods*: Point of origin is the Ewald summation, but the reciprocal-space Fourier sum is replaced by a Fast-Fourier-Transformation (FFT). In the FFT, the charges of the smooth part are transfered to a discrete lattice. Then the Poisson equation is solved on the lattice. After that, the electric field is interpolated back to the atoms. Most of these approaches require periodic boundary conditions and yield $O(N\log N)$ scaling with the number of particles. It is assumed that the $\log N$-factor only becomes relevant for high particle numbers compared to linear-scaling methods.

- *Tree based methods*: The idea is to combine distant particles into groups and consider only their far field. The potential of the charge density of each group is expanded into multipoles (see Eq. (3.12)). After that, the interaction of a particle with each multipole of each group is evaluated. In contrast to Fourier based methods, open boundaries are required in most of the available implementations. Depending on the particular method, the scaling with the number of particles is $O(N)$ or $O(N\log N)$. The linear scaling, however, comes with some overhead due to the expensive pre-computing of the multipoles. Hence, most multipole based methods become only efficient for large particle numbers.

- *Direct methods*: The most simple way is to sum up all interactions directly, which yields $O(N^2)$-scaling at best. If it is possible to find a certain cut-off radius, all advantages of short-range interactions (linear scaling, compatibility with cell decomposition algorithms, easy implementation in existing code) become accessible. One possibility is the reaction field method [2], which defines a sphere around each atom within which the Coulomb interactions are treated explicitly. Outside of this sphere, the medium is assumed to have a uniform dielectric constant. This approach, however, requires periodic bound-

ary conditions. If the system under study is not too heterogeneous, there indeed exists a method introduced by Wolf *et al.* in 1999 [97], which shows a way to put into practice the approach of mapping eletrostatics solely onto short-range-like interactions. Hence, almost arbitrary boundary conditions can be applied.

In summary, the Wolf summation method is easily implemented in IMD and is compatible with the existing cell decomposition algorithm. The Wolf sum yields $O(N)$-scaling in the number of particles, accessibility of almost arbitrary boundary conditions and efficiency independent on the system size.

3.1.2. Ewald summation

In metal oxides, the ions carry some charge q_i and interact with a Coulomb potential. This leads to the classical Madelung problem [53]: determining the energy of a condensed system with pairwise r^{-1} interactions. The convergence properties of the resulting sum require a special treatment. The Ewald method [19] assures rapid convergence for the total Coulomb energy of a set of N ions with charges q_i at positions $\mathbf{r}_i$ that are part of an infinite system of point charges,

$$U^{qq} = \frac{1}{2} \sum_{i=1}^{N} \sum_{\substack{j=1 \\ j \neq i}}^{\infty} \frac{q_i q_j}{r_{ij}}, \tag{3.1}$$

(where $\mathbf{r}_{ij} = \mathbf{r}_j - \mathbf{r}_i$ and $r_{ij} = |\mathbf{r}_{ij}|$) by a mathematical trick. Firstly, structural periodicity of linear size L is artificially imposed on the system, and in the resulting expression a decomposition of unity of the form

$$1 = \operatorname{erfc}(\kappa r) + \operatorname{erf}(\kappa r) \tag{3.2}$$

is inserted. The error function is defined as

$$\operatorname{erf}(\kappa r) := \frac{2}{\sqrt{\pi}} \int_0^{\kappa r} dt\, e^{-t^2}. \tag{3.3}$$

The Ewald splitting parameter κ controls the distribution of energy contributions between the two terms. Thus, Eq. (3.1) can be written as

$$U^{qq} = \frac{1}{2}\sum_{i=1}^{N}\sum_{j=1}^{N}\sum_{\mathbf{n}=\mathbf{0}}^{\infty}{}' \frac{q_i q_j}{|\mathbf{r}_{ij}+\mathbf{n}L|}\left[\mathrm{erfc}(\kappa|\mathbf{r}_{ij}+\mathbf{n}L|) + \mathrm{erf}(\kappa|\mathbf{r}_{ij}+\mathbf{n}L|)\right], \tag{3.4}$$

where the sum over periodic images $\mathbf{n}$ is primed to indicate that the $i = j$ term is to be omitted for $\mathbf{n} = \mathbf{0}$. Taking the Fourier transform of the erf expression only, but not of the erfc term, one can convert the conditionally convergent total energy Eq. (3.1) into the sum of real-space and reciprocal-space contributions $U_{\mathbf{r}}^{qq}$ and $U_{\mathbf{k}}^{qq}$ where each of these converges rapidly.

The Ewald trick can be depicted as a smearing of the delta-shaped charge densities by Gaussians of width κ. This relationship can be easily verified: Inserting a potential of the form $V(r) \sim \frac{\mathrm{erfc}(\kappa r)}{r}$ in Poisson's equation yields a Gaussian density of width κ. The Gaussians can be treated in real-space and the correction terms emerging from this are solved in the reciprocal space.

The downside to the Ewald summation method is the scaling of the computational effort with the number of particles in the simulation box: Even when the balance between real- and reciprocal-space contributions controlled by κ is optimized, the computational load increases at best as $O(N^{3/2})$ [20].

3.1.3. Wolf summation

Wolf *et al.* [97] proposed a direct summation technique with linear scaling ($O(N)$) for Coulomb interactions. This so called Wolf summation takes into account the physical properties of the systems under study. To this end, one looks at the Fourier transform of the erf term of Eq. (3.4),

$$U_{\mathbf{k}}^{qq} = \frac{2\pi}{L^3}\sum_{\mathbf{k}\neq\mathbf{0}}\sum_{i,j}\left[q_i q_j e^{i\mathbf{k}\cdot\mathbf{r}_{ij}}\,\frac{\exp\left(-k^2/4\kappa^2\right)}{k^2}\right] - \frac{\kappa}{\pi^{1/2}}\sum_i q_i^2, \tag{3.5}$$

where the self term ($\mathbf{n} = \mathbf{0}$ and $i = j$) is first included in the summation and then subtracted. Eq. (3.5) can be rewritten as

$$U_{\mathbf{k}}^{qq} = \sum_{\mathbf{k}\neq\mathbf{0}} S(\mathbf{k})\frac{\exp\left(-k^2/4\kappa^2\right)}{k^2} - \frac{\kappa}{\pi^{1/2}}\sum_i q_i^2, \tag{3.6}$$

where

$$S(\mathbf{k}) = \frac{2\pi}{L^3} \left| \sum_j q_j \exp(i\mathbf{k} \cdot \mathbf{r}_j) \right|^2 \tag{3.7}$$

is the charge structure factor, $k = |\mathbf{k}|$ and V volume of the simulation box. The charge structure factor is the Fourier transform of the charge-charge autocorrelation function.

In liquid systems and largely also in solids, there are no long-range charge fluctuations; the charges form a cold dense plasma, screening each other. This means that for small amplitudes of the wave vectors $\mathbf{k}$ the charge structure factor is also small. If one now chooses a sufficiently small splitting parameter κ, the reciprocal-space contribution can be neglected altogether. As κ is linked to the real-space cut-off r_c, however, this might require a cut-off radius which is substantially larger than the range of traditional short-range interactions like in metals.

Concurrently, Wolf *et al.* also motivated a continuous and smooth cut-off of the remaining Coulomb potential

$$E^{qq} = \frac{1}{2} \sum_{i=1}^{N} \sum_{\substack{j=1 \\ j \neq i}}^{\infty} \frac{q_i q_j}{r_{ij}} \mathrm{erfc}(\kappa r_{ij}) \tag{3.8}$$

at a cut-off radius r_c:

$$\tilde{E}^{qq}(r_{ij}) = E^{qq}(r_{ij}) - E^{qq}(r_c) - (r_{ij} - r_c) \left. \frac{dE^{qq}}{dr_{ij}} \right|_{r_c} . \tag{3.9}$$

The cut-off is called *smooth*, if both energy function and its first derivative (applied for force calculation) vanish at the cut-off sphere. The latter is realized by the last term in Eq. (3.9) and is required in MD simulations. Otherwise, atoms crossing the threshold might get unphysical kicks.

In general (independent of damping factors), shifting the pair potential so that it goes to zero at $r = r_c$ is equivalent to neutralizing the net charge in a spherically truncated system: For a given charge q_i and an interaction cut-off radius r_c, the net charge inside of the cut-off sphere is

$$\Delta q_i = \sum_j q_j \tag{3.10}$$

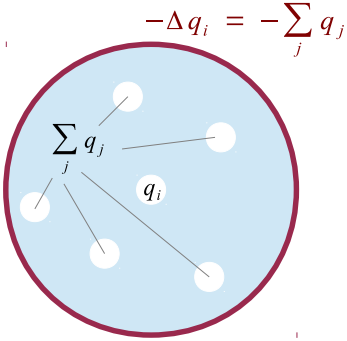

Figure 3.1.: For a given charge q_i, the net charge inside of the cut-off sphere, Δq_i, is neutralized by distributing $-\Delta q_i$ isotropically over the spherical surface.

(with q_j the other charges inside of the sphere). Let a screening be assumed with the negative net charge placed isotropically on the cut-off sphere, so that the enviroment of q_i is neutralized. The interaction of q_i with the sphere yields an additional term to the total Coulomb energy,

$$U_i^{\text{screen}} = -\frac{q_i \Delta q_i}{r_c} = -\sum_j \frac{q_i q_j}{r_c} = -U_i^{qq}(r_c) = \text{const}, \tag{3.11}$$

which is identically to a constant shift. This relationship is clarified in figure 3.1.

The combination of (i) shifting the potential so that it vanishes smoothly at the cut-off, and (ii) damping the Coulomb potential to reduce the required cut-off radius, but only so weakly that the reciprocal-space term can still be neglected, is called Wolf summation. The Wolf method is implemented both in IMD (by Peter Brommer) and in potfit (by the author). The explicit Wolf shifted and truncated Coulomb energy expression is given in appendix A.

3.1.4. Error estimation and scaling properties

The Ewald summation is well established for many decades. It is able to reproduce analytical results (for instance Madelung constants) with high

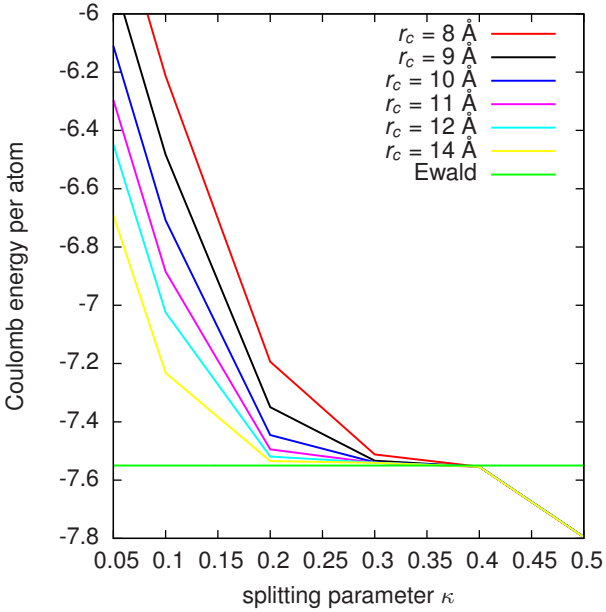

Figure 3.2.: Coulomb energy per atom taken from a simulation of liquid magnesia with Wolf summation (force field from chapter 6). The results strongly depend on the choice of both cut-off radius r_c and splitting parameter κ. The right choice results in a plateau of the correct energy. The Ewald result is plotted as a reference. For $\kappa > 0.4$, all curves are nearly undistinguishable.

accuracy. Hence, it can be used to validate the Wolf summation technique. Compared to Ewald, the Wolf method is an approximation, because the reciprocal-space term is neglected and the real space part has been shifted. Figure 3.2 shows, that the Wolf sum is nevertheless in accurate agreement compared to the Ewald sum provided that both cut-off radius r_c and splitting parameter κ are chosen suitably. The smaller κ is chosen, the bigger becomes the reciprocal-space contribution and the larger is the error made by neglecting the latter. The larger κ is chosen, the stronger becomes the damping of the real-space term, which introduces an error compared to the undamped Coulomb energy. For $\kappa > 0.4$, the strong damping yields a

deviation from the Ewald result which is nearly independent of the chosen cut-off radius. This behavior can be seen in figure 3.2: For $\kappa > 0.4$, all curves are nearly undistinguishable. Between these two scenarios, a trade-off can be found, which results in an energy plateau that is in accordance with the Ewald result. Not surprisingly, the plateau is expanded for larger cut-off radii. For each force field, such a plateau has to be found to allow for accurate simulation results.

To judge the performance of the Wolf summation, the CPU cost of simulating a system of point charges (liquid silica; force field introduced in chapter 6) is shown in figure 3.3. It is compared to the P3M (particle-particle/particle-mesh) [15] method, a present-day grid based approach implemented in the MD code ESPResSo [48]. It can be seen, that the computational effort with Wolf summation scales perfectly linear up to 2.5 million particles. For smaller systems (fewer than about 80 000 particles), ESPResSo is faster due to the short real-space cut-off required for P3M. However, as the system becomes larger, the $O(N\log N)$-scaling of P3M loses to the linear scaling of Wolf. As a reference, also the CPU cost of the Ewald method in IMD is shown. The accuracy of each method is chosen to 10^{-3}. It is obtained by the error estimation of Kolafa and Perram [42] (It has to be mentioned, that this error estimation is not able to account for the negligence of the reciprocal-space term in the Wolf case). The scaling simulations were all performed on a single 2.83 GHz Intel Nehalem CPU.

3.2. Induced electrostatic dipole moments

In the last seven years, several MD studies [31, 78] showed, that simple pair potentials composed of a short-range and a Coulomb term are often not able to model structural and dynamic properties of ionic condensed matter systems accurately. Hence, the description of electrostatic interactions has to be extended. So far, only monopole charges have been taken into account. This is equivalent to a truncation of the multipole expansion for the potential of a charge density,

$$\varphi(\mathbf{r}) \;=\; \frac{q}{r} \;+\; \frac{\mathbf{rp}}{r^3} \;+\; \frac{1}{2}\sum_{ij} Q_{ij}\frac{x_i x_j}{r^5} \;+\; \ldots\,, \tag{3.12}$$

after the first order ($r = |\mathbf{r}|$, x_i component of $\mathbf{r}$, q total charge, $\mathbf{p}$ dipole term and Q_{ij} quadrupole term). In the following, the model by Tangney and

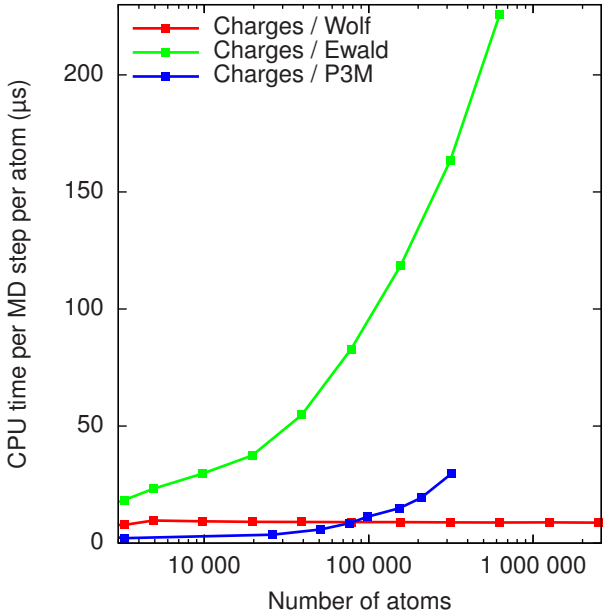

Figure 3.3.: Scaling of computational effort with system size in liquid silica for Wolf, P3M and Ewald. P3M is faster for systems with less than 80 000 atoms. In larger systems, Wolf summation performs better.

Scandolo (TS) [88] is introduced, which considers monopole charges and in addition dipole moments (first and second order terms of expansion Eq. (3.12)) for each oxygen ion. The validation of the force fields presented in this thesis (chapter 5) shows that there is no need for taking higher electrostatic moments into account, which would be computationally very expensive. In chapter 6, it is systematically investigated where the effects of electric dipole moments are important and how the impact arises from additional interaction mechanisms.

3.2.1. Tangney-Scandolo-model

The TS potential contains two contributions: a short-range pair potential of Morse-Stretch (MS) form, and a long-range part, which describes the

electrostatic interactions between charges and induced dipoles on the oxygen atoms. The MS interaction between an atom of type i and an atom of type j has the form

$$U_{ij}^{\mathrm{MS}} = D_{ij}\left[\exp[\gamma_{ij}(1-\frac{r_{ij}}{\rho_{ij}})] - 2\exp[\frac{\gamma_{ij}}{2}(1-\frac{r_{ij}}{\rho_{ij}})]\right], \tag{3.13}$$

with $r_{ij} = |\mathbf{r}_{ij}|$, $\mathbf{r}_{ij} = \mathbf{r}_j - \mathbf{r}_i$ and the model parameters D_{ij}, γ_{ij} and ρ_{ij}, which have to be optimized.

The dipole moments depend on the local electric field of the surrounding charges and dipoles. Hence a self-consistent iterative solution has to be found. In the TS approach, a dipole moment $\mathbf{p}_i^n$ at position $\mathbf{r}_i$ in iteration step n consists of an induced part due to an electric field $\mathbf{E}(\mathbf{r}_i)$ and a short-range part $\mathbf{p}_i^{\mathrm{SR}}$ due to the short-range interactions between charges q_i and q_j. Following Rowley *et al.* [77], this contribution is given by

$$\mathbf{p}_i^{\mathrm{SR}} = \alpha_i \sum_{j\neq i} \frac{q_j \mathbf{r}_{ij}}{r_{ij}^3} f_{ij}(r_{ij}) \tag{3.14}$$

with

$$f_{ij}(r_{ij}) = c_{ij} \sum_{l=0}^{4} \frac{(b_{ij} r_{ij})^l}{l!} e^{-b_{ij} r_{ij}}. \tag{3.15}$$

$f_{ij}(r_{ij})$ was introduced *ad hoc* to account for multipole effects of nearest neighbors and is a function of very short range. b_{ij} is the reciprocal of the length scale over which the short-range interaction comes into play, c_{ij} determines amplitude and sign of this contribution to the induced moment. Together with the induced part, one obtains

$$\mathbf{p}_i^n = \alpha_i \mathbf{E}(\mathbf{r}_i; \{\mathbf{p}_j^{n-1}\}_{j=1,N}, \{\mathbf{r}_j\}_{j=1,N}) + \mathbf{p}_i^{\mathrm{SR}}, \tag{3.16}$$

where α_i is the polarizability of atom i and $\mathbf{E}(\mathbf{r}_i)$ the electric field at position $\mathbf{r}_i$, which is determined by the dipole moments $\mathbf{p}_j$ in the previous iteration step. As a convergence criterion, the rms error of all dipole moments between two consecutive iteration steps has to be smaller than a definable threshold Δp:

$$\frac{1}{N}\sqrt{\sum_i (\mathbf{p}_i^n - \mathbf{p}_i^{n-1})^2} \overset{!}{<} \Delta p. \tag{3.17}$$

Considering the interactions between charges U^{qq} (Eq. (3.1)), between dipole moments,

$$U^{pp} = \frac{1}{2} \sum_{\substack{i,j \\ j \neq i}}^{N} \left[\frac{3(\mathbf{r}_{ij}\mathbf{p}_i)(\mathbf{r}_{ij}\mathbf{p}_j)}{r_{ij}^5} - \frac{\mathbf{p}_i\mathbf{p}_j}{r_{ij}^3} \right], \tag{3.18}$$

and between a charge and a dipole,

$$U^{pq} = \frac{1}{2} \sum_{\substack{i,j \\ j \neq i}}^{N} \frac{q_i(\mathbf{r}_{ij}\mathbf{p}_j)}{r_{ij}^3}, \tag{3.19}$$

the total electrostatic contribution is given by

$$U^{\mathrm{EL}} = U^{qq} + U^{pq} + U^{pp}, \tag{3.20}$$

and the total interaction is

$$U^{\mathrm{tot}} = U^{\mathrm{MS}} + U^{\mathrm{EL}}. \tag{3.21}$$

The TS model is implemented both in IMD (by Peter Brommer) and potfit (by the author, details of the implementation are shown in appendix B). potfit accepts the TS force field parameters as value to be optimized. The MS potential Eq. (3.13) is defined by three parameters for each pair of interaction partners ij. Including the charges q_i, the polarizability α of the oxygen ion and the parameters b_{ij} and c_{ij}, which only differ from zero in the case $i \neq j$, there are 14 paramters for a binary oxide. The requirement of charge neutrality reduces the number of free parameters by one. Thus, there are 13 parameters to optimize. Details of the parameter optimization for each force field are shown in chapter 5.

3.2.2. Validation

Each force field generated in the framework of this thesis is intensively validated (see chapter 5). The highly accurate results presented there show that there is no need for embedding or even many-body or angular dependent potential terms. The dipole field provides for multi-body interactions while keeping the linear scaling in the number of particles.

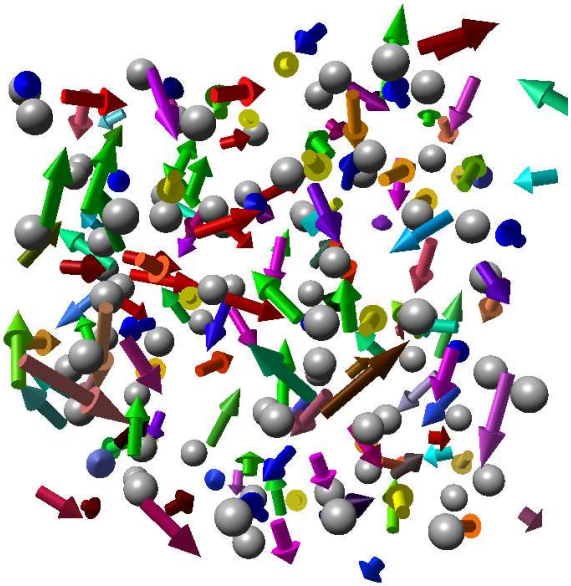

Figure 3.4.: Silica melt at 3100 K: Each silicon atom is depicted as a grey sphere, each oxygen atom is represented by an arrow showing magnitude and direction of its dipole moment. The color coding emphasizes the orientation. No correlated orientation of dipole moments can be observed.

Here, however, it is analyzed, whether the TS dipole model is able to describe the desired dipole properties on a qualitative level. First, the total dipole moment of a liquid silica sample (4896 atoms at 3100 K, force field introduced in section 5.1) is calculated and averaged over a 200 picosecond simulation. There is at no time an appreciable spontaneous polarization. The averaged total dipole moment is $p^S_{\text{tot}} = 3.47 \times 10^{-28}$ Cm, which is small compared to a fully polarized system and thus can be taken as a fluctuation. In the case of liquid magnesia (5832 atoms at 5000 K, force field introduced in section 5.2), the averaged total dipole moment is $p^M_{\text{tot}} = 4.76 \times 10^{-33}$ Cm, which is even smaller than that of silica. In both cases, the result is as expected: On average, no correlated orientations of dipole moments are observed (see figure 3.4). Secondly, the trajectory of several

randomly selected dipole moments is traced, as well with the expected result: The dipole moments do not change their direction discretely, but gyrate continuously while the respective ion moves through the simulation box.

3.3. Wolf summation of dipole contributions

The direct Wolf summation method was introduced in section 3.1.3 for determining the energy of a condensed system with Coulomb interactions. Let now N dipole moments $\mathbf{p}_i$ at positions $\mathbf{r}_i$ be given. The total interaction can be written as

$$U^{pp} = -\frac{1}{2}\sum_{\substack{i,j \\ j\neq i}}^{N} \mathbf{p}_i^t (\nabla \otimes \nabla)\left(\frac{1}{r_{ij}}\right)\mathbf{p}_j. \tag{3.22}$$

Imposing structural periodicity and inserting the decomposition of unity of Eq. (3.2), Eq. (3.22) can be rewritten as

$$U^{pp} = -\frac{1}{2}\sum_{i,j}^{N}\sum_{\mathbf{n}=\mathbf{0}}^{\infty}{}' \mathbf{p}_i^t (\nabla \otimes \nabla)\left(\frac{\operatorname{erfc}(\kappa|\mathbf{r}_{ij}+\mathbf{n}L|)+\operatorname{erf}(\kappa|\mathbf{r}_{ij}+\mathbf{n}L|)}{|\mathbf{r}_{ij}+\mathbf{n}L|}\right)\mathbf{p}_j. \tag{3.23}$$

As in the case of charges, the total energy splits into a real- and a reciprocal-space part,

$$U^{pp} = U^{pp}_{\mathbf{r}} + U^{pp}_{\mathbf{k}}, \tag{3.24}$$

and the Fourier transform of

$$U^{pp}_{\mathbf{k}} = -\frac{1}{2}\sum_{i,j}^{N}\sum_{\mathbf{n}=\mathbf{0}}^{\infty} \mathbf{p}_i^t (\nabla \otimes \nabla)\left(\frac{\operatorname{erf}(\kappa|\mathbf{r}_{ij}+\mathbf{n}L|)}{|\mathbf{r}_{ij}+\mathbf{n}L|}\right)\mathbf{p}_j \tag{3.25}$$

is taken. The prime has been omitted, since the self term (for $\mathbf{n}=\mathbf{0}$ and $i=j$) is now finite. The resulting Fourier series is given by

$$U^{pp}_{\mathbf{k}} = \frac{2\pi N e^2}{V}\sum_{\mathbf{k}\neq\mathbf{0}}^{\infty} \mathbf{k}^t \underline{\mathbf{Q}}(\mathbf{k})\mathbf{k}\,\frac{\exp\left(-k^2/4\kappa^2\right)}{k^2}, \tag{3.26}$$

where V is the volume of the simulation cell and $\underline{\mathbf{Q}}(\mathbf{k})$ the dipole structure factor,

$$\underline{\mathbf{Q}}(\mathbf{k}) := \frac{1}{Ne^2} \sum_{i,j}^{N} \mathbf{p}_i \otimes \mathbf{p}_j \, e^{i\mathbf{k}\cdot\mathbf{r}_{ij}}, \tag{3.27}$$

with the normalization factor $1/\sqrt{Ne^2}$, where e denotes the elementary charge. As can be seen in Eq. (3.26), the large $\mathbf{k}$ contributions to $U_{\mathbf{k}}^{pp}$ tend to zero rapidly, whereas the small $\mathbf{k}$ contributions are governed by the behavior of $\mathbf{k}^t\underline{\mathbf{Q}}(\mathbf{k})\mathbf{k}$, which is expected to vanish as $k \to 0$. Hence, the reciprocal-space term of the dipole contribution can be neglected altogether as in the case of Coulomb energies.

3.3.1. Energy conservation

For the dipole contributions, the summation approach above was extended similarly to section 3.1.3. However, four tasks have to be included to ensure energy conservation during simulation, which are detailed in the following. The explicit Wolf shifted and truncated dipole energy expressions are given in appendix A.

Extended shifting

The dipole potential function and its first derivative also have to vanish at the cut-off radius. The dipole potential, however, is proportional to the first derivative of the Coulomb potential. Hence, the Coulomb potential and its first *two* derivatives must vanish at the cut-off radius. This yields the extended shifting, which replaces the prior one from Eq. 3.9:

$$\tilde{E}^{qq}(r_{ij}) = E^{qq}(r_{ij}) - E^{qq}(r_c) - (r_{ij} - r_c)\frac{dE^{qq}}{dr_{ij}}\bigg|_{r_c} - \frac{1}{2}(r_{ij} - r_c)^2 \frac{d^2E^{qq}}{dr_{ij}^2}\bigg|_{r_c}. \tag{3.28}$$

Dependence of potential on dipole moments

In MD simulations, the energy is conserved, if the forces on the particles are exactly equal to the negative gradient of the potential energy with respect to the atomic coordinates. Otherwise, the energy might oscillate or even drift off if not controlled by a thermostat. In standard MD simulations,

the requirement is usually automatically fulfilled: The forces are calculated as the derivative of the potential, which depends directly on the atomic positions. In the TS model, there is also an indirect dependence, as the potential is also a function of the dipole moments:

$$\varphi = \varphi(\{\mathbf{r}_i\}, \{\mathbf{p}_i(\{\mathbf{r}_j\})\}. \tag{3.29}$$

This would in principle lead to an extra contribution to the derivative of the potential,

$$\frac{d\varphi}{d\{\mathbf{r}_i\}} = \frac{\partial\varphi}{\partial\{\mathbf{r}_i\}} + \frac{\partial\varphi}{\partial\{\mathbf{p}_i\}}\frac{\partial\{\mathbf{p}_i\}}{\partial\{\mathbf{r}_j\}}, \tag{3.30}$$

which would be practically impossible to be determined effectively. Luckily, if the dipole moments are iterated until convergence is reached, the system is at an extremal value in the potential landscape, with $\partial\varphi/\partial\{\mathbf{p}_i\} = 0$, and so this part need not be evaluated. Imperfections in convergence may lead to a drift in the energy. Therefore, Δp in Eq. (3.17) was set to a value four orders of magnitude smaller than an ordinary moment in each iteration. Hence, an appreciable energy drifts not even occurred in long term simulations (simulation times longer than a nanosecond).

Conservation of differential relationship

All integer powers of r^{-1} are treated in a way to conserve the differential relationship between the functions (for example $r^{-2} = -\frac{d(r^{-1})}{dr}$). The Wolf damping modifies the r^{-n} relations:

$$r^{-1} \;\rightarrow\; r^{-1}\mathrm{erfc}(\kappa r) \;=:\; f_{-1}(r). \tag{3.31}$$

This changeover has to be translated consistently to all potential functions:

$$r^{-2} \;\rightarrow\; r^{-2}\mathrm{erfc}(\kappa r) + \frac{2\kappa\exp(-\kappa^2 r^2)}{\sqrt{\pi}r} \;=:\; f_{-2}(r) \tag{3.32}$$

$$\Rightarrow\; f_{-2}(r) \;=\; -\frac{d(f_{-1}(r))}{dr}. \tag{3.33}$$

The need for conserving the differential relationship can most easily be explained with a simple one-dimensional example. Given are two oppositely charged point charges $\pm q$ at a mutual distance r. If the negatively charged one is polarizable with polarizability α, it will get a dipole moment $p = \frac{\alpha q}{r^2}$.

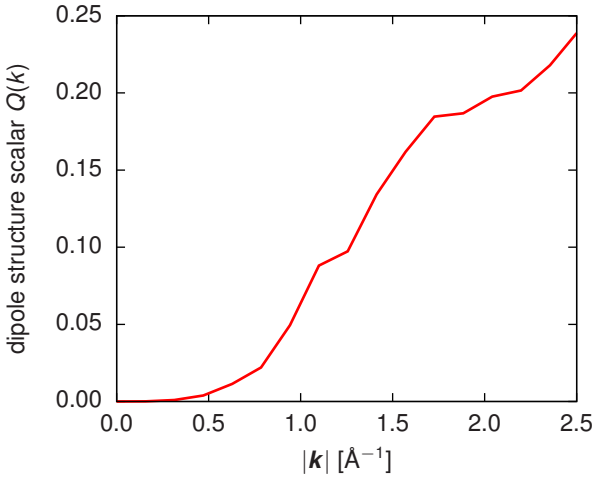

Figure 3.5.: k-dependence of the dipole structure scalar $Q(k)$ in liquid silica (4896 atoms, 3000 K). For small k, the dipole structure factor is negligible.

This leads to a total interaction energy (last term is the dipole self-energy contribution)

$$U = U^{qq} + U^{pq} + U^{pp} = -\frac{q^2}{r} - \frac{qp}{r^2} + \frac{p^2}{2\alpha}, \tag{3.34}$$

from which it follows that

$$\frac{\partial U}{\partial p} = -\frac{q}{r^2} + \frac{q}{r^2} = 0. \tag{3.35}$$

From here, it is visible, that modifying the differential relationship would annihilate the energy contribution condition explained in the previous task.

Correction due to short-range dipole moment

When applying the Wolf formalism to the TS potential, another issue arises concerning the energy contribution condition of the second task. The empirically introduced short-range part of each dipole moment (Eq. 3.14) also affects energy conservation. Hence, a correction term has to be added to

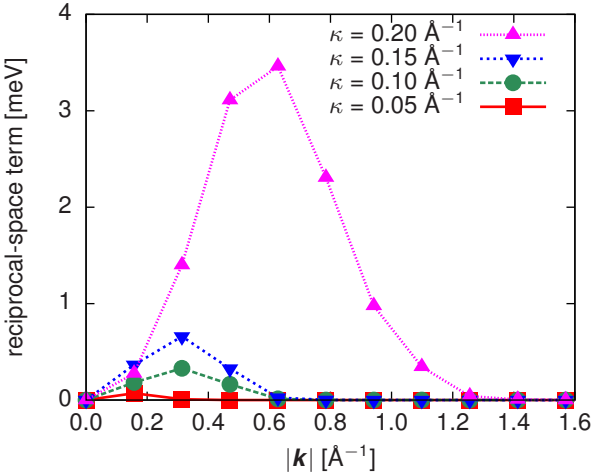

Figure 3.6.: k-dependence of the reciprocal-space term $U_{\mathbf{k}}^{pp}(k)$ for different splitting parameters κ. The $k \to 0$ behavior of $U_{\mathbf{k}}^{pp}(k)$ is governed by $Q(k)$, which results in negligible contributions of the small k-values to the total energy.

the total energy calculation. This also can most easily be explained with the same one-dimensional example of the previous task: The dipole moment in consideration of p^{SR} now becomes $p^{\mathrm{tot}} = p^{\mathrm{SR}} + p$. This leads to the total interaction energy

$$U = -\frac{q^2}{r} - \frac{qp^{\mathrm{tot}}}{r^2} + \frac{(p^{\mathrm{tot}})^2}{2\alpha} \tag{3.36}$$

from which it follows that

$$\frac{\partial U}{\partial p} = -\frac{q}{r^2} + \frac{p^{\mathrm{tot}}}{\alpha} = \frac{qf(r)}{r^2} \neq 0. \tag{3.37}$$

The correction term exactly counterbalances this additional contribution to ensure $\frac{\partial U}{\partial p} = 0$.

3.3.2. Error analysis and scaling properties

To legitimate the neglecting of the reciprocal-space term for the Wolf summed dipole contributions, liquid silica (4896 atoms, 3000 K, original

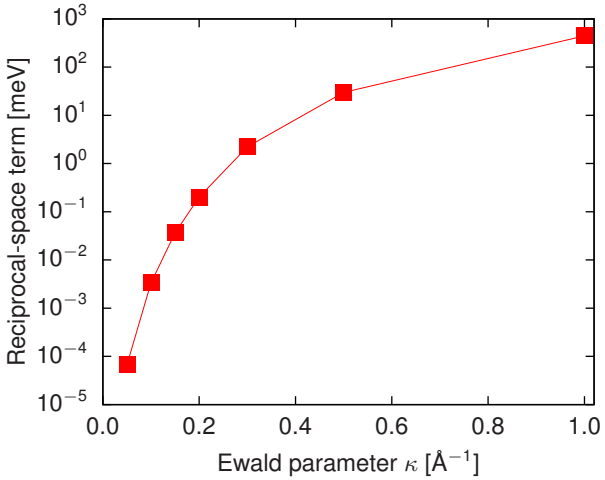

Figure 3.7.: Logarithmic plot of the Reciprocal-space term $U_{\mathbf{k}}^{pp}$ (equation (3.26)) for different splitting parameters κ. For sufficiently small κ, there is no noticeable contribution to the total energy compared to the real-space part.

TS force field from [88] with Wolf summation) has been simulated. It has to be analyzed, whether for a suitable κ the dipole structure factor is small. All values which are calculated in the course of this simulation are time-averaged over the full simulation time of one picosecond.

To analyze the $k \to 0$ behavior, the dipole structure scalar,

$$Q(k) = \langle \mathbf{k}^t \underline{\mathbf{Q}}(\mathbf{k}) \mathbf{k} \rangle_S, \tag{3.38}$$

is calculated. Angular brackets indicate an average over a spherical shell S with width Δk centered at constant $|\mathbf{k}| = k$. This averaging is necessary, because for a periodic system $\underline{\mathbf{Q}}$ is not a continuous function, but a discrete set, consisting of all reciprocal space vectors. Fig. 3.5 shows the dipole structure scalar. For small absolute values of k, $Q(k)$ goes to zero.

Fig. 3.6 shows the k-dependence of the reciprocal-space term,

$$U_{\mathbf{k}}^{pp}(k) = \frac{2\pi N e^2}{V} Q(k) \frac{\exp\left(-k^2/4\kappa^2\right)}{k^2}, \tag{3.39}$$

for different splitting parameters κ (again averaged over a spherical shell). As mentioned above, due to the exponential damping, large k-contributions are negligibly small, whereas the small-k values are governed by the behavior of $Q(k)$ as $k \to 0$.

Finally the sum in Eq. (3.26) is evaluated for the given k-mesh with truncation sphere in the reciprocal-space. The difference between this approach of a spherical truncation and the full summation is very small because of the exponential damping in Eq. (3.39), as seen in the rapid decay of $U_{\mathbf{k}}^{pp}(k)$ for increasing k in Fig. 3.6. In Fig. 3.7 the κ-dependence of the Reciprocal-space term $U_{\mathbf{k}}^{pp}$ is illustrated in a logarithmic plot (to distinguish between $U_{\mathbf{k}}^{pp}(k)$ and $U_{\mathbf{k}}^{pp}$, the latter is identified by capitalization of its name). For a chosen damping of $\kappa = 0.1\,\text{Å}^{-1}$, one gets

$$\frac{1}{N} U_{\mathbf{k}}^{pp} = 3.3\,\mu\text{e}V, \tag{3.40}$$

which is six magnitudes smaller than the real-space part and can thus be neglected.

The performance of the Wolf summed TS interactions (liquid silica, force field introduced in section 5.1) is depicted in figure 3.8. It is compared to Wolf summed Coulomb interactions (force field introduced in chapter 6). As a reference, the CPU cost of the Ewald and the P3M method for charges is shown again. Even with dipole contributions, the Wolf summation scales perfectly linear with system size up to 2.5 million particles. In the TS approach, hence, many-body effects are included without destroying the linear scaling properties obtained by the Wolf summation. The computational cost per atom of the TS model is independent of system size; compared to Coulomb charges, the TS model with Wolf summation in silica is slower by a factor of 2.6. The identical approach for liquid magnesia with force field from section 5.2 yields the same result: linear scaling of the computational effort in the number of particles and a factor independent of system size between TS model and simple charge approach. This shows that the number of steps in the self-consistency loop is independent of system size. In all cases the present work deals with less than merely five steps for convergency are required.

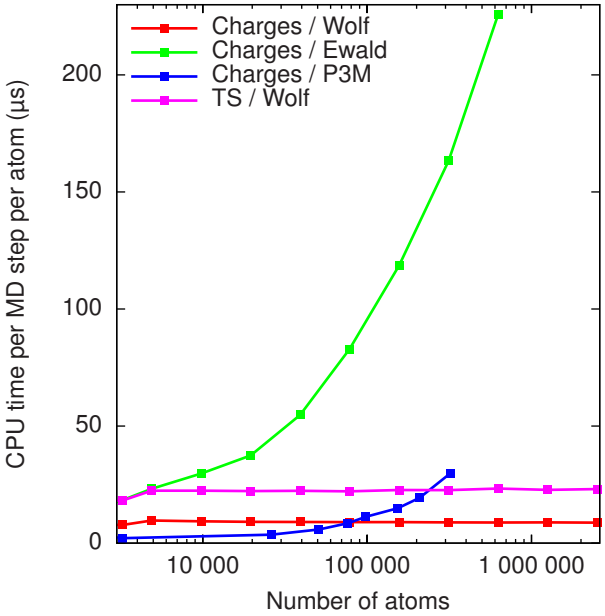

Figure 3.8.: Scaling of computational effort with system size in liquid silica for Wolf summation with and without dipole contributions. The TS model is slower by a constant factor of 2.6. P3M and Ewald for charges are shown again as a reference. The accuracy of each method is chosen to 10^{-3} as in section 3.1.4.

3.3.3. Validation

Before new force fields can be generated as described in chapter 5, the new combination of the non-reparametrized TS silica force field with the Wolf method has to be validated (the origial TS approach used Ewald summation). For this purpose, basic thermodynamic and structural studies are compared for two settings:

1. *TS*: original TS silica force field + Ewald summation method,

2. *New Potential*: non-reparametrized TS silica force field + Wolf summation method.

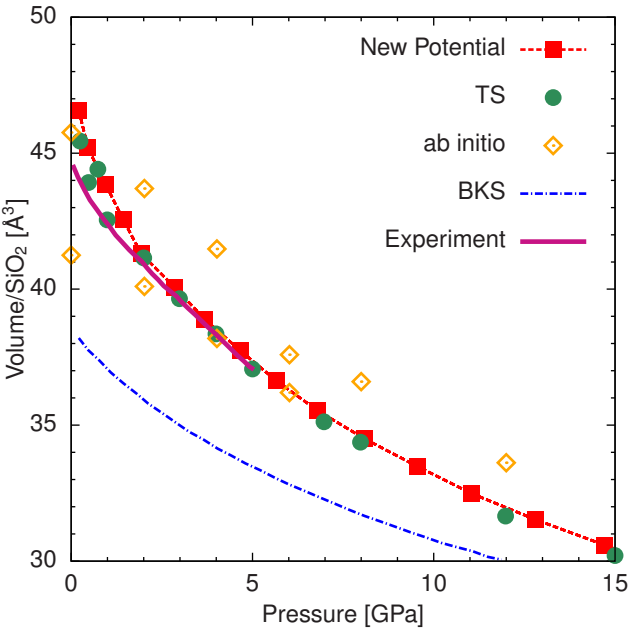

Figure 3.9.: Equation of state of liquid silica at 3100 K for the new potential compared to original TS [88], experiment [21], ab initio simulations [88] and simulations with the non-polarizable BKS potential model [88].

Additionally shown are ab initio results as well as experimental studies for comparison. Also simulations with the well-known BKS potential [89] are included, because many domain experts still use the non-polarizable BKS model although it apparently lacks accuracy in many simulation studies.

First, the equation of state of liquid silica at 3100 K is compared to experiments [21], ab initio results and the original TS potential in figure 3.9. Pressures were obtained as averages along constant-volume MD runs of approximately 10 ps following 10 ps of equilibration and with simulation cells containing 4896 atoms. The good agreement of the original TS potential with the experimental results can be reproduced.

On a microscopic level, the Si–O–Si angle distribution was determined from multiple MD simulation runs at 3100 K and various pressures. The results are shown in figure 3.10 and are in agreement with the original TS

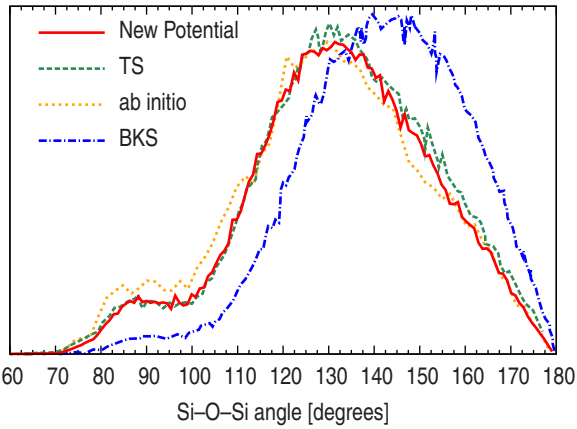

Figure 3.10.: Oxygen centered angle distribution in liquid silica at 3100 K for the new potential compared to original TS, ab initio simulations and the non-polarizable BKS potential model (last three from [88]).

	Experiment [47]	New Potential	TS [88]	BKS [88]
a [Å]	4.916	4.872	4.925	4.941
c [Å]	5.405	5.359	5.386	5.449
ρ $[\frac{\mathrm{g}}{\mathrm{cm}^3}]$	2.646	2.718	2.665	2.598
Si–O–Si	143.7	142.1	144.5	148.1

Table 3.1.: Quartz: Lattice parameters a and c, density ρ and oxygen centered angle.

potential and ab initio results.

The new force field is also probed by simulating the most important low pressure crystal structures quartz, cristobalite and coesite. The relevant equilibrium variables density, Si–O–Si angle and the lattice parameters at 300 K are given in tables 3.1, 3.2 and 3.3. The average relative deviation of the crystal data from the experimental results is $\approx 0.9\%$. Simulations with the original TS potential yield a relative deviation of the parameters that averages at merely $\approx 0.7\%$. Both simulation approaches agree comparatively good with experiment, but a small decrease in precision can be observed when using the new potential.

	Experiment [80]	New Potential	TS [88]	BKS [88]
a [Å]	4.969	5.015	4.936	4.920
c [Å]	6.925	6.999	6.847	6.602
ρ $[\frac{\mathrm{g}}{\mathrm{cm}^3}]$	2.334	2.268	2.412	2.515
Si–O–Si	146.4	147.1	144.0	143.9

Table 3.2.: Cristobalite: Lattice parameters a and c, density ρ and oxygen centered angle.

	Experiment [46]	New Potential	TS [88]	BKS [88]
a [Å]	7.136	7.123	7.165	7.138
b [Å]	7.174	7.161	7.162	7.271
c [Å]	12.369	12.347	12.377	12.493
β	120.34	120.34	120.31	120.76
ρ $[\frac{\mathrm{g}}{\mathrm{cm}^3}]$	2.921	2.940	2.933	2.864
Si–O–Si	143.6	144.2	144.0	150.5

Table 3.3.: Coesite: Lattice parameters a, b and c, monoclinic angle β, density ρ and oxygen centered angle.

In summary, simulations can be accelerated by replacing Ewald with Wolf summation in the non-reparametrized TS force field without significant loss of accuracy. There are, however, small weaknesses of the new force field (e.g. higher average relative deviations from experiment for crystal structure data). Hence, also a new parametrization of the silica force field is meaningful and presented in section 5.1.

Chapter 4.

Visualization

Modern visualization techniques do not only supply pretty pictures of snapshots taken from MD simulations, but also facilitate novel findings by providing a better insight with clever and especially adapted representation of the data. Also for the present study of metal oxides they are taken into account in addition to conventional analytic analyses. A preliminary example of the visualization's effectiveness is given in figure 4.1.

The visualization of the present work is done with the program MegaMol [29], which was developed at the Visualisierungsinstitut in Stuttgart and upgraded during the last two years by Sebastian Grottel and Katrin Scharnowski. They implemented new modules specialized in electrostatics of metal oxides. MegaMol is tailored to the visualization of large, dynamic particle data sets. The following three visualization techniques are available in MegaMol and are applied to analyze data from metal oxide MD simulations.

4.1. Glyph representation

The most basic approach is a simple sphere and arrow glyphs representation. For the present applied force fields containing electrostatic induced dipole moments, each metal ion is depicted by a sphere and each oxygen ion is represented by an arrow showing magnitude and direction of its dipole moment. Thereby, the center of an arrow is pinned to the atomic coordinate. The arrows are color coded to further highlight their orientation. The respective color map is shown in figure 4.2. Details of the used so-called shader-based ray casting technique can be found in [73]. Figure 3.4 (p. 56) is an example for this glyph representation. It provides a familiar visualization of the dipole moments, but this is only useful when looking at a rather small area of a data set. The left side of figure 4.3 shows a

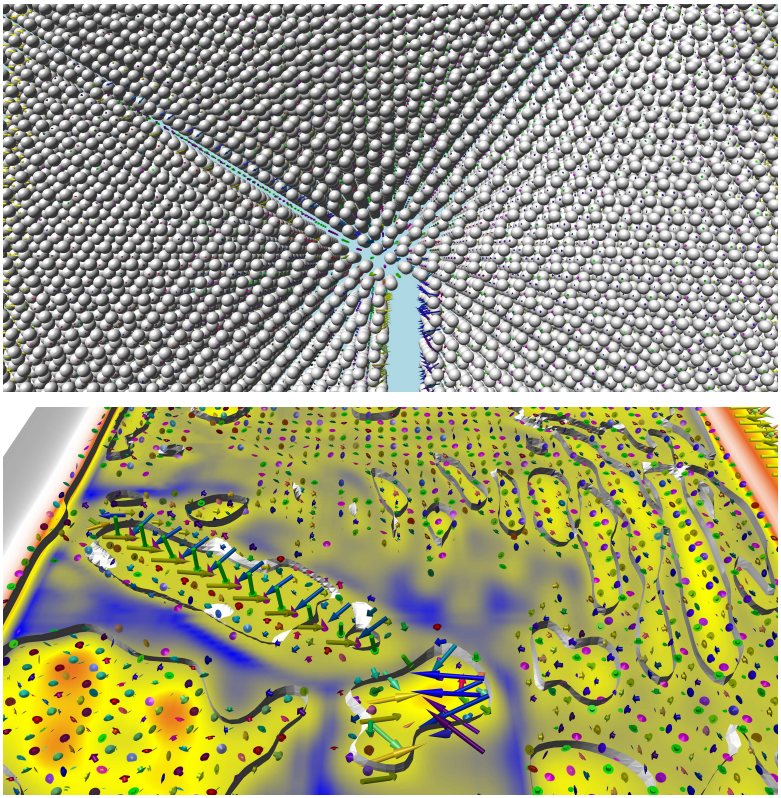

Figure 4.1.: Preliminary example: crack propagating in crystalline α-alumina (see chapter 7), both pictures are prepared with MegaMol [29], the lower by Sebastian Grottel [28]. Above: Simple spheres depict aluminum atoms, each oxygen atom is represented by an arrow showing magnitude and direction of its dipole moment. The crack can be clearly seen, but the view on the dipole moments is mostly covered by the spheres. Below: Combination of the arrow glyph representation with the methods of fractional anisotropy (introduced in section 4.2) and iso surfaces (introduced in section 4.2.1) reveals previously hidden discoveries: Regions of correlated dipole orientation are accentuated and a wavelike propagation in the field of dipole moments coming from the crack tip can be observed.

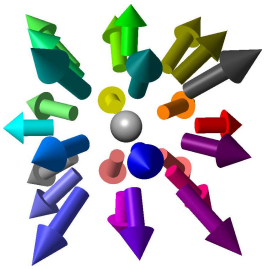

Figure 4.2.: The color coding of the arrow glyphs further highlights the orientation, from [28].

similar but slightly bigger MD data set. Already in this case, where the simulation box contains merely 3264 oxygen atoms, occlusion effects and the representation appears cluttered. If one is nevertheless interested in seeing single dipole moments, a further approach is filtering out unimportant arrows. The definition of *unimportant* of course must then be given by the scientific context of the question at hand. Examples can be seen in figures 8.9 (p. 137) and 8.10 (p. 138), where the filter threshold is a certain magnitude of the moments to remove too small ones for a clear view.

4.2. Fractional anisotropy (FA)

During the work of this thesis, collective behavior of dipole moments appeared in several metal oxide systems under special conditions (e.g. shown in section 7.2 or chapter 8). With the objective of a closer inspection of these collective phenomena, the method of fractional anisotropy (FA) was implemented in MegaMol by Grottel [28] and applied to the study of metal oxide systems. Originally, FA is a scalar value computed from the effective diffusion tensor in diffusion tensor imaging, which measures the part of the tensor that can be ascribed to anisotropic diffusion [4]. Transferring this approach to the application of collective dipole behavior, a value can be obtained that is an indicator for how correlated the orientation of the oxygen dipoles is within a restricted area of the data set.

The FA scalar field is constructed as follows: A volume grid is defined based on the MD data set size by computing the resolution of the grid

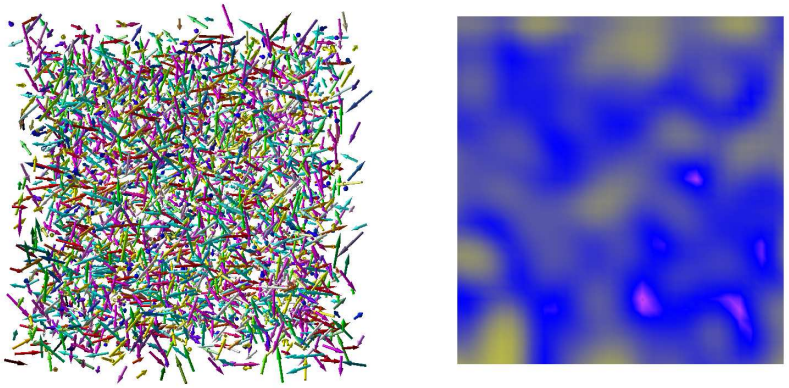

Figure 4.3.: Left: Simple arrow representation of liquid silica (4896 atoms at 3100 K, thereof 3264 oxygen ions depicted by arrows, respective force field introduced in section 5.1); occlusion effects occur and the representation appears cluttered. A statement concerning collective dipole behavior is not possible. Right: The scalar field of FA clearly uncovers small, unstable polarization regions (yellow) that are in contrast to the dominant region (blue), where dipoles are isotropically distributed.

from the average distance between atoms, thus roughly mapping one atom onto one voxel (volumetric pixel, a volume element, representing a value on a grid in three dimensional space). Based on the distance $d_{ij} = |\mathbf{r}_i - \mathbf{v}_j|$ between the position $\mathbf{r}_i$ of oxygen atom i and the position $\mathbf{v}_j$ of the voxel j, a weight w_{ij} for the contribution of the particle to that voxel is calculated as

$$w_{ij} = \begin{cases} 2\left(\frac{d_{ij}}{d_c}\right)^3 - 3\left(\frac{d_{ij}}{d_c}\right)^2 + 1 & \text{if} \quad d_{ij} \leq d_c \\ 0 & \text{if} \quad d_{ij} > d_c \end{cases}, \tag{4.1}$$

where d_c is the finite support radius of the function. It can be taken as a cut-off radius for the calculation of the FA field. In order to capture the data of the significant neighborhood, d_c is always put on a level with the Wolf cut-off radius r_c in the MD force calculation. For each voxel j, the

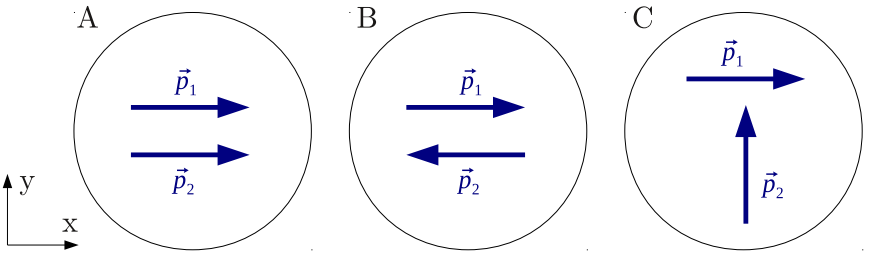

Figure 4.4.: Sketch of two identically (A), oppositely (B) and orthogonally (C) directed dipole moments. Vectors are distinguished with arrows inside of the graph.

FA value F_j of its particle neighborhood is computed as:

$$F_j = \sqrt{\frac{(\lambda_{j1} - \lambda_{j2})^2 + (\lambda_{j2} - \lambda_{j3})^2 + (\lambda_{j3} - \lambda_{j1})^2}{2(\lambda_{j1}^2 + \lambda_{j2}^2 + \lambda_{j3}^2)}}, \tag{4.2}$$

with the eigenvalues λ_{j1}, λ_{j2}, and λ_{j3} of the matrix $\underline{\underline{P}}^j$ formed by the dipole moments $\mathbf{p}_i$ of atoms i:

$$\underline{\underline{P}}^j = \frac{1}{N_w} \sum_{i=1}^{N_w} w_{ij} \mathbf{p}_i \otimes \mathbf{p}_i. \tag{4.3}$$

N_w is the number of atoms i with $w_{ij} > 0$. Note that the dipoles are not normalized before entering equation (4.3). This is important to identify small local correlations as normalization yields a certain smoothing and would hide local effects on small scales. Not till the whole scalar field is calculated, the FA values are normalized to be between zero and one.

Let two dipoles be given (with both weights for the considered voxel being equal to one) to illustrate the FA mechanism. Figure 4.4 shows a sketch of three situations:

A) The dipoles have the same direction $\mathbf{p}_1 = \mathbf{p}_2 = (1;0)^T$; then, the eigenvalues of $\underline{\underline{P}}$ are $\lambda_1 = 0$ and $\lambda_2 = 1$ and the FA value becomes $F_A = \frac{1}{\sqrt{2}}$.

B) The dipoles have opposite directions $\mathbf{p}_1 = (1;0)^T$ and $\mathbf{p}_2 = (-1;0)^T$;

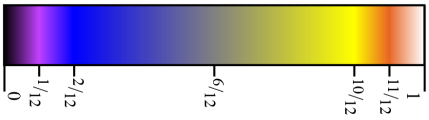

Figure 4.5.: The color map used for the normalized values of FA. The purple band at 1/12 and the red band at 11/12 are used to identify areas of very low and very high values. From [28].

then, the eigenvalues are identical to case A and, hence, the FA value also becomes $F_B = \frac{1}{\sqrt{2}}$.

C) The dipole vectors are orthogonal, $\mathbf{p}_1 = (1;0)^T$ and $\mathbf{p}_2 = (0;1)^T$; then, the eigenvalues of $\underline{\underline{P}}$ are $\lambda_1 = \lambda_2 = \frac{1}{2}$ and the FA value becomes zero.

This basic evaluation illustrates, that the FA approach is able to detect both ferro- and antiferroelectric domains and to separate them from rather uncorrelated regions. Simply adding up all vectors inside the cut-off sphere would only detect ferroelectric states, because two antiferroelectric aligned moments would cancel each other out.

For the visualization of the FA field, a color map as depicted in figure 4.5 is chosen. It is based on cool-warm shading, but specifically highlights very high and very low values. A first example is given in figure 4.3, where the arrow glyph representation yields mainly a cluttered view on the liquid silica sample. The FA field, however, shows the existence of small, unstable polarization regions.

4.2.1. FA iso surfaces

The display can be further enhanced by visually circumscribing the regions where collective orientations emerge using iso surfaces of the FA scalar field. This add-on is especially useful when watching an animation of the whole trajectory as it enables a view on regions moving, disseminating or shrinking over time. The iso value is a selectable parameter between zero and one and has to be adjusted for each individual problem to gain the best depiction. Iso surfaces calculated in the field of FA can also be shown in the glyph-representation. An example with an iso value of 0.68 is given in figure 4.1.

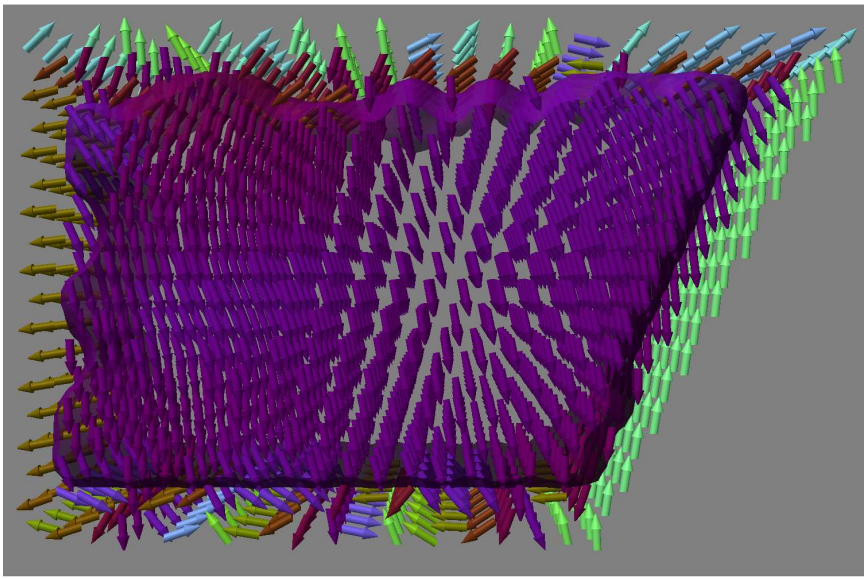

Figure 4.6.: DS iso surface circumscribing a domain of similarly orientated dipole moments (periclase sample, see section 8.3). Visualization support from [79].

4.2.2. Shading

Finally, further information can be depicted on the glyphs with a shading mechanics. In doing so, the degree of correlation determined by the FA field is projected onto the arrows. The mapping allows for easy identification of uncorrelated regions (dark areas, low FA), while in areas of high correlation (high FA) the colorization of the glyphs additionally provides a direct indication of how the dipoles are oriented. The shading approach can be seen for example in figure 7.2.

4.3. Directional similarity (DS)

As mentioned in section 4.2, the fractional anisotropy is able to resolve correlations on small scales, because the dipole moments are not normalized

before the FA value is obtained. This implicates a drawback in the case of regions with similar orientated moments which, however, vary strong in their magnitudes. Then the FA is not able to detect such a region as one single domain, because the FA distinguishes short dipoles from longer ones even if their direction is equal.

Another visualization tool to highlight domains with dipoles featuring similar orientations but different magnitudes is the approach of directional similarity (DS). It was implemented in MegaMol by Scharnowski [79]. The DS firstly normalizes the dipole moments. Then, they are mapped onto a grid, which is only required for saving computing time in the following steps. The DS field is simply obtained by computing the vorticity of the dipole field.

The DS approach identifies dipole regions with similar orientations independent of their magnitudes. However, it is not able to detect antiferroelectric domains as in the case of the FA approach.

4.3.1. DS iso surfaces

As in the FA case, the display can be further enhanced by visually circumscribing the regions where similar directions emerge using iso surfaces of the DS scalar field. The criterion for placing DS iso surfaces is the vorticity of the dipole field. For a clear view, a gaussian smoothing is applied. Otherwise, the DS iso surfaces would look somewhat angular. Figure 4.6 shows an example of a domain with similar orientations but different magnitudes of dipole moments which is clearly circumscribed by the DS iso surface.

Chapter 5.

Force field generation

5.1. Silica

The method of combining the TS polarizable force field model and the direct Wolf summation is first applied to silica (SiO_2). The most prominent case, where silica is found in technological applications, is microelectronics industry. For manufacturing the many transistors forming a microchip, commonly a silicon wafer is employed. With the process of thermal oxidation, an amorphous silica film is built on the silicon substrate. At the time when copper elements are embedded into the system for conducting current, silica acts as an insulator. Although there are superior materials called high-k-dielectrica on the way, many present-day microchips still deal with silica. Due to its nontoxic behavior, silica additives are also used in many everyday life products. Another field of application is geophysics, because the crystalline quartz-phase of silica is one of the two most frequently occuring minerals inside the earth crust. In all cases, it is very valuable to know both bulk behavior and microstructural properties of silica under various and partly extreme thermodynamic properties.

Due to the described technological and geological significance, silica has been thoroughly investigated experimentally [21, 60], by using ab initio calculations [38, 64, 94] and in simulations with empirical interaction potentials [35, 39, 89, 90]. Also the original TS model, that uses classical Ewald summation, was first applied to liquid silica. Hence, silica is an ideal test case for the new potential generation. In the following, the force field generation is shown as well as its validation and application to several basic studies.

5.1.1. Force field parametrization

At first, a reference structure database was prepared. Five MD trajectories were generated with the non-reparametrized silica TS force field and Wolf summation (this non-reparametrized version was judged in section 3.3 as highly accurate). These constant-temperature runs were performed at five different temperatures from 2000 to 4000 Kelvin in 500 K steps. In addition, the volume was slightly lowered to prepare different pressure conditions. Then, several snapshots were taken following 10 ps of equilibration. In this way, 47 liquid reference structures were prepared with on average 109 atoms, altogether 5123 atoms. The reference structures show a pressure spectrum from zero up to 15 GPa. They then were applied as input configurations for VASP, where PAW pseudopotentials and a generalized gradient approximation (GGA) of the exchange-correlation functional were used. For the silicon (oxygen) pseudopotential, the default settings $E_{\mathrm{cut}}^{\mathrm{Si}} = 245$ eV ($E_{\mathrm{cut}}^{\mathrm{O}} = 400$ eV) in the PAW are selected. With the LDA exchange-correlation functional, the well-known underestimation of the volume yielded clear deviations from experimental data. The approach with GGA and the same reference structures, however, was able to reproduce the volume in MD simulations. Replacing the pseudopotential or increasing its energy cut-offs had no noticeable influence on the results.

Then, the reference database was committed to potfit. The weights in potfit were chosen to $w_e = 0.1$ and $w_s = 0.5$, which is consistent with comparable optimization approaches [39, 88]. The resulting parameters, however, remained rather unaffected by modification of the weights. By contrast, the splitting parameter κ had to be optimized. Setting $\kappa = 0.02$ Å^{-1}, a cut-off radius of only 8 Å was found to be sufficient, which is small compared to other [11, 39] long-range potential approaches and results in an additional speedup in simulations. For comparison only, the procedure was repeated with a cut-off radius of 10 Å. The obtained results were quite similar. As the computational effort scales with r_c^3, simulations with a cut-off radius of 8 Å are about two times faster than the same settings with a cut-off radius of 10 Å . It has to be mentioned that $\kappa = 0.02$ Å^{-1} describes a relatively weak damping. This identifies the good native screening ability of liquid silica. The final set of parameters is shown in table 5.1. The rms errors are $\Delta F_e = 0.1922$, $\Delta F_s = 0.0341$ and $\Delta F_f = 1.6211$.

q_{Si}	q_{O}	α_{O}	$b_{\mathrm{Si-O}}$	$c_{\mathrm{Si-O}}$
1.860032	−0.930016	0.020689	4.434517	−31.525678
$D_{\mathrm{Si-Si}}$		$D_{\mathrm{Si-O}}$		$D_{\mathrm{O-O}}$
0.000004		0.100108		0.028596
$\gamma_{\mathrm{Si-Si}}$		$\gamma_{\mathrm{Si-O}}$		$\gamma_{\mathrm{O-O}}$
19.841872		11.598884		8.808762
$\rho_{\mathrm{Si-Si}}$		$\rho_{\mathrm{Si-O}}$		$\rho_{\mathrm{O-O}}$
5.400713		2.066695		3.742815

Table 5.1.: Force field parameters for silica as introduced in equations (3.13)–(3.15), given in IMD units set eV, Å and amu (hence charges are multiples of the elementary charge).

For the new silica force field, the dipole structure factor and the resulting reciprocal-space contribution of the total energy was evaluated. For the selected damping of $\kappa = 0.02\,\mathrm{Å}^{-1}$ the result is

$$\frac{1}{N} E_{\mathbf{k}}^{\mathrm{pp}} = 0.09\,\mu\mathrm{e}V, \tag{5.1}$$

whereas the real-space contribution of the total energy per atom is

$$\frac{1}{N} E_{\mathbf{r}}^{\mathrm{tot}} = 7.20\,\mathrm{e}V. \tag{5.2}$$

Hence the reciprocal-space term is indeed insignificant and the model of neglecting reciprocal-space contributions is accurate.

5.1.2. Validation

The new potential was validated by determining thermodynamic, microstructural and vibrational properties of silica. The goal was to cover different temperature and pressure scenarios in order to show the transferability of the new potential. The following simulations were all performed with the same initial configuration consisting of 4896 atoms (1632 Si and 3264 O). Due to the Wolf summation, it would of course be possible to simulate much bigger systems in reasonable time duration. However, this is not required for condensed matter systems because of the periodic boundary conditions applied in MD simulations.

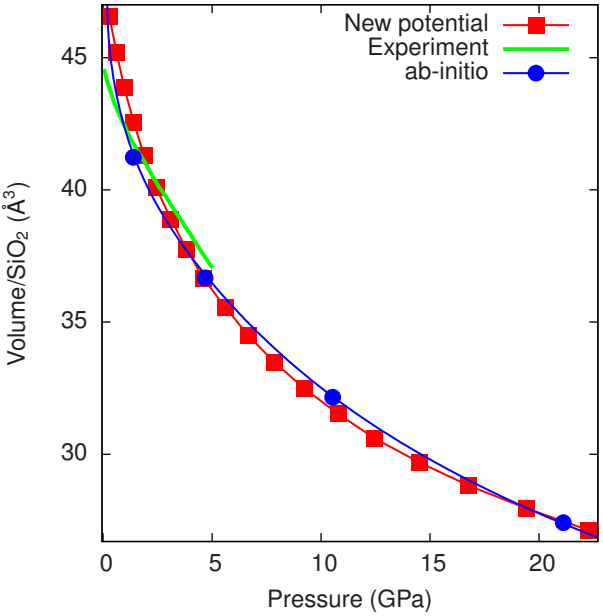

Figure 5.1.: Equation of state of liquid silica at 3100 K for the new potential compared with experiment [21] and ab initio calculations [38].

In figure 5.1, the equation of state of liquid silica at 3100 K calculated with the new potential is shown. Pressures were obtained as averages along constant-volume MD runs of 10 ps following 10 ps of equilibration. For comparison, experimental data [21] and first principles results using VASP [38] are illustrated. The equation of state calculated with the new potential coincides with ab initio and experimental results.

The radial distribution functions for Si–Si, Si–O and O–O at 3000 K with volume/SiO_2 $V_{SiO_2} = 45.80$ Å^3 were evaluated for 100 snapshots taken out of an 100 ps MD run. The averaged curves are given in figure 5.2. Results calculated with the new potential are in accurate agreement with ab initio data [38]. The Si–Si and O–O curves are slightly shifted to larger distances.

The Si–O–Si angle distribution was determined from 300 MD runs at 2370 K and zero pressure. The averaged result is compared with an ab initio MD study [94] and is depicted in figure 5.3. As discussed in Ref.

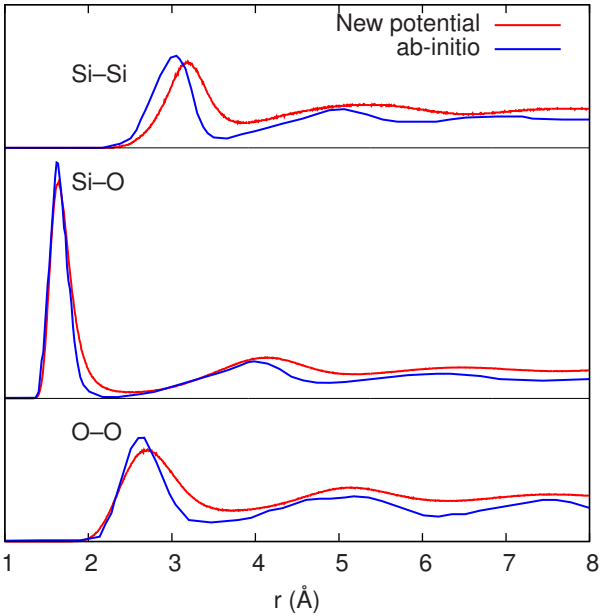

Figure 5.2.: Radial distribution functions for Si–Si, Si–O and O–O at 3000 K compared with ab initio calculations [38].

[94], the ab initio MD tend to shift the angle distribution of liquid silica to slightly smaller angles with respect to the distribution generated by empirical MD simulations.

The new force field was also applied to simulations of amorphous silica, although its parameters were only optimized with liquid reference structures between 2000 and 4000 K. For this purpose, the liquid initial structure was cooled down to 300 K at an annealing rate of 0.01 K/fs, which is recommended by Vollmayr et al. [93] and also used in Ref. [39]. Using different annealing rates, however, had no significant impact on the results. The VDOS $G_{Si}(E)$ ($G_O(E)$) for silicon (oxygen) was obtained from a 100 ps MD trajectory with nMoldyn [75]. Figure 5.4 shows the partial and generalized VDOS compared with an ab initio study from Ref. [64]. The curves were adjusted in order to display the three main bands of each curve at similar frequencies. For silica, the optimal value for the frequency scaling

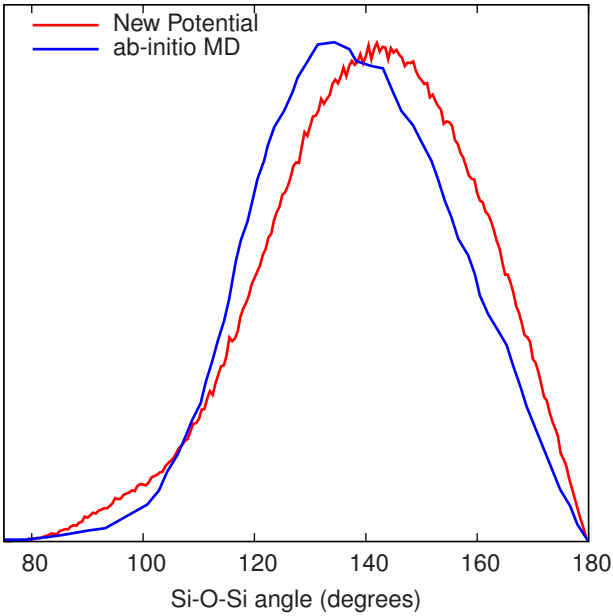

Figure 5.3.: Oxygen centered angle distribution in liquid silica at 2370 K for the new potential compared with an ab initio MD study [94].

is $\gamma = 0.3$. The new force field reproduces the key features of the partial VDOS. There are, however, several smaller deviations from ab initio results: The partial VDOS for silicon overestimates the low-energy band as the main-peak is shifted by around 12 meV to lower energies. The partial VDOS for ogyxen does not reproduce the band between 35–55 meV and the two smaller peaks at around 77 meV and 108 meV. These characteristics are also reflected in the generalized VDOS. The relatively large scaling of the MD curves might also be a weakness of the new potential. In summary, the new potential is able to qualitatively reflect the lattice dynamics, although it was not optimized for amorphous states at 300 K, but there are limits to its accuracy.

As a final test, the force field was used for MD studies of α-quartz, one of the most important low-pressure crystal structures of SiO_2. This is a very hard test for the transferability of the potential, considering liquid

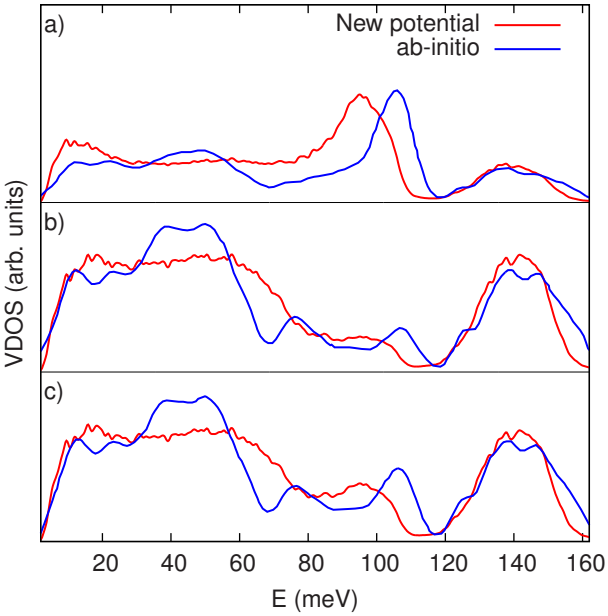

Figure 5.4.: VDOS of amorphous silica at 300 K calculated with the new potential compared with an ab initio MD study [64]. a) partial VDOS for silicon atoms, b) partial VDOS for oxygen atoms, c) generalized VDOS.

structures between 2000 and 4000 K were used as reference data. In table 5.2, the lattice parameters, Si–O bond length, and the Si–O–Si angle are compared to analytical values [24, 25]. The force field overestimates the equilibrium volume; the lattice parameters are too large by on average 2.8%. In an MD simulation at 300 K over 10 ns, the force field stabilized the alpha-quartz structure. This shows that the new potential does yield reasonable results even under conditions it was not optimized for.

In summary, the new force field approach yields highly accurate results for liquid silica. The new potential can be applied to lots of silica investigations, which could not yet be adequately investigated with MD simulations due to large system sizes or boundary condition restrictions. Probing solid phases, which were not included in the reference database during the force

	a (Å)	c (Å)	Si–O (Å)	Si–O–Si (°)
New potential	5.15	5.50	1.65	148.5
Theory	4.97 [25]	5.39 [25]	1.61 [24]	145 [24]

Table 5.2.: Lattice parameters, Si–O bond length and Si–O–Si angle of α-quartz compared with theoretical studies.

field optimization, yields suitable results on a qualitatively level. Quantitative analysis, however, should be done carefully as expected.

5.2. Magnesia

The second application of the new force field approach is magnesia (MgO), another very important metal oxide. Not only is it one of the stoichiometricely simpler oxides (making it a frequently studied test system), it is also both ubiquitous and of technological importance. Beside its every-day usage - encoded as E 530 in food industry or given to gymnasts for antislip hands - magnesia is frequently applied in industry due to its high melting point. Furnaces and other components which have to be heat resistant are commonly coated with magnesia. Hence, there have been many experimental [5, 30, 65, 83] and theoretical [1, 37, 63, 77, 87] studies. By generating a force field for magnesia, the combined use of the TS model and Wolf summation for the first time was applied beyond silica.

5.2.1. Force field parametrization

To generate the reference structure database for liquid magnesia, snapshots from an MD trajectory with an ad-hoc potential were used. In this way, 80 liquid reference structures with on average 242 atoms, in total 19 360 atoms, were prepared. The reference forces, stresses and energies were computed with VASP using PAW pseudopotentials and in the GGA approximation as approved in the silica case. The energy cut-off for the magnesium pseudopotential is given by $E_{\text{cut}}^{\text{Mg}} = 210$ eV. From these, an intermediate TS potential was obtained, which then was again used to generate a new MD trajectory and then a new set of reference structures. This procedure was iterated until there was no further significant change in the potential parameters. The pressure spectrum of the final reference structure database

q_{Mg}	q_{O}	α_{O}	$b_{\mathrm{Mg-O}}$	$c_{\mathrm{Mg-O}}$
1.230958	−1.230958	0.045542	3.437254	−24.256585
$D_{\mathrm{Mg-Mg}}$		$D_{\mathrm{Mg-O}}$		$D_{\mathrm{O-O}}$
0.000003		0.100093		0.000003
$\gamma_{\mathrm{Mg-Mg}}$		$\gamma_{\mathrm{Mg-O}}$		$\gamma_{\mathrm{O-O}}$
18.736878		10.340058		18.696021
$\rho_{\mathrm{Mg-Mg}}$		$\rho_{\mathrm{Mg-O}}$		$\rho_{\mathrm{O-O}}$
6.161436		2.458717		6.630618

Table 5.3.: Force field parameters for magnesia as introduced in equations (3.13)–(3.15), given in IMD units set eV, Å and amu.

is between 0 and 15 GPa, while the temperature varies between 2000 and 5000 K to account for the higher melting point of magnesia. The weights in potfit again were set to $w_e = 0.1$ and $w_s = 0.5$. A cutoff radius of 8 Å was sufficient when choosing $\kappa = 0.1$ Å^{-1}. The final set of parameters is shown in table 5.3. The rms errors are $\Delta F_e = 0.1170$, $\Delta F_s = 0.0228$ and $\Delta F_f = 0.5295$.

The following values for the Wolf dipole error estimation were obtained by averaging over a simulation time of 200 ps. The reciprocal-space term is again really insignificant. For $\kappa = 0.1\,$Å^{-1}, the result is

$$\frac{1}{N} E_{\mathbf{k}}^{\mathrm{pp}} = 0.15\,\mu\mathrm{e}V, \tag{5.3}$$

whereas the real-space contribution of the total energy per atom is

$$\frac{1}{N} E_{\mathbf{r}}^{\mathrm{tot}} = 6.30\,\mathrm{e}V. \tag{5.4}$$

5.2.2. Validation

The new potential was validated by determining thermodynamic and microstructural properties of liquid magnesia. The transferability of the new potential beyond the optimized temperature range was also investigated by modelling the most important crystal structure periclase (NaCl-type). The following simulations were all performed with the same initial configuration consisting of 5832 atoms (2916 Mg and 2916 O).

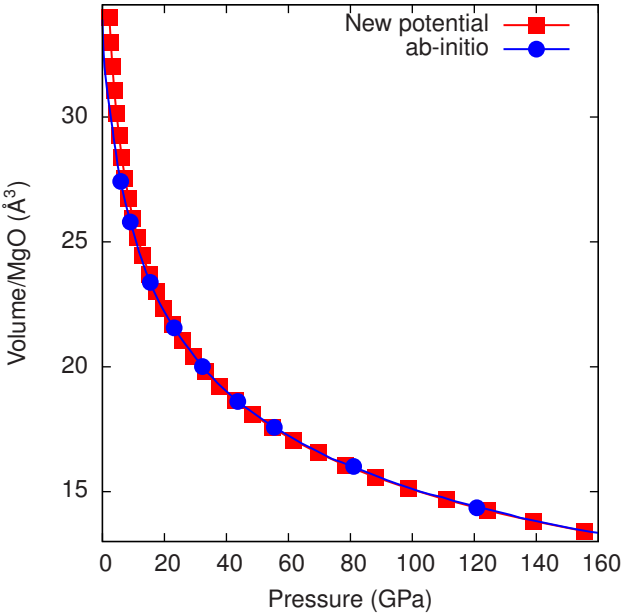

Figure 5.5.: Equation of state of liquid magnesia at 5000 K for the new potential compared with ab initio calculations [37].

The equation of state, obtained as in silica, is shown in figure 5.5. Due to the high melting point of magnesia, a temperature of 5000 K was chosen. The result is compared with a first-principles study using VASP [37]. Although the new potential was optimized with a reference database having a pressure spectrum from zero to 15 GPa, it is able to reproduce the ab initio results quite accurate up to 160 GPa.

In figure 5.6 the radial distribution function for Mg–Mg (which is very similar to the O–O function) and Mg–O is depicted at 3000 K with volume/MgO $V_{\mathrm{MgO}} = 27.76$ Å^3. The results coincide precisely with ab initio data [37].

The Mg–O–Mg angle distribution was determined from several MD runs at $V_{\mathrm{MgO}} = 33.99$ Å^3 and three different temperatures 3000 K, 4000 K and 5000 K. The curves look similar (see figure 5.7), they show a maximum at 100 degrees. So the interatomic angles in the magnesia melt are about 10

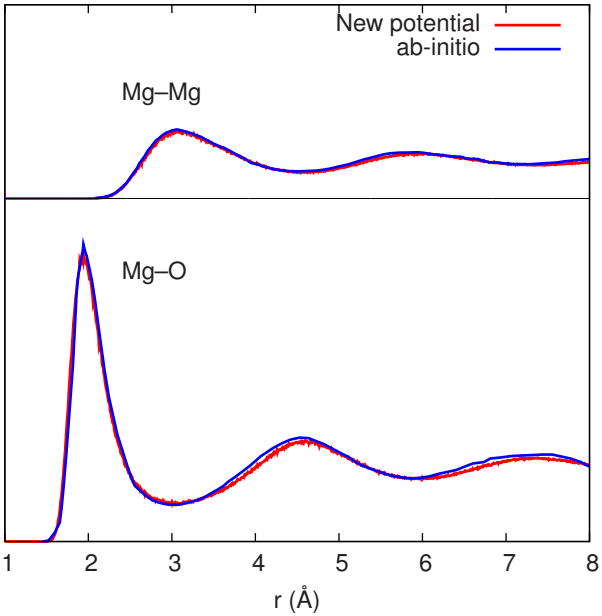

Figure 5.6.: Radial distribution functions for Mg–Mg (which is very similar to O–O case) and Mg–O at 3000 K, compared with ab initio calculations [37].

degrees greater than in periclase. Both distribution studies follow from an averaging in the same way as for silica.

Finally, the new force field was applied to simulations of periclase at 300 K, although its parameters were only optimized with liquid reference structures between 2000 and 5000 K. The new force field is able to stabilize the cubic periclase structure with high accuracy. The lattice constant is in very good agreement with recent ab initio and experimental studies, as presented in table 5.4.

In the same way as for silica, the generalized VDOS of periclase was obtained. Figure 5.8 shows a comparison with ab initio calculations [22] and an experimental [6] study. A frequency scaling of only $\gamma = 0.03$ was applied. The new potential is able to qualitatively reproduce the key features, but there a two weak points: Firstly, the main peak at around 53 meV is shifted

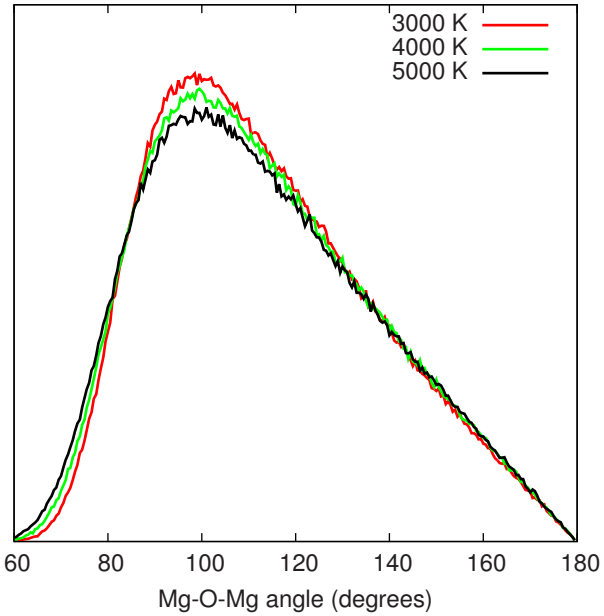

Figure 5.7.: Oxygen centered angle distribution in liquid magnesia for the new potential for 3000 K, 4000 K and 5000 K.

to lower frequencies by around 10 meV. Secondly, the peak at 36 meV – originating from the partial VDOS for oxygen – is only weakly reproduced. In summary, the new force can give only qualitative results concerning lattice dynamics in this temperature range, for which it was not optimized.

To sum up the validation, the new magnesia force field yields generally accurate results. As in the case of silica the new potential can be applied to lots of magnesia investigations, which could not yet be adequately investigated with MD simulations due to large system sizes or boundary condition restrictions. Also the cubic periclase structure can be modelled accurately, although the force field parameters were only optimized with liquid reference structures. The magnesia study additionally shows, that a crude starting potential suffices to determine high-quality potentials, which makes the new force field approach applicable for even more systems of interest.

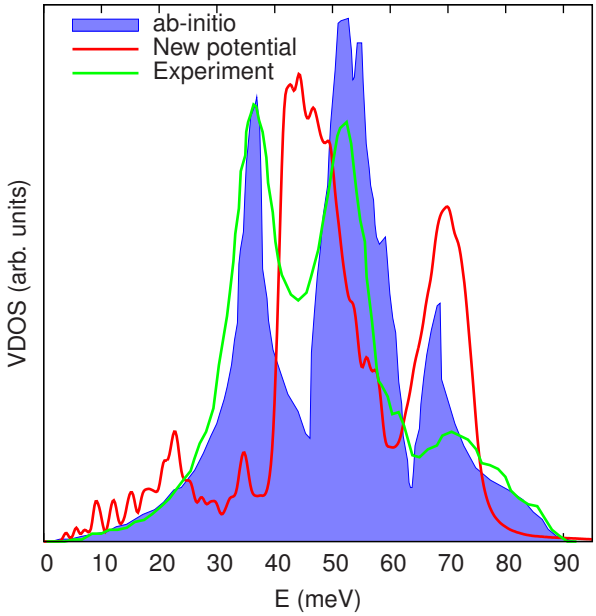

Figure 5.8.: Generalized VDOS of periclase at 300 K calculated with the new potential compared with ab initio calculations [22] and an experimental study [6].

5.3. α-Alumina

α-alumina is the first crystalline system, where the new force field approach is applied to. This is more difficult, because the Wolf method is known to be more accurate in liquid or at least amorphous systems. As discussed in section 3.1.3, a basic condition for the applicability of the Wolf summation is a natural screening ability of the system of interest. The ionic neighborhood in a liquid system is basically more isotropic than in an ordered crystal, which may result in a higher cut-off radius needed in the following for getting accurate results.

For the purpose of applying the new force field generation to a crystalline system, alumina was chosen, because it is the most commonly used ceramic in technological applications. Due to its insulating properties, it

New Potential	4.214
Exp. [83]	4.212
Exp. [5]	4.211
ab initio (GGA) [1]	4.234
ab initio (LDA) [63]	4.240

Table 5.4.: Lattice constant a [Å] of periclase determined with the new potential compared to ab initio and experimental studies.

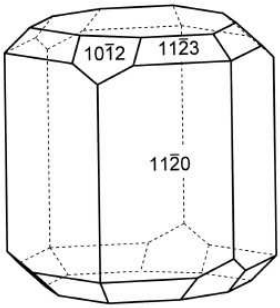

© 2007 Walter de Gruyter, Riedel/Janiak: Anorganische Chemie.

Figure 5.9.: Sketch of the hexagonal scalenohedral crystal structure of α-alumina. From [14].

is frequently adopted in microelectronic devices, i.e., field effect transistors or integrated circuits. Another important field of application is the coating of metallic components. Alumina covering aluminum is known to prevent further oxidation of the metal. Since alumina is characterized by a high melting point and also a high degree of hardness, applications at high temperatures and high mechanical demands are possible. Together with diamond, α-alumina belongs to the two hardest minerals in the world (9 Mohs compared to 10 Mohs for diamond). Mechanical properties such as tensile strengths and fracture processes are of high importance in most application areas. Hence, the main task of the below presented alumina

force field is the simulation of propagating cracks.

Due to this technological significance, alumina was frequently investigated experimentally [18, 50, 59] and by ab initio methods [17, 58, 99, 100]. First-principles methods are well established for calculating the work of separation or the surface energy. However, the investigation of dynamic processes such as crack propagation requires systems with significantly more atoms and larger timescales than ab initio based methods nowadays can deal with. Hence, it was an important and new challenge to develop a suitable polarizable interaction force field for MD simulations.

α-alumina has a hexagonal scalenohedral crystal structure, which corresponds to point group D_{3d}. A structure sketch is shown in figure 5.9. In hexagonal and rhombohedral lattice systems, the Bravais-Miller index (BMI) which has four numbers ($hkil$) can be applied. Here, h,k and l are identical to the basic Miller index, and $i = -(h+k)$ is a redundant number. The BMI is sometimes more meaningful than the Miller index, because it makes crystal symmetries apparent by permutation. In figure 5.9, three crystallographic planes are exemplarily characterized by its BMI. A crack is geometrically always characterized by the crystallographic plane inside of which it is arranged, and the direction in which it propagates.

5.3.1. Force field parametrization

At first, a set of 67 α-alumina crystal structures with 360 atoms, in total 24 120 atoms, was prepared [32]. This reference database is composed of three kinds of structures:

1. crystals strained up to 20% in [0001], [$\bar{2}$110] and [0$\bar{1}$10] directions at zero Kelvin,

2. structures with free (0001), ($\bar{2}$110) and (0$\bar{1}$10) surfaces at zero Kelvin,

3. equilibrated snapshots taken out of a VASP ab initio MD trajectory (see section 2.2.2), where an ideal crystal is heated from zero Kelvin up to 2000 Kelvin.

The alumina force field generation is focussed on crystalline solids with well-defined structure. Hence, no initial ad-hoc potential is required to generate a reference database. This is only necessary for nonperiodic condensed structures as in the cases of liquid silica (section 5.1) and liquid magnesia

q_{Al}	q_{O}	α_{O}	$b_{\mathrm{Al-O}}$	$c_{\mathrm{Al-O}}$
1.122608	-0.748406	0.026576	18.984286	-5.571329
$D_{\mathrm{Al-Al}}$		$D_{\mathrm{Al-O}}$		$D_{\mathrm{O-O}}$
0.000890		1.000058		0.005307
$\gamma_{\mathrm{Al-Al}}$		$\gamma_{\mathrm{Al-O}}$		$\gamma_{\mathrm{O-O}}$
12.737442		8.077778		12.081851
$\rho_{\mathrm{Al-Al}}$		$\rho_{\mathrm{Al-O}}$		$\rho_{\mathrm{O-O}}$
5.405175		1.851806		3.994815

Table 5.5.: Force field parameters for alumina as introduced in equations (3.13)–(3.15), given in IMD units set eV, Å and amu (hence charges are multiples of the elementary charge).

(section 5.2). The 67 structures were again applied as input configurations for VASP and by use of PAW pseudopotentials (energy cut-off for aluminum $E_{\mathrm{cut}}^{\mathrm{Al}} = 396$ eV) in the GGA approximation as approved in the silica and magnesia case.

The weights in potfit were chosen to $w_e = 0.03$ and $w_s = 0.28$. Setting $\kappa = 0.1$ Å^{-1}, a cutoff radius of 10 Å was found to be sufficient. The final set of parameters is shown in table 5.5. The rms errors are $\Delta F_e = 0.0492$, $\Delta F_s = 0.0273$ and $\Delta F_f = 0.3507$.

5.3.2. Validation

Initially, basic properties of crystalline alumina such as lattice constants [32], cohesive energies [32] and vibrational properties were determined. Additionally and relevant for fracture studies, the validation simulations focused on surface relaxations, surface energies and stresses of strained configurations.

Lattice constants and cohesive energies are obtained by pressure relaxation: Besides energy minimization, the pressure tensor of the sample is calculated at each step, and the size of the simulation box is changed by a small amount in order to lower that pressure. After inserting surfaces or interfaces into the relaxed sample, a further relaxation is performed which reveals surface or interface energies. As can be seen from table 5.6, lattice constants and cohesive energy of crystalline α-alumina obtained with the new potential agree well with ab initio calculations by Hocker [32] and

	a (Å)	c (Å)	E_{coh} (eV)
New potential [32]	4.79	12.97	31.85
Ab initio (Hocker [32])	4.78	13.05	32.31
Lit. (experiment)	4.76 [92]	13.00 [92]	31.8 [95]
Lit. (ab initio)			33.0 [82]
	$E_{(0001)}$ (J/m^2)	$E_{(11\bar{2}0)}$ (J/m^2)	$E_{(10\bar{1}0)}$ (J/m^2)
New potential	1.59	1.65	1.89
Ab initio (Hocker [32])	1.55	1.83	1.98
Lit. (ab initio)	1.85 [85]	2.44 [85]	2.39 [85]
	2.03 [52]	2.23 [52]	2.50 [52]
	1.76 [55]		
	1.54 [69]		

Table 5.6.: Lattice constants a and c, cohesive and surface energies obtained with the new potential compared to ab initio results and literature data. The ab initio data was obtained by Hocker [32] with VASP.

previous studies.

The partial VDOS for aluminum and oxygen ($G_{Al}(E)$ and $G_O(E)$) were obtained in the same way as for silica and magnesia. However, no significant frequency scaling ($\gamma = 0.004$) was necessary, which is a strong indicator for the efficiency of the force field. Figure 5.10 shows the partial and generalized VDOS. The key features of the curves obtained with the new potential and an ab initio study from Ref. [49] coincide. For the partial VDOS of aluminum, both studies show a broad band between 41 and 83 meV. The ab initio results show less states in the low-energy band between 15 and 30 meV. There are two sharp peaks between 87 and 100 meV in the ab initio curve, whereas the new potential shows one broader peak with a shoulder which indicates the second peak. The curves for the partial VDOS of oxygen are in good agreement. Both simulation and ab initio calculation show the main band of states between 12 and 85 meV with similar curve progression and three local maxima at around 35, 47 and 62 meV. These characteristics are also reflected in the generalized VDOS. In addition, the generalized VDOS obtained with neutron scattering [50] is depicted, which shows the same main characteristics of the curve on a qualitative level.

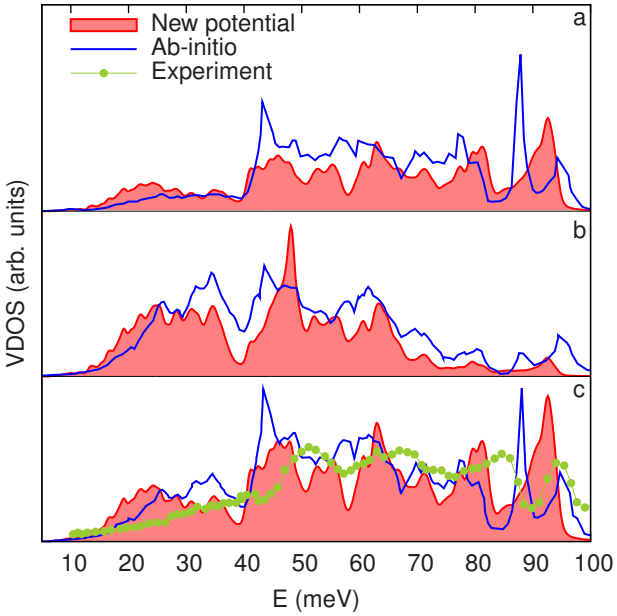

Figure 5.10.: VDOS calculated with the new potential compared with an ab initio study [49] and experiment [50]. a) Partial VDOS for aluminum atoms, b) partial VDOS for oxygen atoms, c) generalized VDOS.

The literature surface energies [52, 55, 69, 85] given in table 5.6 differ among each other which originates from the different methods used in the ab initio approaches. The ab initio calculation of the (0001) surface energy by Hocker [32] agrees with the value obtained in Ref. [69], where also the VASP code with the same pseudopotential and exchange-correlation approximation was used. For all investigated surfaces, the energies obtained with the new potential and with ab initio methods agree. Both results reveal that the (0001) surface has the lowest surface energy and the $(0\bar{1}10)$ surface the highest one. The studies of Ref. [52, 55, 85] yield slightly higher energies for all investigated surfaces.

The surface structure after relaxation is shown in figure 5.11. This comparison study was done by Hocker [32]. It reveals that the Al atoms of the outermost Al-layer are moved closer to the outermost O-layer at the (0001)

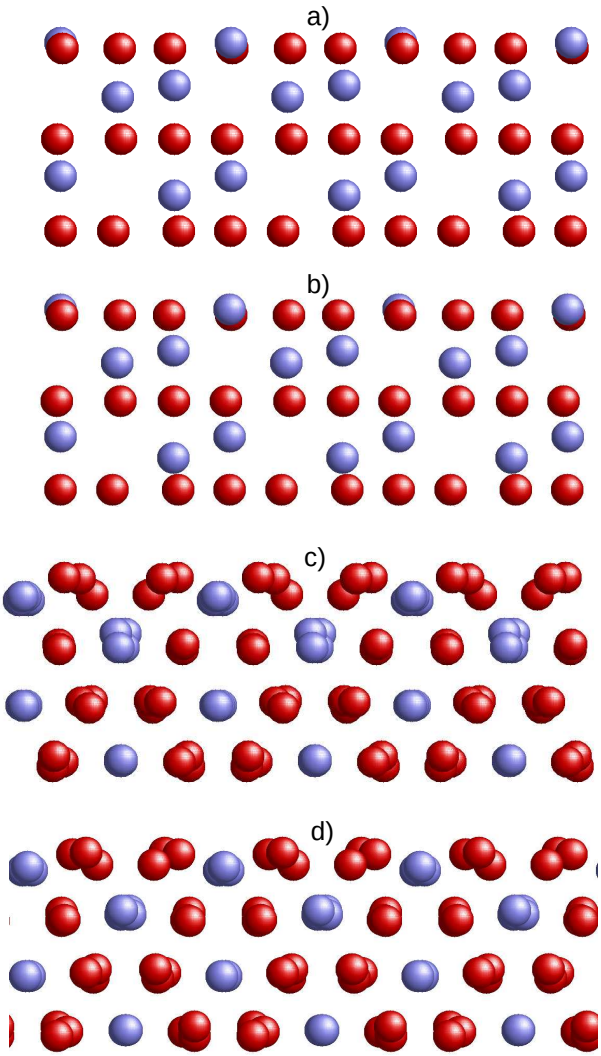

Figure 5.11.: Surface relaxations for the new potential compared with ab initio calculations. Red: oxygen. Blue: aluminum. a) (0001)-surface, ab initio, b) (0001)-surface, MD, c) $(0\bar{1}10)$-surface, ab initio, d) $(0\bar{1}10)$-surface, MD. This comparison study was done by Hocker [32].

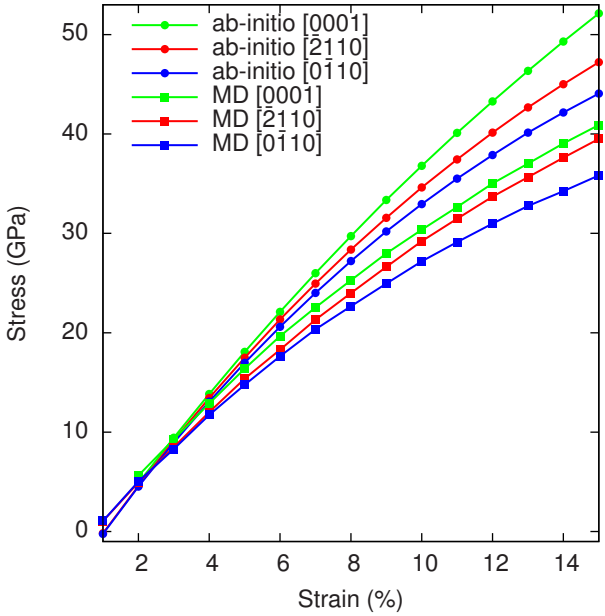

Figure 5.12.: Stresses of strained configurations with [0001] (green), [$\bar{2}$110] (red) and [0$\bar{1}$10] (blue) strain directions against the stress tensor component in direction of strain. The curves obtained with the new potential are marked with squares, those from ab initio calculations with circles. The stress calculation was done by Hocker [32].

Al-terminated surface, which is known to be the most stable (0001) surface termination. The atomic adjustment perpendicular to the surface obtained with the new potential agrees very well with the ab initio results. The distance of an Al- and an O-layer is 0.83 Å, whereas this value decreases to 0.15 Å (MD) respectively 0.14 Å (ab initio) at the surface. A relaxation of the oxygen atoms can be seen at the (0$\bar{1}$10) surface. Both MD and ab initio study show that the three oxygen atoms per unit cell – which are initially in a row along the direction orthogonal to the plane of figure 5.11 – relax to different distances from the initial surface. Furthermore, a relaxation towards the neighboring Al-atoms in the first layer occurs. The results obtained with the new potential again coincide with the ab initio calculation.

One difference, however, can be seen at the second layer: Every second Al atom in each row orthogonal to the figure plane is slightly displaced towards the surface in the ab initio relaxation. This effect is not observed in the MD relaxation simulation. Neither the MD nor the ab initio relaxation study of the $(\bar{2}110)$ surface yield significant atomic movements.

As described in section 5.3.1, strained configurations with strain directions [0001], $[\bar{2}110]$ and $[0\bar{1}10]$ were added in the reference database for the potential optimization approach. To clarify whether the new potential can reproduce the stresses of strained configurations, these stresses are calculated by Hocker [32] using MD with the new potential. Figure 5.12 shows a comparison of stresses obtained in simulations to the stresses of the underlying ab initio reference configurations, each with 360 atoms. They are strained up to 15% in [0001], $[\bar{2}110]$ and $[0\bar{1}10]$ direction respectively. The difference between MD and ab initio results is small at lower strains. With increasing strain, the difference increases up to about 10 GPa at 15% strain. The new potential underestimates the stress in all cases. However, the directions, in which the stress increases, can be reproduced correctly: The highest stresses are observed for strains in [0001] direction, the lowest stresses are found for configurations strained in $[0\bar{1}10]$ direction.

In summary, the new potential can be used to simulate mechanical and vibrational properties of crystalline α-alumina – bulk as well as systems containing surfaces – with high accuracy. As in the case of silica and magnesia, the new potential can be applied to lots of investigations, which could not yet be adequately investigated with MD simulations due to large system sizes or boundary condition restrictions. This is especially the case when simulating crack propagation scenarios, where more atoms and longer timescales are needed than in simple bulk simulations. The detailed investigation of propagating cracks studied by MD simulations with the new force field at hand is presented in chapter 7. The force field is again applied in chapter 8, where the influence of mechanical strain on the field of electrostatic dipole moments is investigated.

Chapter 6.

Significance of dipole moments

In the previous chapter, the force fields generated for silica, magnesia and alumina were validated as highly accurate. Additionally, it has to be verified, whether the extra simulation effort caused by the new polarizable terms is justified. The present chapter details studies of the dependency of metal oxide properties in MD simulations on the polarizability of oxygen ions. A systematic investigation is not only able to legitimate extra computer costs, but to itemize, for which system properties the effects of electrostatic dipole moments are more important and where the influence is negligible.

For crystalline silica, Herzbach and Binder [31] already showed, that the TS force field is superior to the non-polarizable BKS [89] pair potential models. This trend is also visible in section 3.3.3: The BKS potential underestimates the volume in the equation of state study (figure 3.9) and yields deviations in the angle distribution (figure 3.10) and several crystalline structure parameters (tables 3.1, 3.2 and 3.3). Recently, polarization effects on different properties of various molten fluorides, chlorides and ionic oxides were described by Salanne and Madden [78]. The authors illustrated the impact of polarizability in several exemplary selected systems of these material classes and predicted the general importance for structural and dynamic properties.

In the following, a *systematic* comparison of two types of force fields is shown, which only differ by the presence of the polarizable term; the non-electrostatic and Coulomb terms have in each case the same functional form for both force fields. Hence, differences in MD simulation applications can be attributed to polarizability. To obtain a conclusion with a high degree of universality, MD simulation studies of both liquid and crystalline structures of silica, magnesia and alumina are performed. For each of the three metal oxides, two separately optimized force fields are applied:

μ	rms error	ϕ^0_μ	ϕ_μ
S	ΔF_e	0.216605	0.192220
	ΔF_s	0.040983	0.034099
	ΔF_f	1.866665	1.621107
M	ΔF_e	0.075370	0.116994
	ΔF_s	0.029595	0.022774
	ΔF_f	0.671468	0.529535
A	ΔF_e	0.139316	0.049172
	ΔF_s	0.055651	0.027273
	ΔF_f	0.203966	0.350653

Table 6.1.: rms errors from the optimization of the force fields ϕ_μ (from chapter 5) and ϕ^0_μ (with μ = S, M, A for silica, magnesia and alumina respectively).

(i) ϕ^0_μ (with μ = S, M, A for silica, magnesia and alumina respectively): short range interactions of Morse-Stretch (MS) form (equation 3.13) combined with Coulomb interactions between charged particles (new force fields, detailed in the following).

(ii) ϕ_μ: extension of (i) by adding polarizability to the oxygen ions (exactly the force fields presented in the previous chapter).

For a direct and systematic comparison, type (i) force fields for silica, magnesia and alumina were generated, which consist of a MS short range part combined with Coulomb interactions between charges. The latter are treated with Wolf summation as described in chapter 3.1.3. Hence, the only difference – concerning the functional form – compared to the force fields presented in chapter 5 is the absence of the polarizable term. The parameters, however, differ among each other compared to the polarizable force fields from chapter 5 due to the independently performed generation. Table 6.2 shows the corresponding parameters of the non-polarizable force fields.

Although the potentials ϕ_μ have three more parameters than the ϕ^0_μ (13 compared to 10), they do not describe the reference data significantly better than the ϕ^0_μ. This is illustrated by the rms errors, that are shown in table 6.1. Indeed, there is a trend favoring the polarizable potentials: seven of nine rms errors are better in the case of ϕ_μ. And in the case of

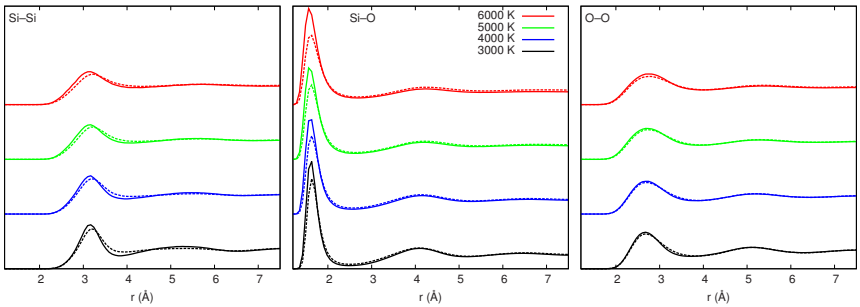

Figure 6.1.: Normalized radial distribution functions for Si–Si, Si–O and O–O in liquid silica at 3000–6000 K. The solid (dashed) curves belong to ϕ_S (ϕ_S^0).

silica and magnesia, the rms errors are – on average – smaller for ϕ_μ than for ϕ_μ^0. For alumina, however, it is the other way round. Thus, the rms errors are only first indicators of the quality of the generated force field, but they are not able to denote the practicability of a potential model.

6.1. Comparison of accuracy in simulations

It appeared already reasonable in chapter 5 that force fields may also yield qualitative results beyond the range for which they were optimized. However such applications beyond the optimization range should be closely verified. In the following, the tests are focused on the range for which the force fields were trained, but results are also shown outside this zone to enlarge the validity of this comparison study.

6.1.1. Microstructural properties

First, the influence of polarizability on microstructural properties is illustrated. The radial distribution functions for liquid silica (4896 atoms) at 3000–6000 K are, in each case, evaluated for 100 snapshots taken out of 100 ps MD runs at the given temperature. The averaged curves are given in figure 6.1. The curves obtained with ϕ_S^0 are similar to the curves of ϕ_S. The existing slight deviations decrease with increasing temperature, so

ϕ_{S}^0	$D_{\mathrm{Si-Si}}$	$D_{\mathrm{Si-O}}$	$D_{\mathrm{O-O}}$
	0.100032	0.100250	0.076883
	$\gamma_{\mathrm{Si-Si}}$	$\gamma_{\mathrm{Si-O}}$	$\gamma_{\mathrm{O-O}}$
	11.009449	11.670530	7.505632
	$\rho_{\mathrm{Si-Si}}$	$\rho_{\mathrm{Si-O}}$	$\rho_{\mathrm{O-O}}$
	2.375990	2.073780	3.683866
	q_{Si}	q_{O}	
	1.799475	-0.899738	
ϕ_{M}^0	$D_{\mathrm{Mg-Mg}}$	$D_{\mathrm{Mg-O}}$	$D_{\mathrm{O-O}}$
	0.038258	0.100261	0.065940
	$\gamma_{\mathrm{Mg-Mg}}$	$\gamma_{\mathrm{Mg-O}}$	$\gamma_{\mathrm{O-O}}$
	9.108854	10.405694	7.962500
	$\rho_{\mathrm{Mg-Mg}}$	$\rho_{\mathrm{Mg-O}}$	$\rho_{\mathrm{O-O}}$
	3.384000	2.417339	3.448060
	q_{Mg}	q_{O}	
	1.100730	-1.100730	
ϕ_{A}^0	$D_{\mathrm{Al-Al}}$	$D_{\mathrm{Al-O}}$	$D_{\mathrm{O-O}}$
	0.002164	1.000003	0.000018
	$\gamma_{\mathrm{Al-Al}}$	$\gamma_{\mathrm{Al-O}}$	$\gamma_{\mathrm{O-O}}$
	10.855181	7.617923	16.719817
	$\rho_{\mathrm{Al-Al}}$	$\rho_{\mathrm{Al-O}}$	$\rho_{\mathrm{O-O}}$
	5.517666	1.880153	6.609171
	q_{Al}	q_{O}	
	1.244690	-0.829793	

Table 6.2.: Parameters for the potentials ϕ_{S}^0, ϕ_{M}^0 and ϕ_{A}^0, given in IMD units set eV, Å and amu.

	a (Å)	c (Å)	$\mathrm{E_{coh}}$ (eV)
ϕ_{A}^0	4.87	13.24	34.71
ϕ_{A}	4.79	12.97	31.85
Ab initio	4.78	13.05	32.31
Experiment	4.75 [92]	12.99 [92]	31.8 [95]

Table 6.3.: Lattice constants and cohesive energy per Al_2O_3 unit of α-alumina at zero Kelvin obtained with ϕ_{A} and ϕ_{A}^0 compared with ab initio results (from Hocker, see section 5.3) and experimental data.

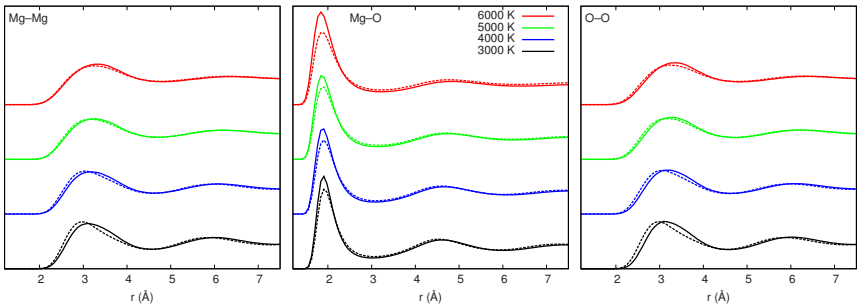

Figure 6.2.: Normalized radial distribution functions for Mg–Mg, Mg–O and O–O in liquid magnesia at 3000–6000 K. The solid (dashed) curves belong to ϕ_{M} (ϕ^0_{M}).

	a (Å)	c (Å)	Si–O (Å)	Si–O–Si
ϕ^0_{S}	4.98	5.47	1.67	139°
ϕ_{S}	5.15	5.50	1.65	148.5°
Theory	4.97 [25]	5.39 [25]	1.61 [24]	145° [24]

Table 6.4.: Lattice constants, Si–O bond length and Si–O–Si angle of α-quartz at 300 K compared with theoretical studies.

the polarizability is more important for lower temperatures. For magnesia (see figure 6.2), the radial distribution functions show comparable behavior: small deviations between ϕ^0_{M} and ϕ_{M}, that decrease with temperature. Apparently, the radial distribution in high temperature oxide melts does not require polarizable oxide ions.

A stronger influence of polarizability is observed on bond angles. Figure 6.3 (left) depicts the oxygen centered angle distribution at 3000–6000 K in liquid silica and magnesia, respectively. Both ϕ^0_{S} and ϕ^0_{M} overestimate the region of lower angles and underestimate the region of higher angles. Potentials with electrostatic dipole moments yield the correct shift of the distributions to slightly higher angles. Again, deviations decrease with increasing temperature. Although ϕ_{A} and ϕ^0_{A} were optimized for low-temperature crystalline structures, the behavior for liquid alumina at 3000 K is probed. Figure 6.3 (right) shows the oxygen centered angle distribution in alumina compared to a recent ab initio study [91]. Although the

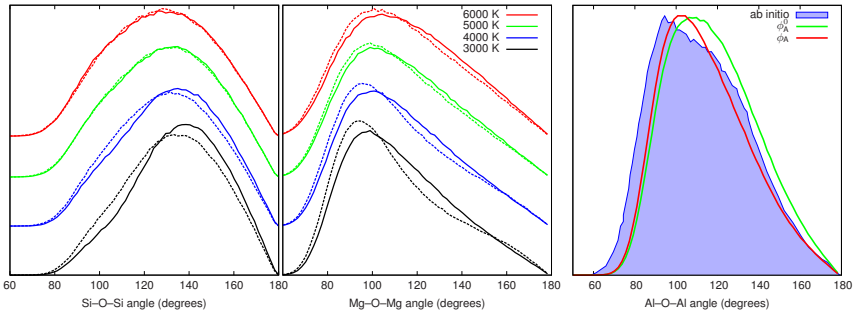

Figure 6.3.: Left: Normalized oxygen centered angle distributions in liquid silica and magnesia at 3000–6000 K for $\phi_{S,M}$ (solid curves) and $\phi^0_{S,M}$ (dashed curves). ϕ^0_S yields a shoulder between around 80 and 130 degrees, whereas the band at around 135–170 degrees is underestimated. Similarly, ϕ^0_M yields a shoulder between around 65 and 95 degrees, whereas the band at around 110–150 degrees is underestimated. Deviations decrease with increasing temperature. Right: The oxygen centered angle distribution in liquid alumina is shown at 3000 K for ϕ_A and ϕ^0_A and compared to an ab initio study [91].

trend of shifting angles to higher values by allowing for polarizability is not reproduced in this case, polarizability yields a curve which is in better agreement to ab initio data. These results coincide with Ref. [78], where the authors stated that polarization effects in ionic systems play an important role in determining bond angles.

The electrostatic dipole moments also influence crystalline structure parameters. The lattice constants of α-alumina are given in table 6.3. ϕ_A yields an accurate agreement both with ab initio and experimental data, whereas with ϕ^0_A the lattice constants are overestimated (in each case around 2% deviation). However, both stabilize the trigonal crystal structure. Lattice constants, Si–O–Si angle and Si–O bond length for α-quartz at 300 K (see Table 6.4) were also determined, which is outside the optimization range for the ϕ_S and ϕ^0_S potentials. The average relative deviation of all parameters is for both potentials very similar (2.6% for ϕ_S and 2.3% for ϕ^0_S). On closer inspection, ϕ^0_S yields more accurate lattice constants, whereas ϕ_S better reproduces the Si–O–Si angle and Si–O bond length. This is consistent with [78] and the results above concerning liquid metal

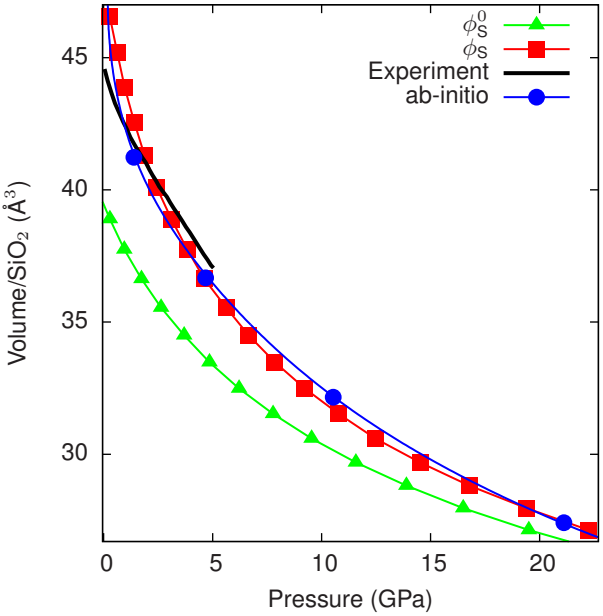

Figure 6.4.: Equation of state of liquid silica at 3100 K for ϕ_S and ϕ_S^0 compared with experiment [21] and ab initio calculations [38].

oxides, where also the polarizability is more important for an improved description of bond angles than for atomic distances.

6.1.2. Thermodynamic properties

The cohesive energy for α-alumina is shown in table 6.3. ϕ_A coincides with ab initio and experimental results, ϕ_A^0 overestimates the cohesive energy (averaged deviation of 8.3%). This clear deviation shows that electrostatic dipole moments have to be taken into account, when probing macroscopical system properties.

To investigate the influence of polarizability on other thermodynamic properties, the equation of state of liquid silica (3100 K, see figure 6.4) and magnesia (5000 K and 10 000 K, see figure 6.5) respectively was obtained on the lines of the validation simulations in chapter 5. The curves obtained

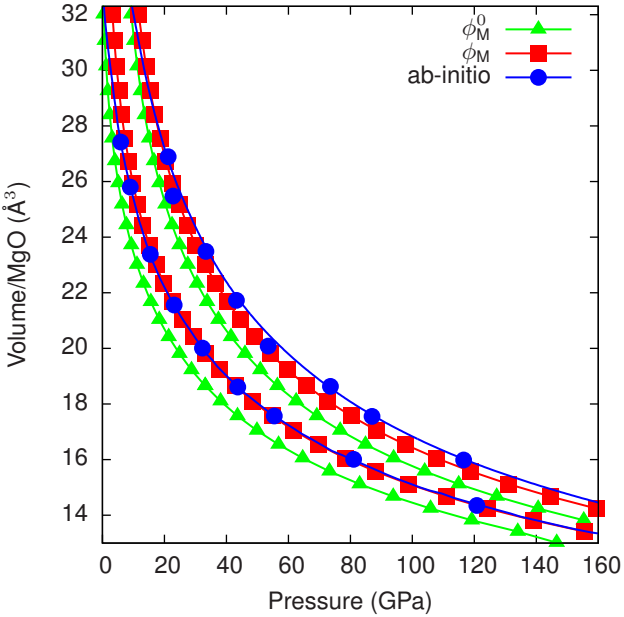

Figure 6.5.: Equation of state of liquid magnesia at 5000 K (left three curves) and 10 000 K (right three curves) for ϕ_M and ϕ^0_M compared with ab initio calculations [37].

with ϕ_S and ϕ_M coincide with ab initio results as well as with experiment in the case of silica. The potentials ϕ^0_S and ϕ^0_M, however, show a clear underestimation of the volume, which illustrates the need for polarizability. The insufficiency of ϕ^0_M does not decrease with increasing temperature as in the case of microstructural properties. For the equation of state, polarizability has to be taken into account regardless of the simulation temperature.

6.2. Stress analysis and summary

Apparently, the equation of state of liquid oxides shows the most significant difference between ϕ^0_μ and ϕ_μ; the potentials without polarizability seem to lack a significant contribution to the pressure. The additional pressure

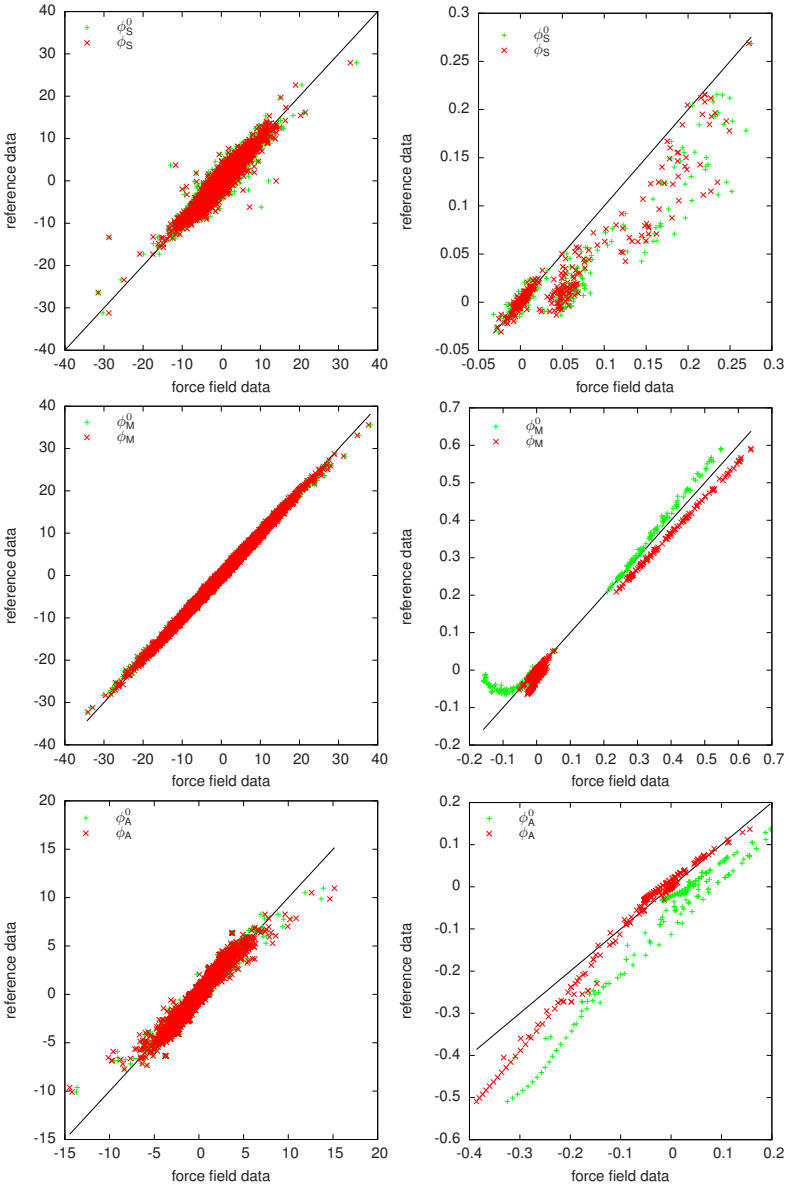

Figure 6.6.: Values computed by each potential (top silica, central magnesia, bottom alumina) plotted against its reference data value. A point placed on the bisecting line corresponds to perfect matching. Left: force components of each configuration (in meV/Å); right: stress components of each single atom (in MPa).

in simulations with ϕ_μ can however not directly be attributed to dipolar interactions. An analysis of the virial showed that U_{qp} and U_{pp} (see equation (3.20)) only contribute about 1.2% of the total virial (and thus the pressure); the higher pressure for these systems results almost exclusively from stronger MS and Coulomb contributions to the virial. As the atomic forces are described with comparable precision for both sets of potentials, this implies that the dipolar interaction is required to obtain correct pressures and forces simultaneously, especially as the concerning polarizable force fields have higher absolute values of the atomic charges.

When looking at the parameters of the respective force fields, it is noticable that in the ϕ^0_μ, the MS potentials are stronger at smaller atomic distances: The absolute value of the MS strengh D_{ij} is higher and the stretch length ρ_{ij} (cf. equation (3.13)) is shorter in the non-polarizable potentials. This seems to indicate that in this case MS is required to describe the atomic interactions for nearest neighbours, while the dipolar interactions provide these contributions for the force fields with polarization.

A better insight is uncovered by inspecting in detail, how accurate the reference ab initio forces and stresses are reproduced by the particular force fields: Figure 6.6 depicts scatter plots, where for each single quantity (force component, stress component) the value computed by the potential is plotted against its reference data value. Hence, for perfect matching a point is placed on the bisecting line. As can be seen from the left three graphs of figure 6.6 showing the force components of each single atom, both force field types ϕ_μ and ϕ^0_μ yield distributions scattered around the bisecting line. The only difference between ϕ_μ and ϕ^0_μ is how accurate the bisecting line is hit. In the right graphs, however, where the stress components of each configuration are depicted, clear deviations are uncovered: For silica, ϕ^0_{S} just reproduces the stresses slightly worse than ϕ_{S}. However, ϕ^0_{M} produces unnatural meanderings from the optimal matching at the left end of the graph (negative stress component values). The failure becomes even more apparent in the alumina case, where ϕ^0_{A} underestimates the stresses over the whole data set. To sum up, the scatter plots predict less accuracy for the ϕ^0_μ, when investigating system properties with a strong dependence on stress and pressure.

In summary, the strongest influence of polarizability is observed in macroscopic thermodynamic properties as the equation of state and the cohesive energy. The dipole contributions are indispensable, when simulating system properties, where collective atomic behavior is important; here, the

dipole interplay seems to be of significant importance. Therefore, the collective phenomena, which are investigated in the following two chapters (cracks in chapter 7 and flexoelectricity in chapter 8) are modelled with the polarizable force fields (as presented in chapter 5). Also on a microscopic scale, the role of dipoles is visible. However, the influences are more relevant for bond angle formation than for atomic distances in both liquid and crystalline structures. Simple pair potentials with Coulomb interactions seem to be compatible to describe local radial distributions. Collective dipole mechanisms, however, are important to model the correct bond angles. The influence of polarizability on microscopic distributions always decreases with increasing temperature.

Chapter 7.

Cracks in α-alumina

Below, the first MD simulations of crack propagation in a metal oxide with a potential that takes into account the polarizability of oxygen atoms are presented. The simulations which are detailed in the following were performed by Stephen Hocker [32] with the force field introduced in section 5.3. The first section (7.1) addresses the analysis of the propagation directions obtained by cooperation with Hocker [32]. The second section (7.2) focusses on the investigation of the influence of cracks in α-alumina on the dipole field which was done by the author with the visualization support of Sebastian Grottel [28].

7.1. Crack propagation

To investigate crack propagation at constant energy release rate, configurations were prepared with dimensions (b_x, b_y, b_z) of $21 \times 3 \times 13$ nm^3 which contain about 80 000 atoms. Lateral planes of these cuboids are the (0001), $(0\bar{1}10)$ and $(\bar{2}110)$ crystallographic planes. An elliptical initial crack of 5 nm length in x-direction was inserted on one side of the samples by moving atoms in z-direction (see figure 7.1). The opening of the crack is always calculated with the Griffith criterion: In front of the crack tip the sample is linearly strained until the elastic energy due to strain is equal to the Griffith energy G_0 which is twice the surface energy of the crack plane. This criterion was fullfilled at about 4% strain. These structures were then relaxed to obtain the displacement field of a stable crack. Periodic boundary conditions were applied in the direction along the crack front, whereas fixed displacement boundary conditions were applied in the other directions. Initial configurations for crack propagation simulations with different energy release rates were obtained by a linear scaling of this displacement field. During the crack propagation simulations, the NVE

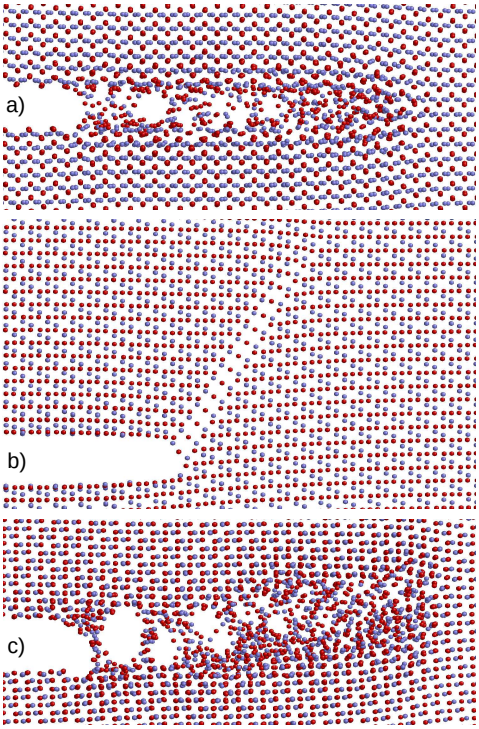

Figure 7.1.: Crack propagation in α-Al_2O_3 (Al-atoms blue, O-atoms red). a) Initial crack in $(\bar{2}110)$ plane, b) initial crack in (0001) plane, c) initial crack in $(0\bar{1}10)$ plane.

ensemble and a starting temperature of 0 K were applied.

Since effects from the boundary conditions (which involve unnatural surfaces in some directions) should be excluded, a crack propagation test simulation with periodic boundary conditions in all directions was performed. In this case, a symmetrical crack was inserted in the middle of the sample. As long as the two crack tips are far away from each other (which is true up to about 5 nm distance), the same result as with the boundary conditions described above are observed. Hence, possible boundary condition effects can be excluded.

7.1.1. Cracks in a $(\bar{2}110)$ plane

Initial cracks were inserted in a $(\bar{2}110)$ plane with crack propagation directions [0001] or $[0\bar{1}10]$. In both cases, the initial crack is stationary at energy release rates up to $1.5\,G_0$. Higher energy release rates lead to crack propagation in the initial $(\bar{2}110)$ plane. It is known that the discrete character of interatomic bonds which reveals itself in the so called lattice trapping effect can retard crack propagation to energy release rates beyond the critical energy release rate determined by the Griffith criterion. As can be seen from figure 7.1 a), yet at high energy release rates bond breaking between the two crack lips is not continuous. Chains of atoms bridging the crack lips stay intact during the simulation. Furthermore, considerable disorder is observed at the resulting crack surfaces. In $[0\bar{1}10]$ propagation direction, these effects are slightly more pronounced than in [0001] propagation direction. It cannot be ruled out that these very strong bonds are caused by inaccuracies of the force field. However, the observation of intact bonds bridging the crack lips agrees with previous simulations of alumina, where it was stated that these atomic chains were observed in experiments as well [98]. The present results show that cracks are able to propagate in $(\bar{2}110)$ planes in both [0001] and $[0\bar{1}10]$ directions. This is in accordance with electron micoroscopy experiments [59], where it turned out that cracks occur in a $(\bar{2}110)$ plane although these are not the preferred fracture planes.

7.1.2. Cracks in a (0001) plane

The (0001) planes are the closest packed planes of α-Al_2O_3; therefore cleavage of these planes is improbable. The present simulations confirm that cracks do not propagate in the (0001) plane in which the initial crack was inserted with crack propagation directions $[\bar{2}110]$ or $[0\bar{1}10]$. At energy release rates below $1.7\,G_0$, a damaged region in front of the crack tip was generated with atomic disorder similar to the case of the $(\bar{2}110)$ plane. However, the crack tip did not move. More interesting is the $(0001)[0\bar{1}10]$ oriented initial crack at higher energy release rates: As can be seen from figure 7.1 b), the crack propagates in a $(10\bar{1}2)$ cleavage plane. Due to the boundary conditions, the crack surfaces cannot separate completely, but a row of oxygen atoms stays in the crack path. In contrast to the cracks in a $(\bar{2}110)$ plane, there is no disorder along the crack surfaces. The observed crack propagation in a $(10\bar{1}2)$ cleavage plane agrees well with electron mi-

croscopy investigations [59] which revealed that fracture surfaces of the $(10\bar{1}2)$ cleavage planes are frequently observed in α-alumina.

7.1.3. Cracks in a $(0\bar{1}10)$ plane

Cracks initially inserted in a $(0\bar{1}10)$ plane in $[\bar{2}110]$ direction propagated in this orientation starting at energy release rates of $2.2\,G_0$. In the case of a [0001] crack propagation direction (figure 7.1 c), the movement of the crack tip was observed at energy release rates above $1.9\,G_0$. Similar to the case of the $(0001)[0\bar{1}10]$ orientation, the crack changed its propagation plane. As can be seen in figure 7.1 c, the crack moved partially in the initial $(0\bar{1}10)$ plane, but also partially in a $(10\bar{1}2)$ cleavage plane. As in the case of cracks in $(\bar{2}110)$ planes, the initially $(0\bar{1}10)[\bar{2}110]$ or $(0\bar{1}10)[0001]$ oriented cracks generate disorder at the crack surfaces during crack propagation; some atomic bonds stay intact across the crack opening.

In summary, simulation results performed with the force field presented in section 5.3 agree well with recent electron microscopy investigations [59]. Propagation directions as well as microstructural behavior of different cracks in α-alumina coincide in both studies.

7.2. Influence of crack on dipole field

The crack samples have a non-vanishing and heterogeneous strain field. The orientation of electric dipole moments in crack propagation simulations can then differ significantly from the orientations in other configurations of the same material due to effects of strain. In addition, the presence of charged surfaces influences dipole orientations. In the following, the two most meaningful crack simulations are picked to investigate the electrostatic dipole field:

(1) crack in a $(\bar{2}110)$ plane propagating in $[0\bar{1}10]$ direction as analyzed in section 7.1.1 and shown in figure 7.1 a),

(2) crack inserted in a (0001) plane propagating in a $(10\bar{1}2)$ cleavage plane as analyzed in section 7.1.2 and depicted in figure 7.1 b).

Charged crack surfaces depend on the crack propagation planes. As shown in figure 7.1 a), the initial surfaces of type (1) cracks are oxygen

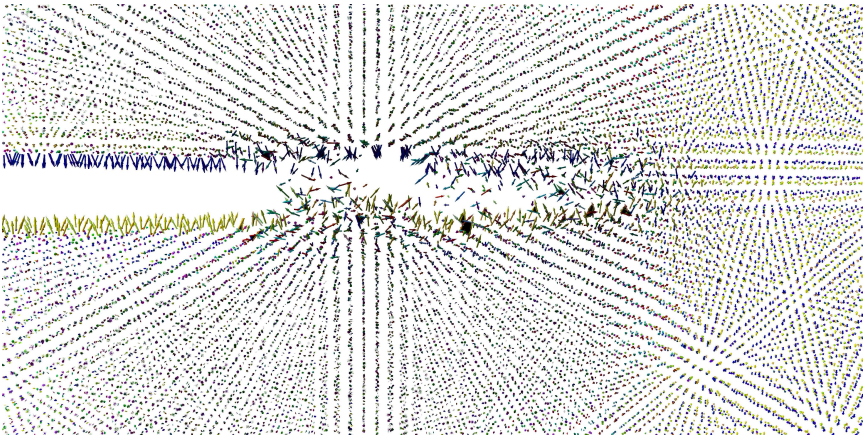

Figure 7.2.: Type (1) crack, aluminum atom sphere glyphs are removed for a clear view. The oxygen terminated surfaces of the crack show the expected alignment of induced dipole moments: Above the crack, dominant blue arrows point to the crack, below the crack, dominant yellow arrows point to the crack. Dipoles are aligned in the region in front of the crack tip which corresponds to the strained part of the configuration. Surface effects, however, induce stronger dipole moments as can be seen from the length of the arrows.

terminated. Therefore, it can be expected that the dipoles of the oxygen atoms at each crack surface are aligned in the same direction and the alignment on the other crack surface is the other way round. This adjustment is reproduced in simulation, as can be seen in figure 7.2. It is significantly more pronounced at the surfaces of the initial crack (left part of the crack in figure 7.2), but it can be seen also along the crack surfaces created by the propagation (right part of the crack). In the latter case, the disorder along the crack surfaces and the intact atomic chains across the crack opening reduce the alignment.

Collective orientation mechanisms of electric dipole moments due to strain can only be observed in crystals, where the inversion symmetry is broken. Therefore, in bulk α-Al_2O_3 usually no dipole alignment is observed. In the crack propagation simulation, however, the inversion symmetry is broken by the crack itself, because it causes a heterogeneous strain

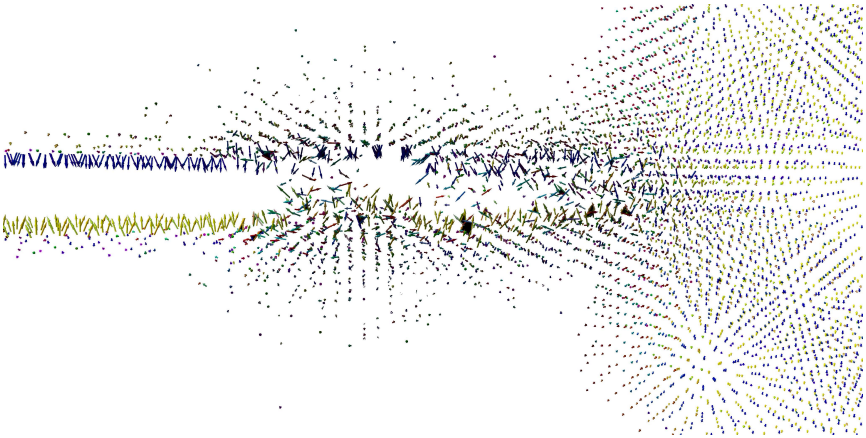

Figure 7.3.: Same situation as in figure 7.2, but moments with magnitudes smaller than 40% of the maximal magnitude are filtered out.

situation. As can bee seen from figure 7.2, collective orientation of the electric dipole moments is observed. Dipoles are aligned in the region in front of the crack tip which corresponds to the strained part of the configuration. On the contrary, in the unstrained regions below and above the crack surfaces the dipoles show no preferred orientation. The different orientation regions are more pronounced by the shading mechanism discussed in section 4.2.2. These so-called flexoelectric effects of heterogeneous strain on the dipole field are investigated in more detail in chapter 8.

All effects of collective dipole behavior become even more apparent, when a filter (introduced in section 4.1) is applied. Figure 7.3 shows the same dipole field as in figure 7.2, but moments with magnitude smaller than 40% of the maximal magnitude are filtered out. From this it follows that the region in front of the crack not only features collective oriented but also stronger dipole moments than regions below and above the crack.

Figure 7.4 finally shows four snapshots taken out of the 5 ps trajectory of a type (1) crack simulation (1 ps simulation time between each snapshot). This time, iso surfaces in the FA field are shown to separate the regions with high dipole order in front of the crack from regions with low order above and below the crack. In this way, a time-resolved observation of the influence of the crack on the dipole field is possible. During the whole crack

analysis, an iso value of 0.81 was found to be sufficient. In the following, it is detailed, how the crack disturbes the field of oriented dipole moments. Several mechanisms were uncovered by the FA visualization technique and are presented below.

7.2.1. Vesicular disorder regions

Figure 7.5 depicts a type (2) crack – at first a snapshot at the very beginning of the simulation. Although the crack did not yet change its propagation direction, it already has an influence on the alignment of the surrounding dipole moments. This can be seen through the considerably different iso surface shapes above and below the crack. Above the crack one can observe a large region of uncorrelated orientation, whereas below only a very small similar area exists. This behavior can be understood when considering the strain situation: The type (2) crack energetically prefers a $(10\bar{1}2)$ cleavage plane which can only be entered by bending up. Bending down would result in a backwards motion that can be excluded due to the crack setup. Hence, the mechanical influence of the crack on the region above is different than on the region below.

The lower picture of figure 7.5 shows the same simulation run after 2.4 ps. At this point, the crack has changed its propagation direction and a vesicular disorder region moving away perpendicularly from the crack can be seen (blue arrow); its averaged diameter is 42 Å. This type (2) setup most clearly uncovers one of the disturbance mechanisms of a crack on the dipole field: No homogeneous realignment in the field of dipoles takes place, but vesicular disorder regions coming from the crack enter the formerly correlated regions and act as nuclei for disturbing the correlations and finally yield isotropic orientations of dipole moments.

7.2.2. Circular waves

Another observation revealed by the FA approach are waves in the electric dipole field. They are the second disturbance mechanism caused by the propagating crack. Figure 7.6 shows a circular wave of dipole disorder coming from the crack tip. Whereas waves in the atomic lattice (phonons) caused by a crack are already known and analyzed in detail, these dipole waves are a first-time observation in atomistic simulations. An investigation of the correlation of dipole waves with phonons is not required, because

it is intrinsic: The dipole moments are calculated self-consistently in each MD step; hence collective dipole and atomic behavior are coupled by the method of the force field.

7.2.3. Stationary waves

It is expected, that stationary waves can be caused by introducing fixed boundaries. Figure 7.7 shows six snapshots taken out of a type (1) crack simulation at intervals of 20 fs. In this visualization, the scalar field of FA reveals a stationary wave in the dipole field between the crack tip and the fixed boundary on the right. The disturbance coming from the crack tip is stabilized by the fixed boundaries on bottom and on top of the sample. It is very interesting that the crack – although its front takes less than 20% of the samples width – also acts as a fixed boundary for the wave. With the given colormap (see figure 4.5), wave peaks can be identified: The brighter whitish color of the large area in front of the crack in the first and the last image show the positive wave peaks while yellow-orange in the two center images represent the negative wave peak. Hence, the period of this stationary wave is around 100 fs.

In summary, the influence of a crack on the dipole field can be described by two phenomena: Perpendicular to the crack propagation direction, vesicular disorder regions enter the aligned dipoles and act as nuclei for disturbing the correlations. In addition, a wave-like disturbance is coming from the crack tip. The MD simulations with the force field presented in section 5.3 are able to make a statement concerning typical wavelengths and periods of time.

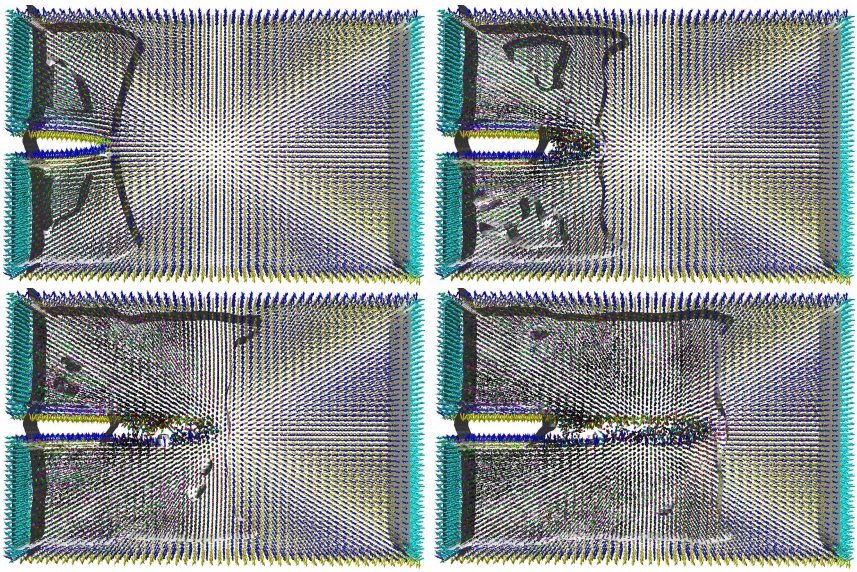

Figure 7.4.: Four snapshots taken out of the full simulation trajectory of a type (1) crack (above left at the beginning, above right after 1 ps, below left after 2 ps and below right after 3 ps). Iso surfaces in the FA field are shown to separate regions with high dipole order in front of the crack from regions with low order above and below the crack. In addition, vesicular regions of higher order inside the uncorrelated regions above and below the crack are uncovered. This indicates that the influence of the crack on the dipole field is a heterogeneous process. The more the crack is advanced, the more homogeneous the FA field above and below the crack becomes. The occuring vesicular regions are detailed in section 7.2.1. From [28].

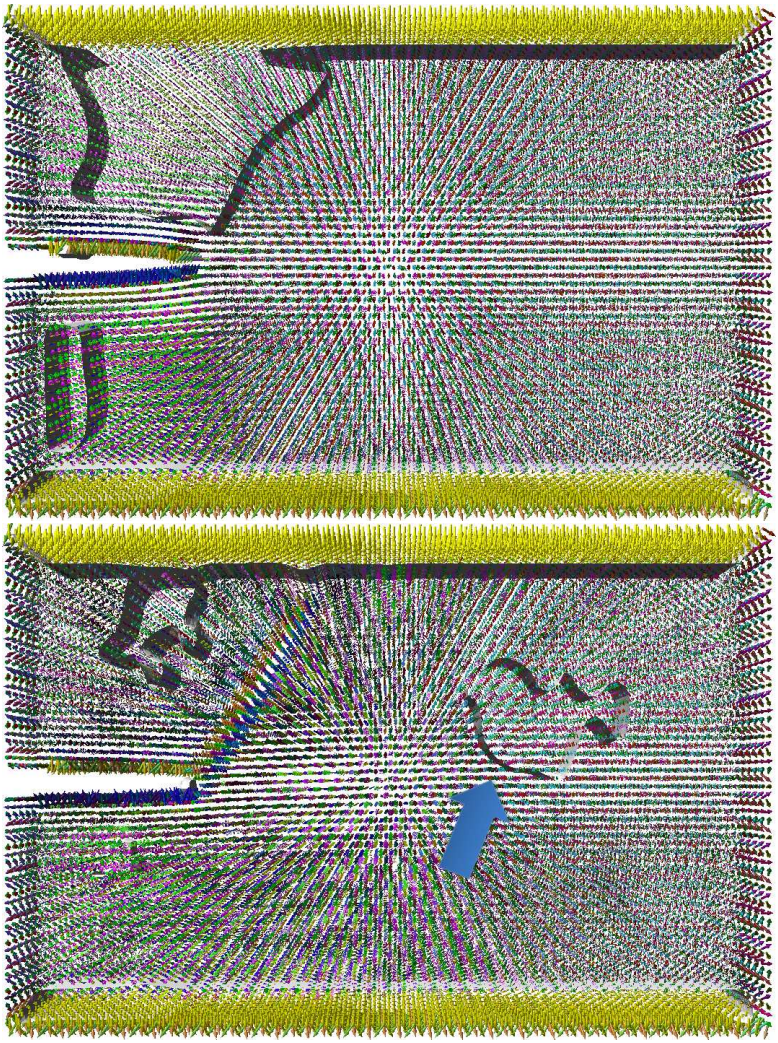

Figure 7.5.: Above: Snapshot of a type (2) crack at the very beginning of the simulation, from [28]. A higher degree of disordered dipole orientations above the inserted crack than below is visible through the iso surfaces. Below: Same situation after 2.4 ps and after changed crack propagation direction. A vesicular disorder region propagates approximately perpendicular to the crack (blue arrow).

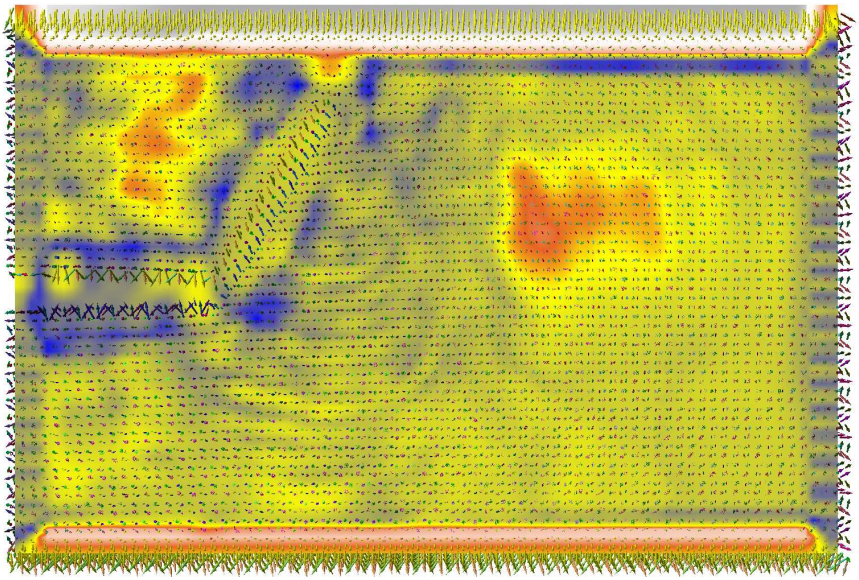

Figure 7.6.: The FA scalar field of a type (2) crack simulation reveals a circular wave of dipole disorder coming from the crack tip. The wavelength is about 7.4 Å. The vesicular disorder regions are again visible (red areas). From [28].

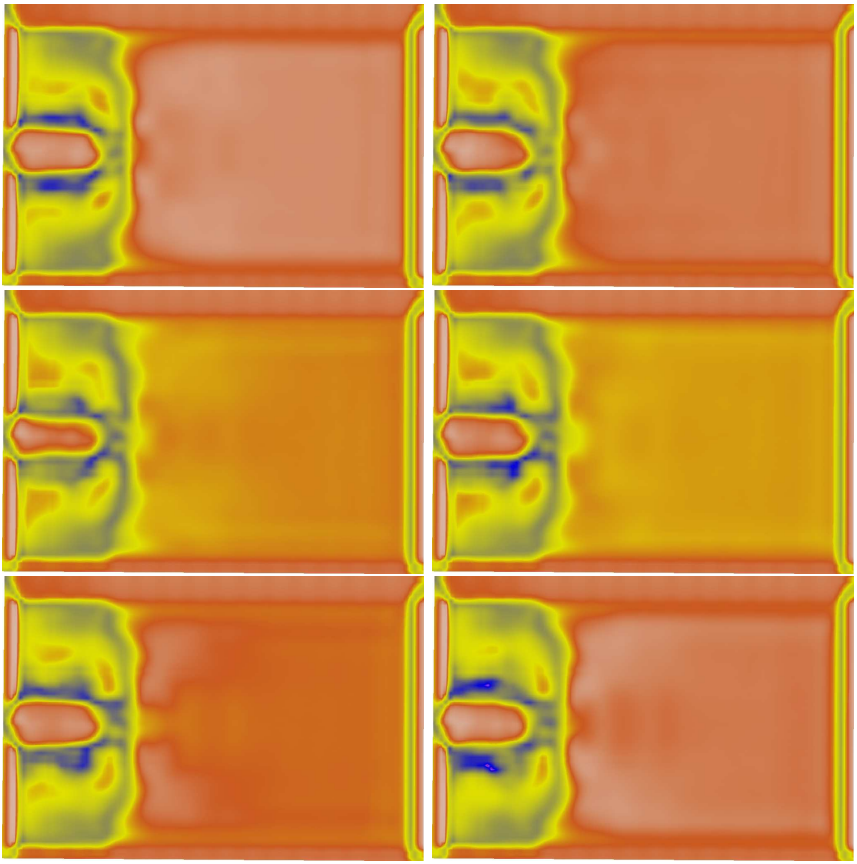

Figure 7.7.: Scalar FA field of type (1) crack simulation at intervals of 20 fs (progression from above left to below right), from [28]. A stationary wave in the dipole field between the crack tip and the fixed boundary on the right is revealed. The brighter whitish color of the large area in front of the crack in the first and the last image show the positive wave peaks while yellow-orange in the two center images represent the negative wave peak.

Chapter 8.

Influence of strain gradient on dipole field

8.1. Piezoelectricity

In 1880, Pierre and Jacques Curie discovered the phenomenon called piezoelectricity, where voltage emerges from a deformation of the material. In a microscopic view, oriented electrostatic dipole moments occur in some materials due to external strain. There exist two kinds of piezoelectric processes: In the first case, the unstrained material has no dipole moments (dielectric medium). Then, the strain causes a displacement of oppositely charged ions against each other forming a dipole moment. In the second case, the material already features dipole moments, but they are randomly oriented (paraelectric medium). Then, the strain causes collective alignment of the available dipoles. Both processes can be investigated with MD simulations by use of the TS force field model. However, one has to keep in mind, that the first process is approached in the TS model by always attaching an arising dipole moment to the oxygen ion. As shown during the whole thesis, this approximation yields very resonable and accurate results for metal oxide systems.

In general, the linear piezoelectric coupling between polarization $\mathbf{P}$ and strain $\underline{\underline{\epsilon}}$ can be expressed by a three-stage tensor d (threefold underlining is omitted for a clear view),

$$\mathbf{P} = d\,\underline{\underline{\epsilon}}, \tag{8.1}$$

which in principle has 27 independent components. Existing symmetries reduce this number. In this context, the polarization $\mathbf{P}$ is associated with the dipole moments $\mathbf{p}_i$ inside of a given volume V by

$$\mathbf{P} = \frac{1}{V}\sum_i \mathbf{p}_i. \tag{8.2}$$

The corresponding free energy density (with the electric field $\mathbf{E}$) is then written as

$$f_{\text{piezo}} = \frac{1}{2}\mathbf{E}\,\mathbf{P} = \frac{1}{2}\mathbf{E}\,d\,\underline{\underline{\epsilon}} = \sum_{i,j,k}^{3} E_k\, d_{kij}\, \epsilon_{ij} \tag{8.3}$$

with E_k, d_{kij} and ϵ_{ij} $(i, j, k = 1, 2, 3)$ the respective tensor components. These equations also include the description of anti-piezoelectricity (antiferroelectric alignment of dipole moments due to strain), because only the amplitude $\mathbf{P}$ of a generalized polarization

$$\tilde{\mathbf{P}} = \mathbf{P}e^{i\mathbf{kr}} \tag{8.4}$$

enters the free energy contribution ($\mathbf{k}$ is the wavevector of a periodic polarization field).

The electric field is expressed by a polar vector $\mathbf{E}$, which changes its sign when inverting spatial coordinates. On the other hand, the strain matrix $\underline{\underline{\epsilon}}$ is inversion-invariant. Hence, the free energy in equation (8.3) would change its sign when inverting spatial coordinates and therefore has to vanish in this case: There is no piezoelectricity in crystalline systems with inversion symmetry.

8.2. Flexoelectricity

In chapter 7 it was shown, that there is very well appearance of collective antiferroelectric dipole alignment in front of a propagating crack in α-alumina, although the point group $\mathrm{D_{3d}}$ contains the inversion. It was stated in section 7.2, that the crack breaks the inversion symmetry by generating a heterogeneous strain situation. This linear flexoelectric coupling between polarization and a strain gradient was first predicted in 1964 by Kogan [40]. Although the analytical description [56, 72, 74, 86] advanced as well as experimental [3, 10, 13, 26, 51, 101] and ab initio [34, 57] studies, there exists no molecular dynamics simulation approach up to now. Indeed, there is one single atomistic approach [54] where also an ab initio based polarizable force field was adopted to model dipole orientation phenomena. However, only the dependence of polarization on the sample size is depicted there. The following results fill the gap.

The linear flexoelectric coupling between polarization $\mathbf{P}$ and a strain gradient $\nabla\underline{\underline{\epsilon}}$ (which is a three-stage tensor) is described by a four-stage

tensor h (again fourfold underlining is omitted),

$$\mathbf{P} = h\,\nabla\underline{\underline{\epsilon}}, \tag{8.5}$$

which in general can have 81 independent components in the case of a total unsymmetric system. The belonging free energy density is then written as

$$f_{\text{flexo}} = \frac{1}{2}\mathbf{E}\,\mathbf{P} = \frac{1}{2}\mathbf{E}\,h\,\nabla\underline{\underline{\epsilon}} = \sum_{i,j,k,l}^{3} E_k\,h_{klij}\,\nabla_l\,\epsilon_{ij} \tag{8.6}$$

with the tensor components h_{klij} $(i,j,k,l = 1,2,3)$. On the lines of the analysis of piezoelectricity, also anti-flexoelectric effects are included with the generalized polarization introduced in equation (8.4).

In contrast to the strain matrix $\underline{\underline{\epsilon}}$, the strain gradient $\nabla\underline{\underline{\epsilon}}$ is not inversion-invariant. Hence, flexoelectricity in principle can also occur in crystalline systems with inversion symmetry, which establishes a new material class for industrial products that are based on generating voltage by deformation of the material or – even more relevant for technological applications – the other way round: generating specific current-controlled deformation.

8.3. Periclase

By investigating periclase (crystalline magnesia with cubic sodium chloride structure), a preferably simple crystalline system is chosen at first to investigate the influence of strain on the dipole field.

8.3.1. Piezoelectric behavior

Following the symmetry argument in section 8.1, no piezoelectricity can occur in periclase, because the respective point group $\mathrm{O_h}$ contains the inversion. The underlying representation theory illustrates symmetry consequences in more details and is shown in preparation for the analysis of flexoelectric coupling.

Table 8.1 depicts the character table of $\mathrm{O_h}$ containing ten inequivalent irreducible representations. The representation of the polar electic field vector $\mathbf{E}$ in the space of $\mathrm{O_h}$ is given by

$$D^E(O_\mathrm{h}) = T_{1u}. \tag{8.7}$$

O_h	e	$6C_4$	$3C_4^2$	$8C_3$	$6C_2$	i	$3\epsilon_h$	$6\epsilon_d$	$8S_6$	$6S_4$
A_{1g}	1	1	1	1	1	1	1	1	1	1
A_{2g}	1	-1	1	1	-1	1	1	-1	1	-1
A_{1u}	1	1	1	1	1	-1	-1	-1	-1	-1
A_{2u}	1	-1	1	1	-1	-1	-1	1	-1	1
E_g	2	0	2	-1	0	2	2	0	-1	0
E_u	2	0	2	-1	0	-2	-2	0	1	0
T_{1g}	3	1	-1	0	-1	3	-1	-1	0	1
T_{2g}	3	-1	-1	0	1	3	-1	1	0	-1
T_{1u}	3	1	-1	0	-1	-3	1	1	0	-1
T_{2u}	3	-1	-1	0	1	-3	1	-1	0	1

Table 8.1.: Character table of O_h with the cubic symmetry elements: identity e, n-fold rotations C_n, inversion i, reflections $\epsilon_{h/d}$ and rotary reflections S_n. The index g stands for even representations, u for odd ones (definition on the basis of the sign of the i-character).

The representation of $\underline{\underline{\epsilon}}$ can be constructed by building the representation product of the representation of a polar vector as $\mathbf{E}$ with itself and then taking the symmetric part:

$$D^{\epsilon}(O_h) = [T_{1u} \otimes T_{1u}]_+ = A_{1g} \oplus E_g \oplus T_{2g}. \tag{8.8}$$

To find the tensor components of d, one has to search for the appearance of the trivial representation A_{1g} when contracting $\underline{\underline{\epsilon}}$ with $\mathbf{E}$ (see equation (8.3)). Following the relationship for the appearance of A_{1g} in the Clebsch-Gordan-coefficients (representation D^{α} has character χ^{α}),

$$(\chi^{\alpha}\chi^{\beta}|\chi^{A_{1g}}) = \delta_{\alpha\beta}, \tag{8.9}$$

one only has to look for identical irreducible representations inside of $D^E(O_h)$ and $D^{\epsilon}(O_h)$. Each irreducible representation, which occurs in both representations, gives reason to an independent entry in the coupling tensor d. As easily can be seen (and as expected), $D^E(O_h)$ contains only even and $D^{\epsilon}(O_h)$ only odd representations. Hence, d does not have any non-vanishing entry and no piezoelectricity occurs in periclase.

Molecular dynamics simulations with the force field presented in section 5.2 are consistent with group theoretical results: A periclase bulk sample was strained homogeneously in different directions and under different

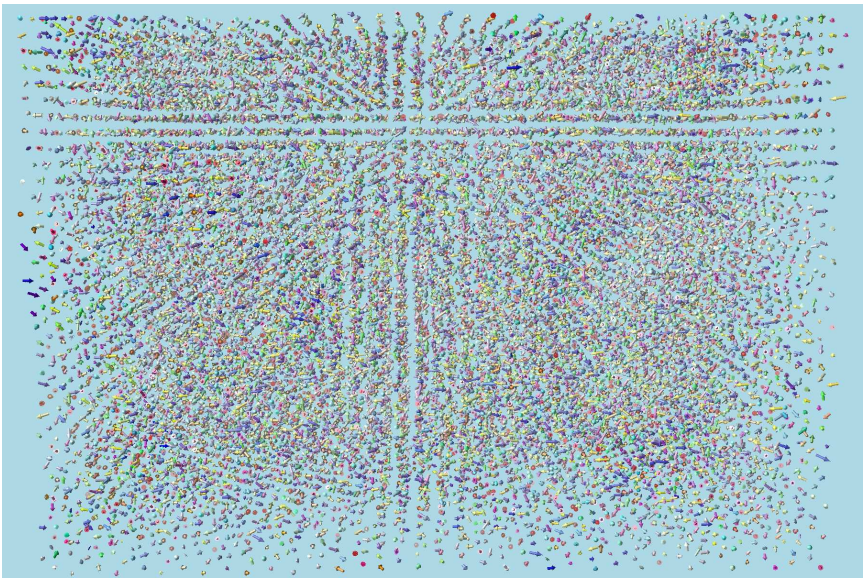

Figure 8.1.: Glyph representation of a periclase snapshot without any filter options. The sample is homogeneously extended in a direction parallel to one of the cubic crystal axis until the edge length in the elongated direction is nearly 50% longer than the perpendicular ones. Nevertheless, no collective alignment of electric dipole moments is visible.

loads and no correlated orientations of dipole moments occur. Figure 8.1 shows a snapshot of a simulation with periodic boundary conditions, where the periclase sample is homogeneously extended in a direction parallel to one of the cubic crystal axis until the edge length in the elongated direction is nearly 50% longer than the perpendicular ones. Nevertheless, no collective alignment of electric dipole moments is visible. The dipoles are randomly oriented over the whole sample, the net dipole moment is negligible. Everywhere, the FA scalar field takes insignificant values. Figure 8.1 can be taken as a reference for the following alignment phenomena.

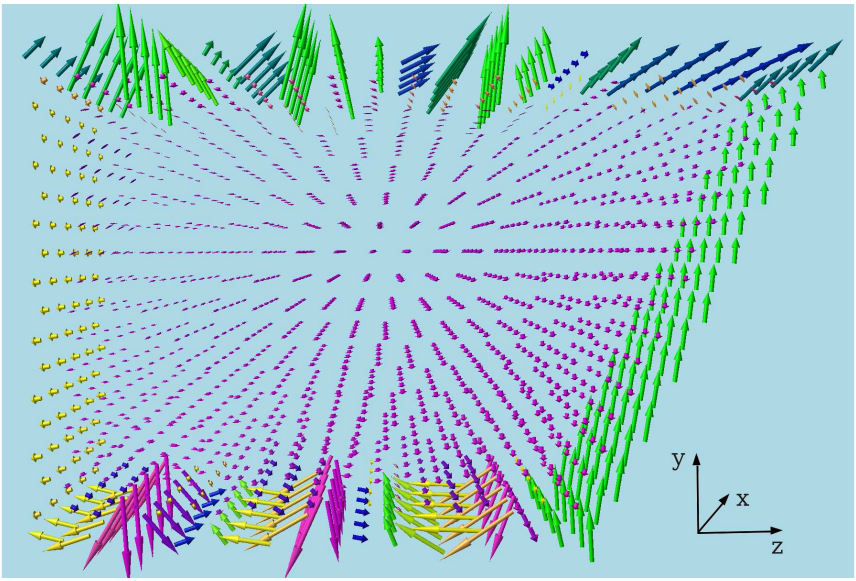

Figure 8.2.: Glyph representation (without filter) of the periclase trapezoid sample. The dipoles of each ion, which do not belong to the fixed boundary, are oriented exactly in the same direction (uniform purple arows), namely perpendicular to the direction of the strain gradient.

8.3.2. Flexoelectric behavior

Contrary to piezoelectric behavior, flexoelectric coupling in periclase is admitted to arise by symmetry aspects. The representation of $\mathbf{E}$ in the space of O_h was already given in equation (8.7). The representation of $\nabla \underline{\underline{\epsilon}}$ can be constructed by building the representation product of the representation of a matrix as $\underline{\underline{\epsilon}}$ (see equation (8.8)) and a polar vector as $\mathbf{E}$:

$$\begin{aligned} D^{\nabla\epsilon}(O_h) &= (A_{1g} \oplus E_g \oplus T_{2g}) \otimes T_{1u} \\ &= A_{2u} \oplus E_u \oplus 3T_{1u} \oplus 2T_{2u}. \end{aligned} \tag{8.10}$$

To find the tensor components of h, one has to search for irreducible representations which occur in both representations $D^E(O_h)$ and $D^{\nabla\epsilon}(O_h)$. In the present case, T_{1u} is found three times which implies three independent tensor entries and the possibility of flexoelectric behavior. The

explicit structure of the coupling tensor h can be obtained by use of the A_{1g}-projector to find the appearance of the trivial representation A_{1g} when contracting $\nabla_{\underline{\underline{\epsilon}}}$ with $\mathbf{E}$. Details of the approach and the explicit flexoelectric free energy density are given in appendix C. The resulting coupling tensor components are given by

$$h_{klij} = (h_{11} - h_{12} - 2h_{44})\delta_{klij} + h_{12}\delta_{kl}\delta_{ij} + h_{44}(\delta_{ki}\delta_{lj} + \delta_{kj}\delta_{li}), \quad (8.11)$$

where δ_{klij} is 1 for all indices equal and zero otherwise. This result is in accordance with the analyses of Maranganti [56] and Shu [81].

A simple way to introduce heterogeneous strain to the periclase sample in MD simulation is to strain the sample in one direction with increasing magnitude along a perpendicular direction. The resulting geometry is a rectangular trapezoid. Taking this trapezoid – with different amounts of strain – as input in IMD, one single NVE simulation step with open boundary conditions was performed to get one full iteration cycle of the TS dipole routine. Longer MD simulations would naturally diminish the strain gradient, because this forced strain situation is unstable. As expected from the symmetry analysis, a strong flexoelectric behavior appears as shown in figure 8.2 (each of the periclase samples shown in this section depicts the most highly strained situation (50%) in order to visualize the strongest flexoelectric effect). Without regard of the unnatural fixed single layer boundary, the dipoles of the whole sample are oriented exactly in the same direction, namely to the bottom right, which is roughly perpendicular to the direction of the strain gradient (top right). Another view of the trapezoid sample was already depicted in figure 4.6 on page 75 as an example for directional similarity (DS).

The dipole alignment in IMD is in accordance with theory: In the trapezoid sample, strain was introduced in z-direction ($\epsilon_{zz} \neq 0$) with a gradient in the yz-plane ($\nabla_y \neq 0$ and $\nabla_z \neq 0$). From equations (8.5) and (8.11), it then follows that the polarization is given by

$$\mathbf{P} = \begin{pmatrix} P_x \\ P_y \\ P_z \end{pmatrix} = \begin{pmatrix} 0 \\ h_{12}\nabla_y\epsilon_{zz} \\ h_{11}\nabla_z\epsilon_{zz} \end{pmatrix}. \quad (8.12)$$

The polarization and with it the dipole moments must be aligned in the yz-plane. Furthermore, already the qualitative analysis of the IMD results predicts a positive (negative) sign for h_{11} (h_{12}).

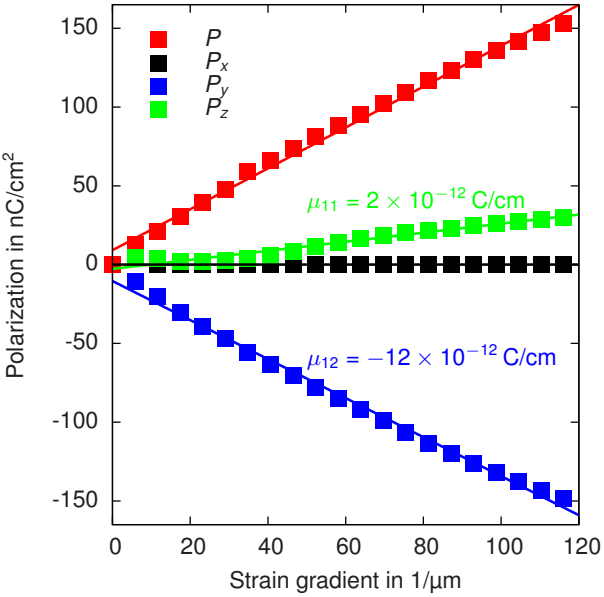

Figure 8.3.: Magnitude $P = |\mathbf{P}|$ of the polarization and the components P_x, P_y and P_z plotted against strain gradient for the periclase trapezoid sample. In all cases, a linear scaling with increasing strain is apparent. The curve of P_x clearly shows, that dipoles are aligned in the yz-plane. From the slope of the curves of P_y and P_z, the flexoelectric coupling coefficients h_{11} and h_{12} can directly be determined.

In the same manner as described before, 20 periclase trapezoid samples strained from zero up to 50% have been set up. As can be seen in figure 8.3, the magnitude P of the polarization (boundary atoms omitted) scales linear with increasing strain. This does not only legitimate the previous made assumption of a linear response theory, but is also in accordance with recent experiments: Cross [13] has shown the linear coupling between strain gradient and polarization for different ionic bulk materials as well as the 2012 published work from Baskaran and He [3] where an investigation of flexoelectric coupling in polyvinylidene flouride films predicts that the flexoelectric polarization is linearly proportional to the strain gradient.

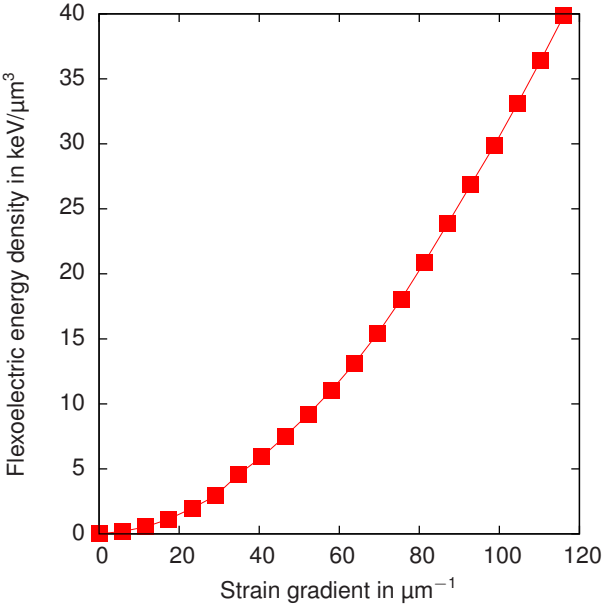

Figure 8.4.: Flexoelectric free energy density as a function of strain gradient.

With equation (8.12), the simulation provides the coupling coefficients h_{11} and h_{12}. Figure 8.3 shows the three components P_x, P_y and P_z of the polarization, where also the linear coupling is verified. The curve of P_x clearly shows, that dipoles are aligned in the yz-plane. From the slope of the curves of P_y and P_z, the flexoelectric coupling coefficients can directly be determined:

$$\begin{aligned} h_{11} &= 2 \times 10^{-12} \, \frac{\mathrm{C}}{\mathrm{cm}}, \\ h_{12} &= -12 \times 10^{-12} \, \frac{\mathrm{C}}{\mathrm{cm}}. \end{aligned} \tag{8.13}$$

There is no prior literature specifying the flexoelectric coupling constants for periclase. There exist, however, several experimental [3, 13, 101] and ab initio [57] studies, where the coupling coefficients of other cubic bulk materials (GaAs, NaCl, KCl, barium and strontium titanate) have been

measured/calculated. The resulting magnitude order for the coupling is always comparably.

The corresponding flexoelectric free energy density can be written as

$$f_{\text{flexo}} \;=\; \frac{1}{2}\,[\; h_{11}E_z\nabla_z\epsilon_{zz} \;+\; h_{12}E_y\nabla_y\epsilon_{zz}\;] \tag{8.14}$$

as shown in appendix C, equation (C.9). By means of equation (8.6), the relationship between magnitude of the polarization and energy density can be obtained:

$$f_{\text{flexo}} = \frac{1}{2}\mathbf{EP} = \frac{1}{2}\frac{V\mathbf{P}}{\alpha}\mathbf{P} = \frac{VP^2}{2\alpha} \tag{8.15}$$

with polarizability α specified in table 5.3 (p. 85). The resulting flexoelectric free energy density is shown in figure 8.4. As the polarization scales linearly with strain gradient (see figure 8.3), f_{flexo} is a quadratic function of strain gradient. The order of magnitude of f_{flexo} is in the range of 0 – 0.5 meV per particle.

8.3.3. Flexoelectric domains

Further insights were obtained by combining two previous used samples to get a douple-trapezoid as input for IMD. Thereby it has to be mentioned that the merging was done before starting an IMD run and calculating the dipole moments via TS model. Otherwise one would simply combine two constructed domains. However, the aim was to reveal how the dipoles align from the start in a sample with the new situation of two different directed strain gradients. Let the trapezoid in figure 8.2 be copied and reflected horizontally. Then, the two trapezoids are connected at its longest edges. The result is the following: In the upper trapezoid, the strain gradient is oriented in bottom-right direction, whereas in the lower trapezoid, the strain gradient is oriented in top-right direction. In the previous section, the dipoles aligned roughly perpendicular to the strain gradient. Hence, in the described double-trapezoid each single trapezoid should become a separable flexoelectric domain. Indeed, this behavior can be achieved as shown in figure 8.5. Two clean and well separated domains are visible within which the dipole moments are oriented almost perpendicular to the direction of the strain gradient. Because the strain gradients of the two domains are orientated perpendicular, also the total dipole moment of the two domains are at right angle.

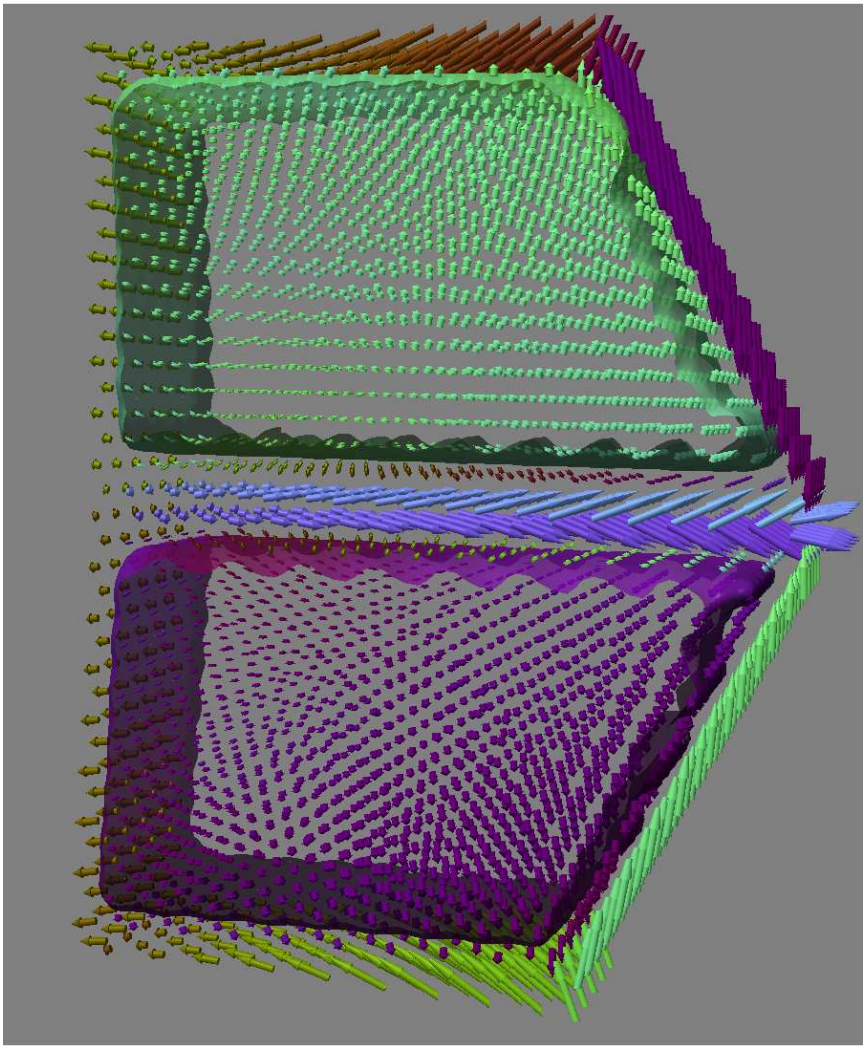

Figure 8.5.: Glyph representation (without filter) of the periclase double-trapezoid sample. Two well separated flexoelectric domains (upper domain green arrows, lower domain purple arrows) are formed by the different directions of strain gradient. Between the two domains, a Néel-Wall (blue arrows) is visible. DS iso surfaces emphasize the well separated domains. Visualization support from [79].

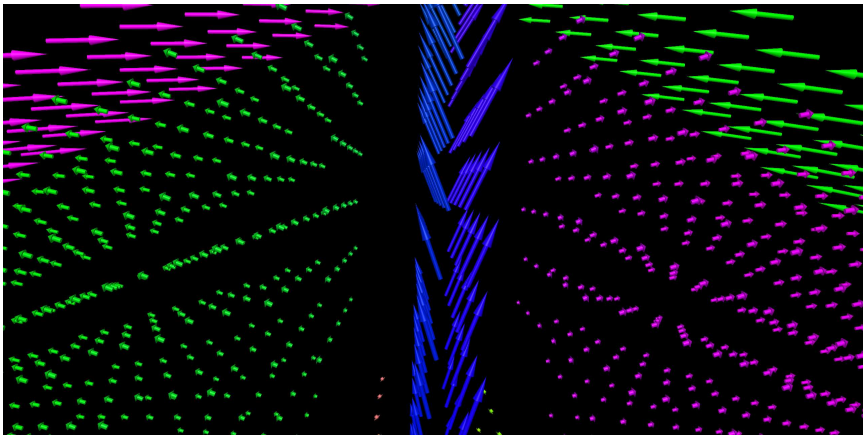

Figure 8.6.: Zoomed view on the Néel-Wall of the same sample as depicted in figure 8.5. Moments with magnitude smaller than 5% of the longest ones were filtered out for a clear view.

The scenario of two flexoelectric domains reveals a new finding: Inside of the domain wall, which stresses across four atomic layers (two oxygen layers are visible in figure 8.5 via blue arrows), the dipole moments rotate around an axis parallel to the wall plane. From magnetism, this kind of domain border crossing is known as Néel-wall. Figure 8.6 shows a zoomed view on the wall.

Finally, four trapedoids have been combined similarly to the previous case to get a fourfold-trapezoid as input for IMD. The construction is not done by merging two double-trapezoids because this hexagon-scenario yields a symmetric sample, in which again two domains are formed. In fact, four single trapezoids are merged in a manner to construct a preferably unsymmetrical strain situation. The resulting arrow-like periclase sample is shown in figure 8.7. As can be seen clearly, four well separated flexoelectric domains arise. In each domain, the dipole moments are oriented approximately perpendicular to the direction of the local strain gradient. Unfortunately, the color coding is not accurate enough to distinguish between the dipoles of domain top-left and domain bottom-right (or between domain top-right and bottom-left). However, the directions are directly given by the arrow-glyph representation. Due to the described alignment,

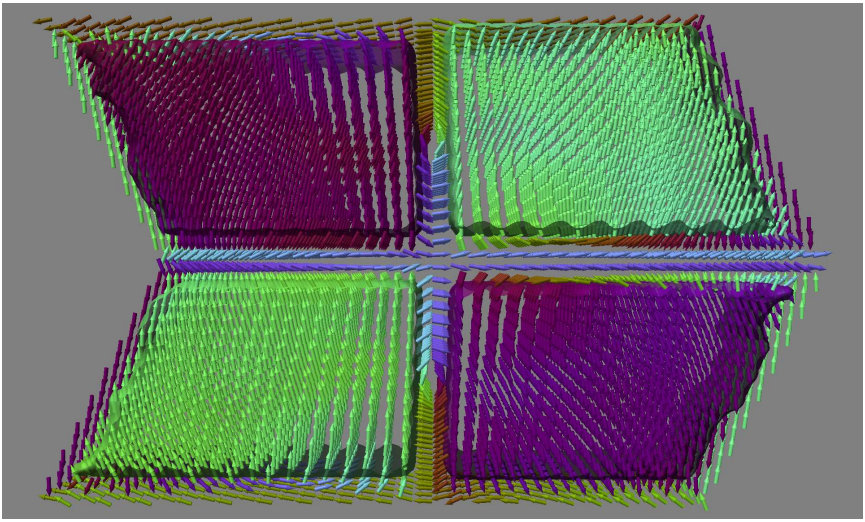

Figure 8.7.: Normalized glyph representation (without filter) of the periclase fourfold-trapezoid sample. Four flexoelectric domains, separated by Néel-walls, arise. DS iso surfaces emphasize the well separated domains. Visualization support from [79].

the direction of dipoles of domain top-right and bottom-right are oriented away from one another. In contrary, the direction of dipoles of domain top-left and bottom-left are oriented to each other. This difference may explain the domain wall alignment detailled in the following. Figure 8.8 shows the same situation with additional filtering of dipoles which do not belong to any domain. This view further highlights the clear separation of four flexoelectric domains.

Two domains are in each case separated by Néel-walls which is emphasized in figure 8.7 by four zoomed-in views. Due to the previous described dipole alignment inside of the domains, the domain walls differ among each other. Because the four walls converge in the center of the sample, the vertically running walls are not homogenously. Between the center and the edges of the sample, those walls exhibit a rotation of orientation (from blue near the center to orange near the edge).

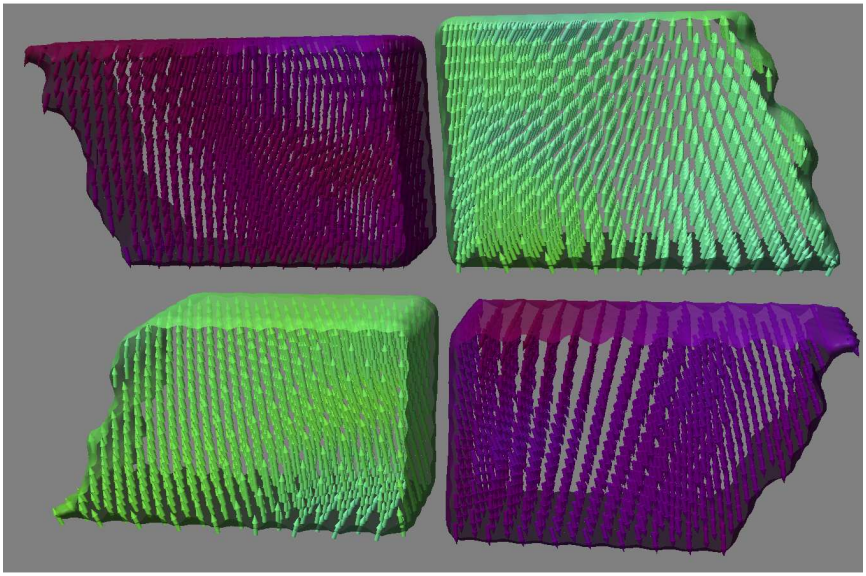

Figure 8.8.: Same situation as in figure 8.7 with filtering of dipoles which do not belong to any domain. Visualization support from [79].

8.4. α-Alumina

The second selected and more complex crystalline system is α-alumina, which has hexagonal scalenohedral crystal structure (see figure 5.9).

8.4.1. Piezoelectric behavior

On the lines of the periclase analysis, no piezoelectricity is allowed to occur in α-alumina, because the point group D_{3d} contains the inversion. Again, representation theory is applied for detailing the symmetry analysis.

Table 8.2 shows the character table of D_{3d} containing six inequivalent irreducible representations. The representation of $\mathbf{E}$ in the space of D_{3d} is given by

$$D^E(D_{3d}) = A_{2u} \oplus E_u. \tag{8.16}$$

The representation of $\underline{\underline{\epsilon}}$ is constructed again by building the representation

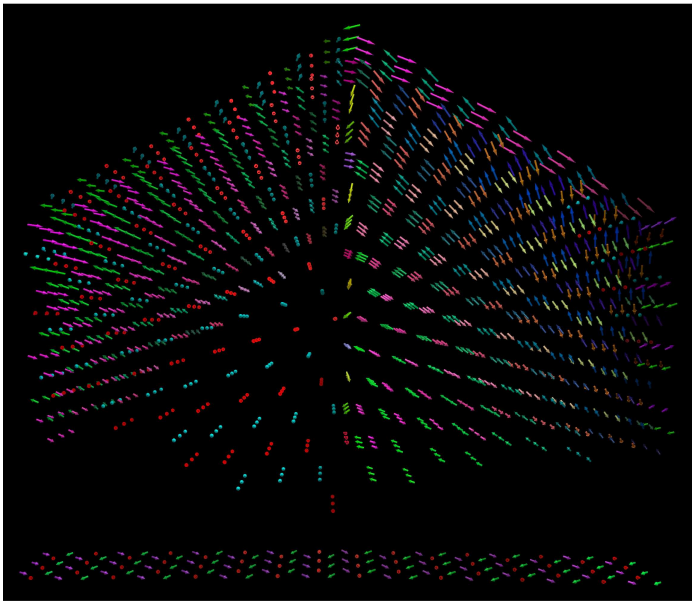

Figure 8.9.: Glyph representation of the α-alumina double-trapezoid sample. Moments with magnitude smaller than 30% of the longest ones were filtered out. Several domains of anti-flexoelectric dipole alignment are visible. There are no well defined domain walls visible but sharp domain borders.

product of the representation of a polar vector as $\mathbf{E}$ with itself and then taking the symmetric part:

$$D^{\epsilon}(D_{3\mathrm{d}}) = [(A_{2u} \oplus E_u) \otimes (A_{2u} \oplus E_u)]_+ = 2A_{1g} \oplus 2E_g. \qquad (8.17)$$

To find the tensor components of d, one has to look for identical irreducible representations inside of $D^{E}(D_{3\mathrm{d}})$ and $D^{\epsilon}(D_{3\mathrm{d}})$. Each irreducible representation which occurs in both representations gives reason to an independent entry in the coupling tensor d. As again expected, $D^{\epsilon}(D_{3\mathrm{d}})$ contains only even and $D^{\epsilon}(D_{3\mathrm{d}})$ only odd representations. Hence, d does not have any non-vanishing entry and no piezoelectricity occurs in α-alumina.

Similarly to the periclase case, MD simulations with the new α-alumina

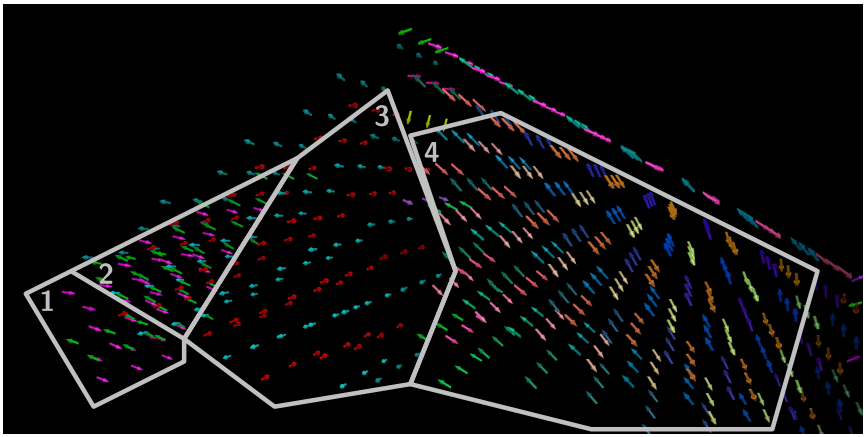

Figure 8.10.: Zoomed view on the double-trapezoid sample as depicted in figure 8.9. Moments with magnitude smaller than 50% of the longest ones were filtered out for a clear view. Three anti-flexoelectric dipole domains can be identified (1, 3 and 4). There exists also an area (2), where the domains 1 and 3 merge fluently.

force field (section 5.3) are able to reproduce the theoretical analysis: On the lines of the periclase simulations, an α-alumina bulk sample was strained homogeneously in different directions and under different loads and no correlated orientations of dipole moments occur.

8.4.2. Flexoelectric behavior and domains

By symmetry aspects, flexoelectric coupling in α-alumina is admitted: The representation of $\mathbf{E}$ in the space of $\mathrm{D}_{3\mathrm{d}}$ was already given in equation (8.16). The representation of $\nabla_{\underline{\underline{\epsilon}}}$ can be constructed by building the representation product of the representation of a matrix as $\underline{\underline{\epsilon}}$ (see equation (8.17)) and a polar vector as $\mathbf{E}$:

$$\begin{aligned} D^{\nabla\epsilon}(D_{3\mathrm{d}}) &= [(A_{2u} \oplus E_u) \otimes (A_{2u} \oplus E_u)]_+ \otimes (A_{2u} \oplus E_u) \\ &= 2A_{1u} \oplus 4A_{2u} \oplus 6E_u. \end{aligned} \tag{8.18}$$

To find the tensor components of h, one again has to search for irreducible representations which occur in both representations $D^E(D_{3\mathrm{d}})$ and

D_{3d}	e	$2C_3$	$3C_2'$	i	$2S_6$	ϵ_d
A_{1g}	1	1	1	1	1	1
A_{2g}	1	1	-1	1	1	-1
A_{1u}	1	1	1	-1	-1	-1
A_{2u}	1	1	-1	-1	-1	1
E_g	2	-1	0	2	-1	0
E_u	2	-1	0	-2	1	0

Table 8.2.: Character table of D_{3d}. e is the identity, C_3 rotation by 120 degrees (axis per definition in z-direction), C_2' rotation by 180 degrees with axis not in z-direction, i inversion, S_6 rotary reflection and ϵ_d reflection about a plane which bisects the angle between two rotation axes C_2'. The index g again stands for even representations, u for odd ones.

$D^{\nabla\epsilon}(D_{3d})$. In the present case, A_{1u} is found four times and E_u is found six times. Hence, ten independent tensor entries are expected and flexoelectricity is possible.

Also for α-alumina, a double-trapezoid sample was generated to investigate domain building. In α-alumina, the domain situation becomes more complex than in the cubic periclase case as depicted in figure 8.9. The two perpendicular strain gradients result in several domains of anti-flexoelectric dipole alignment. There are no well defined domain walls visible but sharp domain borders. This complex flexoelectric behavior may be assigned to the hexagonal scalenohedral crystal structure. Figure 8.10 shows a zoomed view on the upper part of the sample. Three anti-flexoelectric dipole domains can be identified (1, 3 and 4). There exists also an area (2), where the domains 1 and 3 merge fluently.

Finally, the dipole alignment in front of a propagating crack in α-alumina, which was shown in chapter 7, can now be understood. With the piezoelectric analysis, it remained unexplained, why there occurs collective antiferroelectric dipole alignment in front of a crack. These effects can be assigned to flexoelectricity: The crack causes a heterogeneous strain situation which results in the same antiferroelectric dipole alignment as in the case of a domain in the trapezoid sample.

Chapter 9.

Conclusion

The present thesis presents a broad numerical investigation of three relevant metal oxides. Detailled analyses by atomistic MD simulations with novel force fields for silica, magnesia and α-alumina are shown. Specially tailored visualization techniques further advance the finding of new phenomena in ionic condensed matter systems. The investigation mainly specifies a three-stage contribution with diverse facets to research:

1. Firstly, a new powerful force field generation mechanism was described. It combines the polarizable potential model by Tangney and Scandolo with the direct Wolf summation method. It was verified, that the TS benefit of taking electrostatic dipole moments into account and the linear scaling properties of the Wolf sum are unified in the novel generation approach. The implementation in the force field generation package potfit by the author enables the simulation community to apply the accurate, efficient and flexible method to its individual studies of ionic condensed matter.

2. Secondly, three high-quality force fields for silica, magnesia and α-alumina were presented. In addition to its generation, a careful validation was given in each case. The new force fields are not only applied during the work of this thesis, but are accessible for the metal oxide community to perform simulations, which could not yet be adequately investigated with MD simulations due to large system sizes or boundary condition restrictions.

3. By use of the new force fields, several first-time simulation studies were performed (the fractional anisotropy visualization technique, which emphasizes regions of correlated dipole behavior, additionally revealed new findings):

- The α-alumina force field was applied to crack propagation simulation studies, that were able to reproduce the recently experimentally found propagation directions of cracks inserted in different planes of alumina-samples. Furthermore, the influence of heterogeneous strain caused by the crack on the alignment of oxygen dipole moments was depicted for the first time: Vesicular disorder regions and wave-like disorder, both coming from the crack, propagate in regions of correlated dipole alignment and decrease the order.
- Flexoelectric phenomena were finally investigated in detail both by representation theory analyses and MD simulation studies. The result was a consistent prediction of flexoelectric behavior in periclase as well as in α-alumina, although those materials are not able to exhibit piezoelectricity due to their inversion symmetrically crystalline structure. The analytical adopted and experimentally predicted linear relationship between flexoelectric polarization and strain gradient was confirmed in MD simulations. For the first time, flexoelectric domain formation was found in atomistic simulations. In periclase, visualization analyses revealed, that flexoelectric domains are well separated by Néel-walls.

9.1. Outlook

On each of the three stages of development previously described, the present thesis offers paths of further enhancement. Already now, the presented force field approach is used at the ITAP to develop suchlike force fields for modelling other metal oxide systems, e.g. yttrium doped zirconia. In addition, the whole extension to electrostatics in potfit is released [70] and requested. Also the presented and online provided [70] force fields were already downloaded by other groups. In the end, the novel flexoelectric simulation results are expected to be a starting point for atomistic studies of such phenomena in an emerging research area.

Appendix A.

Wolf electrostatic energy expressions

A.1. System with charges

The Wolf shifted and smoothly truncated Coulomb energy expression for a condensed system of charges (C) as described in section 3.1 is obtained by combining equations (3.8) and (3.9) and can be written as

$$\begin{aligned}\tilde{E}_{\mathrm{C}}^{qq}(r_{ij}) \;&= \frac{1}{2}\sum_{\substack{i,j\\ j\neq i}}^{N} q_i q_j \left[\; \frac{\operatorname{erfc}(\kappa r_{ij})}{r_{ij}} - \frac{\operatorname{erfc}(\kappa r_c)}{r_c} \right.\\ &\quad \left. +\;\; (r_{ij}-r_c)\Big[\frac{\operatorname{erfc}(\kappa r_c)}{r_c^2} + \frac{2\kappa}{\sqrt{\pi} r_c} e^{-\kappa^2 r_c^2}\Big] \;\right].\end{aligned} \tag{A.1}$$

A.2. System with charges and dipoles

Shifting the Coulomb energy in a way that the first two derivatives vanish at the cut-off radius was given in (3.28) by

$$\tilde{E}^{qq}(r_{ij}) = E^{qq}(r_{ij}) - E^{qq}(r_c) - (r_{ij}-r_c)\frac{dE^{qq}}{dr_{ij}}\bigg|_{r_c} - \frac{1}{2}(r_{ij}-r_c)^2\frac{d^2E^{qq}}{dr_{ij}^2}\bigg|_{r_c}. \tag{A.2}$$

With it, the first derivative is

$$\frac{d\tilde{E}^{qq}}{dr_{ij}} = \frac{dE^{qq}}{dr_{ij}} - \frac{dE^{qq}}{dr_{ij}}\bigg|_{r_c} - (r_{ij}-r_c)\frac{d^2E^{qq}}{dr_{ij}^2}\bigg|_{r_c} \tag{A.3}$$

and the second one becomes

$$\frac{d^2\tilde{E}^{qq}}{dr_{ij}^2} = \frac{d^2E^{qq}}{dr_{ij}^2} - \frac{d^2E^{qq}}{dr_{ij}^2}\bigg|_{r_c}. \tag{A.4}$$

The Wolf shifted and smoothly truncated Coulomb energy expression for a system with charges and dipoles (C+P) as described in section 3.3 is obtained by combining equations (3.8) and (A.2), which leads to

$$\begin{aligned}\tilde{E}^{qq}_{\mathrm{C+P}}(r_{ij}) &= \tilde{E}^{qq}_{\mathrm{C}}(r_{ij}) - \frac{1}{4}\sum_{\substack{i,j\\ j\neq i}}^{N} q_i q_j (r_{ij}-r_c)^2 \\ &\times \left[-\frac{2\mathrm{erfc}(\kappa r_c)}{r_c^3} + \left(\frac{4\kappa^3}{\sqrt{\pi}} - \frac{4\kappa}{\sqrt{\pi} r_c^2}\right) e^{-\kappa^2 r_c^2} \right].\end{aligned} \tag{A.5}$$

The accordant expression for the interaction energy between a charge and a dipole is obtained by damping and shifting Eq. (3.19) in consideration of the conservation of differential relationship as discussed in section 3.3.1. Using Eq. (A.2), it can be written as

$$\begin{aligned}\tilde{E}^{pq}_{\mathrm{C+P}}(r_{ij}) &= \frac{1}{2}\sum_{\substack{i,j\\ j\neq i}}^{N} q_i \frac{\mathbf{r}_{ij}\mathbf{p}_j}{r_{ij}} \left(\frac{\mathrm{erfc}(\kappa r_{ij})}{r_{ij}^2} - \frac{\mathrm{erfc}(\kappa r_c)}{r_c^2} \right. \\ &+ \frac{2\kappa}{\sqrt{\pi} r_{ij}} e^{-\kappa^2 r_{ij}^2} - \frac{2\kappa}{\sqrt{\pi} r_c} e^{-\kappa^2 r_c^2} - (r_{ij}-r_c) \\ &\times \left. \left[-\frac{2\mathrm{erfc}(\kappa r_c)}{r_c^3} + \left(\frac{4\kappa^3}{\sqrt{\pi}} - \frac{4\kappa}{\sqrt{\pi} r_c^2}\right) e^{-\kappa^2 r_c^2} \right] \right).\end{aligned} \tag{A.6}$$

Finally, the expression for the dipole-dipole interaction is determined by damping and shifting Eq. (3.18) in the same way to conserve the differential relationship and given by

$$\begin{aligned}\tilde{E}^{pp}_{\mathrm{C+P}}(r_{ij}) &= \frac{1}{2}\sum_{\substack{i,j\\ j\neq i}}^{N} \left(\frac{3(\mathbf{r}_{ij}\mathbf{p}_i)(\mathbf{r}_{ij}\mathbf{p}_j)}{r_{ij}^3} - \frac{\mathbf{p}_i\mathbf{p}_j}{r_{ij}} \right) \left(\frac{\mathrm{erfc}(\kappa r_{ij})}{r_{ij}^2} - \frac{\mathrm{erfc}(\kappa r_c)}{r_c^2} \right. \\ &+ \frac{2\kappa}{\sqrt{\pi} r_{ij}} e^{-\kappa^2 r_{ij}^2} - \frac{2\kappa}{\sqrt{\pi} r_c} e^{-\kappa^2 r_c^2} - (r_{ij}-r_c) \\ &\times \left. \left[-\frac{2\mathrm{erfc}(\kappa r_c)}{r_c^3} + \left(\frac{4\kappa^3}{\sqrt{\pi}} - \frac{4\kappa}{\sqrt{\pi} r_c^2}\right) e^{-\kappa^2 r_c^2} \right] \right).\end{aligned} \tag{A.7}$$

Appendix B.

Extension to electrostatics in potfit

Charges and polarizabilites are given as global parameters for each atom type and enter potfit via the potential model. All functions belonging to both Wolf and TS model were implemented in the potfit repetoire. Each single atom can get the new property *dipole moment*, which is calculated during the force routine. The latter determines the forces on each particle by use of the given force field model (These forces are then compared to the ab initio reference data base.). For electrostatics, a new force routine was implemented in potfit; a flowchart is shown in figure B.1. The electrostatic extension can be executed in parallel using the standard MPI. Details for application are given at [70].

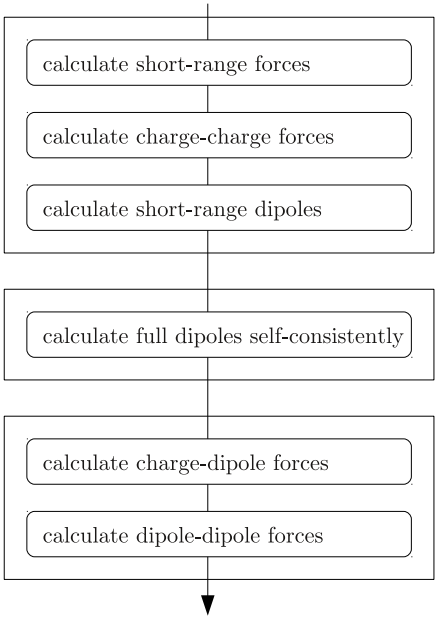

Figure B.1.: Flowchart of electrostatic force routine in potfit, which is called at every optimization step. Each rectangular box denotes a triple loop over all configurations, atoms and neighbors. Inside of the second loop, Eq. (3.16) is solved self-consistently for each configuration, until the convergency criterion Eq. (3.17) is fulfilled. When the dipoles of each atom are known, the dipolar force contributions can be calculated.

Appendix C.

Flexoelectric coupling tensor and free energy density

The explicit structure of the flexoelectric coupling tensor h in a given symmtery can be obtained by use of the A_{1g}-projector $\mathcal{P}^{(A_{1g})}$ to find the appearance of the trivial representation A_{1g} when contracting $\nabla_{\underline{\underline{\epsilon}}}$ with $\mathbf{E}$. Let a group G with group elements g be given. In general, a real projector $\mathcal{P}^{(D^\alpha)}$ onto a representation D^α of G can be defined as

$$\mathcal{P}^{(D^\alpha)} := \frac{1}{|G|} \sum_g \chi^\alpha(g) D(g) \tag{C.1}$$

with $|G|$ the number of elements of G and $\chi^\alpha(g)$ the character of $D^\alpha(g)$. The action of $\mathcal{P}^{(A_{1g})}$ on a scalar function $f(\mathbf{r})$ is then given by

$$\mathcal{P}^{(A_{1g})} f(\mathbf{r}) = \frac{1}{|G|} \sum_g \chi^{A_{1g}}(g) D(g) f(\mathbf{r}). \tag{C.2}$$

Because $\chi^{A_{1g}}(g)$ is equal to 1 for any g and the action of $D(g)$ on $f(\mathbf{r})$ is defined by acting with the inverse representation matrix $D^{-1}(g)$ on the argument,

$$D(g) f(\mathbf{r}) = f(D^{-1}(g)\,\mathbf{r}), \tag{C.3}$$

equation (C.2) can be rewritten as

$$\mathcal{P}^{(A_{1g})} f(\mathbf{r}) = \frac{1}{|G|} \sum_g f(D^{-1}(g)\,\mathbf{r}). \tag{C.4}$$

Using the natural representation as $D(g)$, the action of $\mathcal{P}^{(A_{1g})}$ on the four-stage coordinates directly specifies the independent tensor components and the corresponding basis functions at once.

C.1. Application to O_h

After setting up the natural representations of the 48 elements of O_h, the sum of equation (C.4) can be evaluated for each of the 54 four-stage coordinates ($3 \times 3 \times 6$ for electric field, gradient and strain coordinates). In doing so, one has to keep in mind the index symmetries of h_{klij} which can be seen from equation (8.6) (p. 125): Due to the symmetry of $\underline{\underline{\epsilon}}$, the free energy is invariant when permuting i and j. The final result for the flexoelectric coupling tensor h with components h_{kli} (k index for electric field, l for gradient and i for strain written as vector in Voigt-notation) is:

$$h_{xli} = \begin{pmatrix} h_{11} & 0 & 0 \\ h_{12} & 0 & 0 \\ h_{12} & 0 & 0 \\ 0 & h_{44} & 0 \\ 0 & 0 & h_{44} \\ 0 & 0 & 0 \end{pmatrix}, \; h_{yli} = \begin{pmatrix} 0 & h_{12} & 0 \\ 0 & h_{11} & 0 \\ 0 & h_{12} & 0 \\ h_{44} & 0 & 0 \\ 0 & 0 & 0 \\ 0 & 0 & h_{44} \end{pmatrix}, \tag{C.5}$$

$$h_{zli} = \begin{pmatrix} 0 & 0 & h_{12} \\ 0 & 0 & h_{12} \\ 0 & 0 & h_{11} \\ 0 & 0 & 0 \\ h_{44} & 0 & 0 \\ 0 & h_{44} & 0 \end{pmatrix}. \tag{C.6}$$

This matrix notation corresponds with equation (8.11) (p. 129) and is in accordance with the analyses of Maranganti [56] and Shu [81]. The explicit flexoelectric free energy density f (equation (8.6) on page 125) is given by

$$\begin{aligned} 2f_{\text{flexo}} &= \sum_{k,l} \sum_{i} E_k h_{kli} \nabla_l \epsilon_i \\ &= h_{11} \left[\; E_x \nabla_x \epsilon_{xx} \; + \; E_y \nabla_y \epsilon_{yy} \; + \; E_z \nabla_z \epsilon_{zz} \; \right] \\ &+ h_{12} \left[\; E_x \nabla_x (\epsilon_{yy} + \epsilon_{zz}) \; + \; E_y \nabla_y (\epsilon_{xx} + \epsilon_{zz}) \; + \; E_z \nabla_z (\epsilon_{xx} + \epsilon_{yy}) \; \right] \\ &+ h_{44} \left[\; E_x (\nabla_y \epsilon_{xy} + \nabla_z \epsilon_{xz}) \; + \; E_y (\nabla_x \epsilon_{xy} + \nabla_z \epsilon_{yz}) \right. \\ &\left. + \; E_z (\nabla_x \epsilon_{xz} + \nabla_y \epsilon_{yz}) \; \right] \end{aligned} \tag{C.7}$$

with

$$\epsilon = \begin{pmatrix} \epsilon_{xx} \\ \epsilon_{yy} \\ \epsilon_{zz} \\ \epsilon_{yz} \\ \epsilon_{xz} \\ \epsilon_{xy} \end{pmatrix}. \tag{C.8}$$

Let a strain be given in z-direction ($\epsilon_{zz} \neq 0$) with a gradient in the yz-plane ($\nabla_y \neq 0$ and $\nabla_z \neq 0$) as in the case of the trapezoid sample discussed in section 8.3.2. The corresponding flexoelectric free energy density then becomes

$$2f_{\text{flexo}} \;=\; h_{11}E_z\nabla_z\epsilon_{zz} \;+\; h_{12}E_y\nabla_y\epsilon_{zz}. \tag{C.9}$$

Note that the flexoelectric coupling coefficient h_{44} in periclase cannot be detected with the trapezoid strain situation. As can be seen from equation (C.9), f_{flexo} does not depend on h_{44}. From equations (C.5) and (C.6) it is reasonable that a sheared sample is required for detecting h_{44}.

Bibliography

[1] D. Alfe. Melting curve of MgO from first-principles simulations. *Phys. Rev. Lett.*, 94:235701, 2005.

[2] J. A. Barker and R. O. Watts. Monte Carlo studies of the dielectric properties of water-like models. *Mol. Phys.*, 26(3):789, 1973.

[3] S. Baskaran and X. He. Strain gradient induced electric polarization in α-phase polyvinylidene flouride films under bending conditions. *J. Appl. Phys.*, 111:014109, 2012.

[4] P. J. Basser and C. Perpaoli. Microstructural and physiological features of tissues elucidated by quantitative-diffustion-tensor mri. *J. Magn. Reson. Ser. B*, 111, 1996.

[5] M. Boiocchi, F. Caucia, M. Merli, D. Prella, and L. Ungaretti. Crystal-chemical reasons for the immiscibility of periclase and wüstite under lithospheric P,T conditions. *Eur. J. Mineral.*, 13:871, 2001.

[6] A. Bosak and M. Krisch. Phonon density of states probed by inelastic x-ray scattering. *Phys. Rev. B*, 72:224305, 2005.

[7] P. Brommer. *Development and test of interaction potentials for complex metallic alloys.* Dissertation, Universität Stuttgart, 2008.

[8] P. Brommer and F. Gähler. Effective potentials for quasicrystals from ab-initio data. *Phil. Mag.*, 86:753, 2006.

[9] P. Brommer and F. Gähler. Potfit: effective potentials from ab-initio data. *Model. Simul. Mater. Sci. Eng.*, 15(3):295–304, 2007.

[10] E. V. Bursian and N. N. Trunov. Nonlocal piezoelectric effect. *Sov. Phys. – Solid State*, 16:760, 1974.

[11] A. Carré, L. Berthier, J. Horbach, S. Ispas, and W. Kob. Amorphous silica modeled with truncated and screened coulomb interactions: A

molecular dynamics simulation study. *J. Chem. Phys.*, 127:114512, 2007.

[12] A. Corona, M. Marchesi, C. Martini, and S. Ridella. Minimizing multimodal functions of continuous variables wih the "simulated annealing" algorithm. *ACM Trans. Math. Softw.*, 13:262, 1987.

[13] L. E. Cross. Flexoelectric effects: Charge separation in insulating solids subjected to elastic strain gradients. *J. Mater. Sci.*, 41:53, 2006.

[14] W. de Gruyter. *Anorganische Chemie*. Riedel/Janiak, 2007.

[15] M. Deserno and C. Holm. How to mesh up Ewald sums (I). A theoretical and numerical comparison of various particle mesh routines. *J. Chem. Phys.*, 109(18):7678, 1998.

[16] F. Ercolessi and J. B. Adams. Interatomic potentials from first-principles calculations: the force-matching method. *Europhys. Lett.*, 26(8):583–588, 1994.

[17] S. V. Eremeev, S. Schmauder, S. Hocker, and S. E. Kulkova. Investigation of the electronic structure of Me/Al2O3 (0001) interfaces. *Physica B*, 404:2065, 2009.

[18] A. G. Evans, M. C. Lu, S. Schmauder, and M. Rühle. Some aspects of the mechanical strength of ceramic metal bonded systems. *Acta Metall.*, 34:1643, 1986.

[19] P. P. Ewald. Die Berechnung optischer und elektrostatischer Gitterpotentiale. *Ann. Phys. (Leipzig)*, 64:253–287, 1921.

[20] D. Fincham. Optimization of the Ewald sum for large systems. *Mol. Sim.*, 13(1):1–9, 1994.

[21] G. A. Gaetani, P. D. Asimow, and E. M. Stolper. Determination of the partial molar volume of SiO2 in silicate liquids at elevated pressures and temperatures: A new experimental approach. *Geochim. Cosmochim. Acta*, 62:2499, 1998.

[22] S. Ghose, M. Krisch, A. R. Oganov, A. Beraud, A. Bosak, R. Gulve, R. Seelaboyina, H. Yang, and S. K. Saxena. Lattice dynamics of MgO at high pressure: Theory and experiment. *Phys. Rev. Lett.*, 96:035507, 2006.

[23] P. Gibbon and G. Sutmann. Long-Range Interactions in Many-Particle Simulation. In Johannes Grotendorst, Dominik Marx, and Alejandro Muramatsu, editors, *Quantum Simulations of Complex Many-Body Systems*, volume 10, pages 467–506, 2002.

[24] G. V. Gibbs, D. Jayatilaka, M. A. Spackman, D. F. Cox, and K. M. Rosso. Si-O bonded interaction in silicate crystals and molecules: A comparison. *J. Phys. Chem. A*, 110:12678, 2006.

[25] G. V. Gibbs, A. F. Wallace, D. F. Cox, R. T. Downs, N. L. Ross, and K. M. Rosso. Bonded interactions in silica polymorphs, silicates, and siloxane molecules. *Am. Mineral.*, 94:1085, 2009.

[26] J. M. Gregg. Stressing ferroelectrics. *Science*, 336:41, 2012.

[27] O. Grotheer. *Ab-initio Berechnungen der Spinwellenspektren von Eisen, Kobalt und Nickel*. Dissertation, Universität Stuttgart, 2001.

[28] S. Grottel. *Private communication*.

[29] S. Grottel, G. Reina, and T. Ertl. Megamol: A visualization middleware of point-based molecular data sets. 2012. `http://www.visus.uni-stuttgart.de/megamol/`.

[30] R. M. Hazen. Effects of temperature and pressure on the cell dimension and x-ray temperature factors of periclase. *Am. Mineral.*, 61:266–271, 1976.

[31] D. Herzbach, K. Binder, and M. H. Muser. Comparison of model potentials for molecular-dynamics simulations of silica. *J. Chem. Phys.*, 123(12):124711, 2005.

[32] S. Hocker. *Private communication*.

[33] P. Hohenberg and W. Kohn. Inhomogeneous electron gas. *Phys. Rev.*, 136(3 B):B864, 1964.

[34] J. Hong, G. Catalan, J. F. Scott, and E. Artacho. The flexoelectricity of barium and strontium titanates from first principles. *J. Phys. Cond. Mat.*, 22:112201, 2010.

[35] J Horbach and W Kob. Static and dynamic properties of a viscous silica melt. *Phys. Rev. B*, 60(5):3169, 1999.

[36] `http://www.itap.physik.uni-stuttgart.de/~imd/`.

[37] B. B. Karki, D. Bhattarai, and L. Stixrude. First-principles calculations of the structural, dynamical, and electronic properties of liquid mgo. *Phys. Rev. B*, 73:174208, 2006.

[38] B. B. Karki, D. Bhattarai, and L. Stixrude. First-principles simulations of liquid silica: Structural and dynamical behavior at high pressure. *Phys. Rev. B*, 76(10):104205, 2007.

[39] J. R. Kermode, S. Cereda, P. Tangney, and A. De Vita. A first principles based polarizable O(N) interatomic force field. *J. Chem. Phys.*, 133:094102, 2010.

[40] S. M. Kogan. Piezoelectric effect during inhomogeneous deformation and acoustic scattering of carriers in crystals. *Sov. Phys. Solid State*, 5:2069, 1964.

[41] W. Kohn and L. J. Sham. Self-consistent equations including exchange and correlation effects. *Phys. Rev.*, 140(4A):A1133, 1965.

[42] J. Kolafa and J. W. Perram. Cutoff errors in the Ewald summation formulae for point charge systems. *Mol. Sim.*, 9:351, 1992.

[43] G. Kresse and J. Furthmüller. Efficient iterative schemes for ab initio total-energy calculations using plane-wave basis set. *Phys. Rev. B*, 54(16):11169, 1996.

[44] G. Kresse and J. Hafner. Ab initio molecular dynamics for liquid metals. *Phys. Rev. B*, 47(1):558, 1993.

[45] G. Kresse and D. Joubert. From ultrasoft pseudopotentials to the projector augmented-wave method. *Phys. Rev. B*, 59(3):1758, 1999.

[46] L. Levien and C. T. Prewitt. High-pressure crystal structure and compressibility of coesite. *Am. Mineral.*, 66:324–333, 1981.

[47] L. Levien, C. T. Prewitt, and D. J. Weinder. Structure and elastic properties of quartz at pressure. *Am. Mineral.*, 65:920–930, 1980.

[48] H.-J. Limbach, A. Arnold, B. A. Mann, and C. Holm. Espresso - an extensible simulation package for research on soft matter systems. *Comput. Phys. Commun.*, 174:704, 2006. `http://www.http://espressomd.org`.

[49] Z. Lodziana and K. Parlinski. Dynamical stability of the alpha and theta phases of alumina. *Phys. Rev. B*, 67:174106, 2003.

[50] C.-K. Loong. Phonon densities of states and related thermodynamic properties of high temperature ceramics. *J. Eur. Cer. Soc.*, 19:2241, 1999.

[51] W. Ma and L. E. Cross. Flexoelectricity of barium titanate. *Appl. Phys. Lett.*, 88:232902, 2006.

[52] W. C. Mackrodt, R. J. Davey, S. N. Black, and R. Docherty. The morphology of α-alumina and α-ferric oxide: The importance of surface relaxation. *J. Cryst. Growth*, 80:441, 1987.

[53] E. Madelung. Das elektrische Feld in Systemen von regelmäßig angeordneten Punktladungen. *Phys. Z.*, 19:524–533, 1918.

[54] M. S. Majdoub, P. Sharma, and T. Cagin. Enhanced size-dependent piezoelectricity and elasticity in nanostructures due to the flexoelectric effect. *Phys. Rev. B*, 77:125424, Majdoub2008.

[55] I. Manassidis, A. De Vita, and M. J. Gillan. Structure of the (0001) surface of α-alumina from first principles calculations. *Surf. Sci. Lett.*, 285:L517, 1993.

[56] R. Maranganti, N. D. Sharma, and P. Sharma. Electromechanical coulling in nonpiezoelectric materials due to nanoscale nonlocal size effects: Green's function solutions and embedded inclusions. *Phys. Rev. B*, 74:014110, 2006.

[57] R. Maranganti and P. Sharma. Atomistic determination of flexoeletric properties of crystalline dielectrics. *Phys. Rev. B*, 80:054109, 2009.

[58] A. G. Marinopoulos, S. Nufer, and C. Elsässer. Interfacial structures and energetics of basal twins in α-alumina: First-principles density-functional and empirical calculations. *Phys. Rev. B*, 63:165112, 2001.

[59] H. Matsuo, M. Mitsuhara, K. Ikeda, S. Hata, and H. Nakashima. Electron microscopy analysis for crack propagation behavior in alumina. *Int. J. Fatigue*, 32:592, 2010.

[60] Q. Mei, C. J. Benmore, and J. K. R. Weber. Structure of liquid SiO2: A measurement by high-energy x-ray diffraction. *Phys. Rev. Lett.*, 98:057802, 2007.

[61] H. J. Monkhorst and J. D. Pack. Special points for brillouin-zone integration. *Phys. Rev. B*, 13(12):5188, 1976.

[62] S. Nose. A unified formulation of the constant temperature molecular dynamics method. *J. Chem. Phys.*, 81(1):511, 1984.

[63] A. R. Oganov, M. J. Gillan, and G. D. Price. Ab initio lattice dynamics and structural stability of MgO. *J. Chem. Phys.*, 118(22):10174, 2003.

[64] A. Pasquarello, J. Sarnthein, and R. Car. Dynamic structure factor of vitreous silica from first principles: Comparison to neutron-inelastic-scattering experiments. *Phys. Rev. B*, 57(22):14133, 1998.

[65] G. Peckham. The phonon dispersion relation for magnesium oxide. *Proc. Phys. Soc. London*, 90:657–670, 1967.

[66] J. P. Perdew, J. A. Chevary, S. H. Vosko, K. A. Jackson, M. R. Pederson, D. J. Singh, and C. Fiolhais. Atoms, molecules, solids, and surfaces: Applications of the generalized gradient approximation for exchange and correlation. *Phys. Rev. B*, 46:6671, 1992.

[67] J. P. Perdew and A. Zunger. Self-interaction correction to density-functional approximations for many-electron systems. *Phys. Rev. B*, 23(10):5048, 1981.

[68] J. C. Philipps. Energy-band interpolation scheme based on a pseudopotential. *Phys. Rev.*, 112(3):685, 1958.

[69] H. P. Pinto, R. M. Nieminen, and S. D. Elliot. Ab initio study of γ-alumina surfaces. *Phys. Rev. B*, 70:125402, 2004.

[70] `http://www.itap.physik.uni-stuttgart.de/~imd/potfit/`.

[71] M. J. D. Powell. A method for minimizing a sum of squares of nonlinear functions without calculating derivatives. *Comp. J.*, 7:303, 1965.

[72] H. L. Quang and Q.-C. He. The number and types of all possible rotational symmetries for flexoelectric tensors. *Proc. R. Soc. London, Ser. A*, 467:2369, 2011.

[73] G. Reina and T. Ertl. Hardware-accelerated glyphs for mono- and dipoles in molecular dynamics visualization. *Proc. of Eurovis*, page 177, 2005.

[74] R. Resta. Towards a bulk theory of flexoelectricity. *Phys. Rev. Lett.*, 105:127601, 2010.

[75] T. Rog, K. Murzyn, K. Hinsen, and G. R. Kneller. nmoldyn: A program package for a neutron scattering oriented analysis of molecular dynamics simulations. *J. Comput. Chem.*, 24:657, 2003.

[76] J. Roth, F. Gähler, and H.-R. Trebin. A molecular dynamics run with 5.180.116.000 particles. *Int. J. Mod. Phys. C.*, 11:317, 2000.

[77] A. J. Rowley, P. Jemmer, M. Wilson, and P. A. Madden. Evaluation of the many-body contributions to the interionic interactions in MgO. *J. Chem. Phys.*, 108(24):10209–10219, 1998.

[78] M. Salanne and P. Madden. Polarization effects in ionic solids and melts. *Mol. Phys.*, 109(19):2299, 2011.

[79] K. Scharnowski. *Private communication.*

[80] W. W. Schmahl, I. P. Swainson, M. T. Dove, and A. Graeme-Barber. Landau free energy and order parameter behaviour of the α/β phase transition in cristobalite. *Z. Kristallogr.*, 201(1–2):125–145, 1992.

[81] L. Shu, X. Wei, X. Yao, and C. Wang. Symmetry of flexoeletric coefficients in crystalline medium. *J. Appl. Phys.*, 110:104106, 2011.

[82] D. J. Siegel, L. G. Hector Jr., and J. B. Adams. Ab initio study of Al-ceramic interfacial adhesion. *Phys. Rev. B*, 67:092105, 2003.

[83] S. Speziale, C.-S. Zha, and T. S. Duffy. Quasi-hydrostatic compresn of magnesium oxide to 52 GPa: Implications for the pressure-volume-temperature equation of state. *J. Geophys. Res.*, 106(B1):515, 2001.

[84] J. Stadler, R. Mikulla, and H.-R. Trebin. IMD: a software package for molecular dynamics studies on parallel computers. *Int. J. Mod. Phys. C.*, 8(5):1131–1140, 1997.

[85] J. Sun, T. Stirner, and A. Matthews. Calculation of native defect energies in α-Cr2O3 using a modified Matsui potential. *Surf. Coat. Tech.*, 201:4205, 2006.

[86] A. K. Tagantsev. Piezoelectricity and flexoelectricity in cristalline dielectrics. *Phys. Rev. B*, 34(8):5883, 1986.

[87] P. Tangney and S. Scandalo. A many-body interaction potential for ionic systems: Application to MgO. *J. Chem. Phys.*, 119(18):9673, 2003.

[88] P. Tangney and S. Scandolo. An ab initio parametrized interatomic force field for silica. *J. Chem. Phys.*, 117(19):8898–8904, 2002.

[89] B. W. H. van Beest, G. J. Kramer, and R. A. van Santen. Force fields for silicas and aluminophosphates based on ab initio calculations. *Phys. Rev. Lett.*, 64(16):1955–1958, 1990.

[90] P. Vashishta, R. Kalia, J. Rino, and I. Ebbsjö. Interaction potential for SiO2: A molecular-dynamics study of structural correlations. *Phys. Rev. B*, 41(17):12197, 1990.

[91] A. K. Verma, P. Modak, and B. B. Karki. First-principles simulations of thermodynamical and structural properties of liquid Al2O3 under pressure. *Phys. Rev. B*, 84:174116, 2011.

[92] P. Villars and L. D. Calvert. *Pearson's Handbook of Crystallographic Data for Intermetallic Phases, 2nd Edition, Vol. I.* ASM International, Materials Park, Ohio, 1991.

[93] K. Vollmayr, W. Kob, and K. Binder. Cooling-rate effects in amorphous silica: A computer-simulation study. *Phys. Rev. B*, 54(22), 1996.

[94] R. Vuilleumier, N. Sator, and B. Guillot. Computer modeling of natural silica melts: What can we learn from ab initio simulations. *Geochim. Cosmochim. Acta*, 73:6313–6339, 2009.

[95] R. C. Weast, editor. *CRC Handbook of Chemistry and Physics*. CRC Press, Boca Raton, FL, 1983.

[96] `http://de.wikipedia.org/wiki/Pseudopotential`.

[97] D. Wolf, P. Keblinski, S. R. Phillpot, and J. Eggebrecht. Exact method for the simulation of Coulombic systems by spherically truncated, pairwise 1/r summation. *J. Chem. Phys.*, 110(17):8254–8282, 1999.

[98] W. Wunderlich and H. Awaji. Molecular dynamics-simulations of the fracture toughness of sapphire. *Material & Design*, 22:53, 2001.

[99] W. Zhang and J. R. Smith. Nonstoichiometric interfaces and Al2O3 adhesion with Al and Ag. *Phys. Rev. Lett.*, 85:3225, 2000.

[100] W. Zhang and J. R. Smith. Stoichiometry and adhesion of Nb/Al2O3. *Phys. Rev. B*, 61:16883, 2000.

[101] P. Zubko, G. Catalan, A. Buckley, P. R. L. Welche, and J. F. Scott. Strain-gradient-induced polarization in SrTiO3 single crystals. *Phys. Rev. Lett.*, 99:167601, 2007.

List of Publications

(1) P. Brommer, P. Beck, A. Chatzopoulos, F. Gähler, J. Roth, and H.-R. Trebin. Direct Wolf summation of a polarizable force field for silica. *J. Chem. Phys.* 132 (19), 194109 (2010).

(2) P. Beck, P. Brommer, J. Roth, and H.-R. Trebin. Ab initio based polarizable force field generation and application to liquid silica and magnesia. *J. Chem. Phys.* 135, 234512 (2011).

(3) S. Hocker, P. Beck, S. Schmauder, J. Roth, and H.-R. Trebin. Simulation of crack propagation in alumina with ab initio based polarizable force field. *J. Chem. Phys.* 136, 084707 (2012).

(4) P. Beck, P. Brommer, J. Roth, and H.-R. Trebin. Influence of polarizability on metal oxide properties studied by molecular dynamics simulations. *J. Phys.: Condens. Matter* 24, 485401 (2012).

(5) T. Barthelmes, and P. Beck. Simulationen erklären den Riss. *Stuttgarter Unikurier* 110 (2012).

(6) S. Grottel, P. Beck, C. Müller, G. Reina, J. Roth, H.-R. Trebin, and T. Ertl. Visualization of electrostatic dipoles in molecular dynamics of metal oxides. *IEEE Transactions on Visualization and Computer Graphics* 18(12), 2061 (2012).

(7) K. Scharnowski, M. Krone, P. Beck, and F. Sadlo. Visualization of Polarization Domains in Barium Titanate. *IEEE Transactions on Visualization and Computer Graphics*, SciVis contest winner 2012.

Danksagung

Ich bedanke mich bei meinem Doktorvater Prof. Dr. Hans-Rainer Trebin für die Betreuung meiner Arbeit über die letzten drei Jahre. Seine mit nicht endender Weite reichende Förderung, Unterstützung und Beratung verdienen meinen größten Dank. Für erfolgreiches Forschen unter Wohlfühl-Atmosphäre kann ich mir keine bessere Betreuung vorstellen. Seine freundliche und menschliche Art überträgt sich auf alle Mitarbeiter und hat mich jeden Tag gerne ans Institut kommen lassen.

Danken möchte ich Prof. Dr. Christian Holm für die Übernahme des Zweitberichts und die engagierte und intensive Auseinandersetzung mit meiner Arbeit sowie Prof. Dr. Jörg Wrachtrup für die freundliche Übernahme des Prüfungsvorsitzes.

Ein sehr großes Dankeschön richte ich an Priv.-Doz. Dr. Johannes Roth für die unersetzliche Unterstützung und Zusammenarbeit der vergangenen Jahre. Ob es administrative Probleme an meinem Rechner, physikalische Fragestellungen jeder Art oder die Zusammenarbeit an den meisten meiner Veröffentlichungen bezüglich der vorliegenden Arbeit waren, stellte sich Johannes immer als wertvoller Ansprechpartner und Ideengeber zur Verfügung.

Besonderer Dank gilt Dr. Peter Brommer, dessen Nachfolge ich im November 2009 antrat. In einwöchiger fliegender Arbeitsplatz-Übergabe half er mir beim Einarbeiten in die neue Thematik und ist seitdem auch aus der Ferne Kanadas oder Englands erster externer Berater geblieben. Ich bedanke mich für die erfolgreiche Zusammenarbeit, die zu drei gemeinsamen Veröffentlichungen bezüglich der vorliegenden Arbeit geführt hat.

Ich bedanke mich bei Stephen Hocker, Sebastian Grottel, Michael Krone und Katrin Scharnowski für spannende Kooperationen, innerhalb derer wir verschiedene Kompetenzen erfolgreich gebündelt haben. Mit Stephen habe ich gerissene Ergebnisse erlangt, Sebastian hat mir zu mega Durchblicken verholfen, und Michael sowie Katrin haben mit mir Domänen gesucht und gefunden.

Ein besonderer Dank gilt den helfenden Kollegen, ohne die eine Arbeit diesen Ausmaßes nicht annähernd denkbar ist: Daniel Schopf glühen nach drei Jahren beide Ohren aufgrund all der Fragen, die ich zur Implementierungs-Arbeit in potfit und weiteren diversen administrativen Themen hatte. Dr. Holger Euchner hatte ebenfalls immer eine offene Türe für mich rund ums Thema Phononen. Mit Benjamin Frigan habe ich mich durch die tiefen Tiefen der Gruppentheorie gekämpft, deren Erkenntnisse ich schließlich zur Analyse der flexoelektrischen Phänomene anbringen konnte.

Tina Barthelmes danke ich für die Öffentlichkeitsarbeit im Sonderforschungsbereich 716 und die freundliche Zusammenarbeit, die mir immer Spaß gemacht hat.

Für die Zusammenarbeit in der Metalloxid-Gruppe danke ich Andreas Chatzopoulos, Andreas Irmler und Martina Dombrowski. Außerdem bedanke ich mich bei Dr. Franz Gähler, Dr. Frohmut Rösch und Hans-Jörg Lipp, die sich als helfende Kollegen ebenfalls nicht von meiner Frage-Offensive abschrecken ließen.

Nicht vergessen werden darf mein erster Zimmerkollege Dr. Stephen Sonntag, der als direkter Nebensitzer gerade in meiner Anfangszeit Ansprechpartner für Fragen aller Art war.

Ein Dankeschön geht an unser liebes Sekretariat, wo mich Ulrike Mergenthaler, Marietta Köstler und Simone Blümlein immer mit einem Lächeln begrüßen und mir bei organisatorischen Angelegenheiten aller Art gerne weitergeholfen haben.

Die vorliegende Arbeit wurde im Rahmen der Deutschen Forschungsgemeinschaft, Sonderforschungsbereich 716, erarbeitet. Hierdurch wurde mir ein unermesslicher Reichtum an Möglichkeiten für interdisziplinäre Kooperationen gegeben, die ich gerne wahrgenommen habe. Den Blick über den Tellerrand zu Werkstoffkundlern und Visualisierern möchte ich nicht missen.

Ein unendlich dickes Dankeschön geht an die Person, die sich über die Jahre meiner Promotion kein einziges Mal darüber beschwert hat, wenn ich zu Zeitpunkten Richtung Mitternacht Ideen hatte wie “ich schau nochmal schnell, ob ich neue Jobs submitten kann” oder wenn ich Sonntags “nur mal schnell einen Artikel überfliegen” wollte: Danke Kerstin für die liebe Unterstützung, die mir die Ausgeglichenheit und innere Ruhe gibt, die für die vorliegende Arbeit ein wichtiger Eckpfeiler war.

Besonderer Dank gilt meinen Eltern, die mich über all die Jahre in höchstem Maße und in jedweder Richtung gefördert haben. Die Selbstverständlichkeit, mit welcher sie mich – jeder auf seine individuelle und wunderbare Weise – unterstützt haben, verdient meinen größten Dank und meine Bewunderung. Ihnen widme ich diese Arbeit ebenso wie Laura. Sie ist zufällig meine Schwester, aber aus Verbundenheit meine beste Freundin. Sie hat über all die Jahre am stärksten an mich geblaubt hat und unterstützt mich bedingungs- und bedenkenlos in allen Lebenslagen.

Ich erkläre hiermit, dass ich die vorliegende Arbeit selbständig und nur mit den angegebenen Hilfsmitteln angefertigt habe und dass alle Stellen, die im Wortlauf oder dem Sinne nach anderen Werken entnommen sind, durch Angabe der Quellen als Entlehnung kenntlich gemacht worden sind.

Stuttgart, im November 2012 *Philipp Beck*